DISORDERED INSULATOR IN AN OPTICAL LATTICE

BY

MATTHEW JAMES PASIENSKI

DISSERTATION

Submitted in partial fulfillment of the requirements
for the degree of Doctor of Philosophy in Physics
in the Graduate College of the
University of Illinois at Urbana-Champaign, 2011

Urbana, Illinois

Doctoral Committee:

Assistant Professor Ben Lev, Chair
Associate Professor Brian DeMarco, Director of Research
Professor Robert Clegg
Professor David Ceperley

Abstract

We experimentally studied the transport properties of ultracold bosonic atoms trapped in a disordered optical lattice—a system described by the disordered Bose-Hubbard model, which is a paradigm important to condensed matter physics. The disorder is created using a controllable and completely characterized fine-grained optical speckle field that is superimposed on ^{87}Rb atoms confined in a three-dimensional lattice in the strongly correlated regime. We discovered that above a critical disorder strength, the gas of atoms transforms from a superfluid to a disordered insulator. We compare our results to recent quantum Monte-Carlo numerical simulations of this model. Finally, I present an algorithm we invented that allows the profile of laser beams to be shaped holographically into arbitrary intensity patterns suitable for trapping ultracold atoms.

Acknowledgements

This is an incomplete list of the people who most directly contributed to this work. My parents and family have consistently supported me with enthusiasm and finances. Their example of cheerfulness, honesty, and hard work is the source of my motivation. In our laboratory, I fortunately have been surrounded by a competent, devoted, and pleasant group of researchers. I am especially grateful for the example of Professor Brian DeMarco as well as Matt White, and Dave McKay. I am also glad that I can confidently leave our lab to a fantastic group of young researchers: David Chen, Carrie Meldgin, Stan Kondov, Will McGehee. Our postdocs, Hong Gao and Josh Zirbel, each solved problems with energy, creativity, and rigor. The University of Illinois has provided us with many fine undergraduate researchers, especially Lauren Aycock, Cece Borries, and Paul Koehring. In the physics department I would like to acknowledge Professors Kwiat, Lev, Ceperley, Vishveshwara, Goldbart, and Clegg and their graduate students Kuei Sun, Sheng Quan Zhou, Sarang Gopalakrishnan, Onur Hosten, Julio Barreiro, Seo Ho Youn, Ushnish Ray, Matt Naides, Will Turner, and Mingwu Lu for their contributions to my research and enlightening discussions. Finally, I would like to thank Claire Wright.

Table of Contents

Chapter 1

Introduction

1.1 Introduction

This dissertation primarily describes research into the transport properties of an ultra-cold gas of ^{87}Rb atoms trapped in a disordered optical lattice. These transport experiments were conducted to gain insight into the phase diagram of the disordered Bose-Hubbard model — a paradigm important to the study of certain condensed matter systems. The experiments described in this dissertation accessed a new regime for cold atoms that complements state-of-the-art quantum Monte Carlo simulations. The regime of strongly interacting bosons in a three-dimensional disordered lattice had not been studied previously using the unique abilities of ultra-cold atomic physics. These measurements map the superfluid-to-insulator transition in the disordered Bose-Hubbard phase diagram at finite temperature and a density less than or equal to one particle per site.

This work builds on previous experimental measurements with optical speckle and disordered lattices. Disordered bosons have been studied in trapped gases [1–3] in one-dimensional lattices with optical speckle [4–8]; related work has been done with one-dimensional incommensurate bichromatic lattices [9–12]. Anderson localization, a non-interacting effect, has also been studied in one-dimension [13, 14] using an ultra-cold gas of atoms. What distinguishes the work in this dissertation from previous work with cold atoms is that the gas in our work consists of strongly correlated particles and we trap them in a three-dimensional disordered lattice.

Atom lattice experiments are powerful tools for simulating models of strongly correlated materials. Quantities like the Hubbard tunneling and interaction energies can be calculated ab initio. Completely characterized disorder can be controllably added to a lattice, and be made absent or larger than any other energy scale. This Hamiltonian can then be tuned over a wide range of realizations for each measurement and changed every typically 100-second-long experimental cycle.

In this chapter I will first describe the motivation that led us to study the disordered Bose-Hubbard model experimentally. Next, I will describe the apparatus used to create both a Bose-Einstein condensate (BEC) as well as the novel three-dimensional disordered optical lattice into which the BEC is loaded. After stating both the motivation for our work and the apparatus we use to perform it, I will then present a summary of the main results

of these experiments and their implications. Last, I will preview the new experimental technique detailed in the final chapter of this dissertation, as well as proposals for future research.

The remaining chapters are organized into three topics:

- Chapter 2: features of the disordered Bose-Hubbard model important to our study of ultra-cold ^{87}Rb atoms in a disordered optical lattice;
- Chapter 3: the techniques we used to probe transport of a strongly interacting gas in a disordered lattice and the results of those experiments;
- Chapter 4: an algorithm we developed to create arbitrary holographic optical dipole atom traps.

1.2 Motivation

We created a gas of ultra-cold atoms in a disordered optical lattice to serve as a quantum emulator of the disordered Bose-Hubbard model [15]. The goal of emulation is to find the solution of this model by observing atoms which are described by the same Hamiltonian. We can then use that knowledge to better understand other systems which the disordered Bose-Hubbard model has been used to study. These systems include: films of liquid helium on disordered substrates [16], solid helium [17, 18], and Josephson junction arrays [19] (see Chapter 2). The disordered Bose-Hubbard model still has many open questions, despite the amount of attention it has attracted over the past twenty years (see, for example, [20–23]). By simulating the disordered Bose-Hubbard model using atoms, we hope to answer some of these open questions.

The ability to emulate quantum mechanical models can be an important link in the theoretical study of models of strongly correlated condensed matter. For certain models it is not possible to find a solution even with the fastest computers. We are condemned to reach this point when simulating the interaction of quantum particles, a fact often attributed to Feynman [24]. He showed that for any classical computer, the difficulty of exactly calculating the dynamics of N quantum particles grows exponentially with N [†]. Therefore, if it takes 10 seconds on a computer to calculate the exact dynamics of 100 quantum particles, it would take 10^{10} seconds (317 years) to calculate the exact solution for 1000 particles. Thus for any quantum mechanical system system of even moderate size, there will exist some property that is not capable of being calculated, no matter the speed of the computer. When both analytical and numerical methods fail to solve a model, a quantum emulator may be able to fill in this gap.

[†]Although this statement is generically true, there exist many instances where a basis can be found such that the representation does not require an exponential number of terms.

When an analytical solution is not available, numerical methods still have an important role in solving models despite their fundamental restrictions. The techniques of quantum Monte-Carlo (QMC) computer simulation are capable of calculating exactly (i.e., with bounds on the maximum error) the behavior of many physical systems (see, for example, [25]). However, certain systems require a great deal more computational resources to solve using QMC methods than others. For example, the disordered Bose-Hubbard model has not been solved either at finite temperature nor at non-unit filling (see, for example, [23]). Although it is possible to do both, it would require tremendous amounts of computer power that no one has yet been willing to invest. Cold atoms, on the other hand, are always at a small finite temperature which can be changed easily. Because each of these two complementary techniques may be more capable of simulating or emulating a model under different conditions, it is advantageous to develop QMC and ultra-cold atom emulation together. In this dissertation we demonstrate how the two techniques can work together to tackle an unsolved problem.

1.3 Apparatus

To perform the experiments described in this dissertation, we built an apparatus that creates a Bose-Einstein condensate, loads it into a disordered lattice, and measures its properties using absorption imaging. This section will introduce this experimental apparatus. We have attempted where possible in this introductory chapter not to replicate the details provided in the dissertation by my colleague Dr. Matt White [26] (or, for instance, Ref. [27]) more than is necessary to understand the experiments covered in the following chapters.

This section is organized into three parts:

- standard atomic physics techniques used to produce a condensate of ^{87}Rb atoms in a hybrid magnetic/optical trap,
- a description of a three-dimensional disordered optical lattice, created using optical speckle,
- the techniques used to measure the gas; first manipulating the atoms in the lattice, then taking time-of-flight images.

1.3.1 Making a BEC

The study of the superfluid-to-insulator transition of atoms in an optical lattice requires ultra-cold temperatures. To achieve these temperatures, the atoms must be cooled below the Bose-Einstein condensation transition (~ 60 nK for our experiment) in a harmonic trap before being loaded into the lattice. This section will describe the methods and equipment we use to cool a room-temperature gas of ^{87}Rb atoms in a vapor cell to a nearly pure BEC with between 6 to 150 thousand atoms in an hybrid optical/magnetic trap.

The properties of ^{87}Rb make it a good choice for creating BECs. An alkali with a single valence electron, Rb has a small set of optically addressable transitions [28]. This simple structure allows us to cool atoms in a magneto-optical trap (MOT) using a single trapping laser wavelength and another "repump" laser detuned from trapping laser by the 6.8 GHz ground-state hyperfine splitting (see Figure 1.1). Additionally, inter-particle scattering in ^{87}Rb at low temperatures allows the ensemble of atoms to collide and thermalize quickly, enabling efficient evaporative cooling [29].

The process of creating a BEC starts by collecting several billion atoms in a magneto-optical trap (MOT) at the center of an evacuated cell containing a dilute gas of Rb. The room temperature Rb vapor limits the lifetime of a trapped atom to only a few seconds, making this cell an unsuitable environment for evaporation. To solve this problem, our vacuum system is divided into two sections (see Figure 1.2). The first relatively higher pressure MOT cell is connected by a thin ($\sim$ 1 cm diameter by $\sim$ 1 meter length) tube to another chamber where we evaporatively cool atoms and load them into an optical lattice. With the help of two ion pumps and a titanium-sublimation pump, the small tube allows a large difference in pressure between the glass cells containing the MOT on one end and the optical lattice on the other. BECs can be held for minutes in this low-pressure,"science" cell, vastly longer than the duration of any lattice experiment we perform.

The MOT both collects and cools the atoms, bringing several billion from room-temperature to tens of micro-kelvin. The MOT itself is formed by a combination of a weak magnetic quadrupole field, 3 retro-reflected trap lasers, and a repump laser. The trap lasers are red detuned by 17 MHz from the $|F = 2\rangle$ to $|F = 3\rangle$ "cycling" transition of the D2 line (see Figure 1.1). For the MOT, the magnetic field gradient is set to 10 G/cm.

The light used to create the MOT comes from two external cavity diode lasers (ECDLs) and three injection-locked "slave" lasers. The ECDL that creates the trapping light is locked to the $|F = 2\rangle$ to $|F = 3\rangle$ cross-over peak using a polarization spectroscopy lock [30, 31]. To provide more power, this light is injected into three slave lasers which then form the three retro-reflected MOT beams. The repump is locked 6.8 GHz away using an optical phase lock loop. A portion of both the trap and repump light is split off to image the atoms.

Once the MOT has collected and cooled the atoms, they are transferred to a magnetic trap. This transfer has several steps which cool the atoms and prepare them in a magnetically trappable state. First, the size of the atom gas is reduced by changing the detuning of the trapping lasers from 17 MHz to 50 MHz [32]. Next the quadrupole is turned off and the atoms are cooled using polarization gradient cooling. This smaller, colder gas is then optically pumped into the $|F = 1, m_F = -1\rangle$ state. The magnetic coil current is turned up to 192 A in 10 ms to trap the atoms in a spherical quadrupole trap.

The linear translation stage next carries the magnetic trap coils — along with the atom gas — to the "science" chamber. The translation stage moves approximately 1 meter from the MOT cell to the science cell in about 1 second. While still in the magnetic trap an

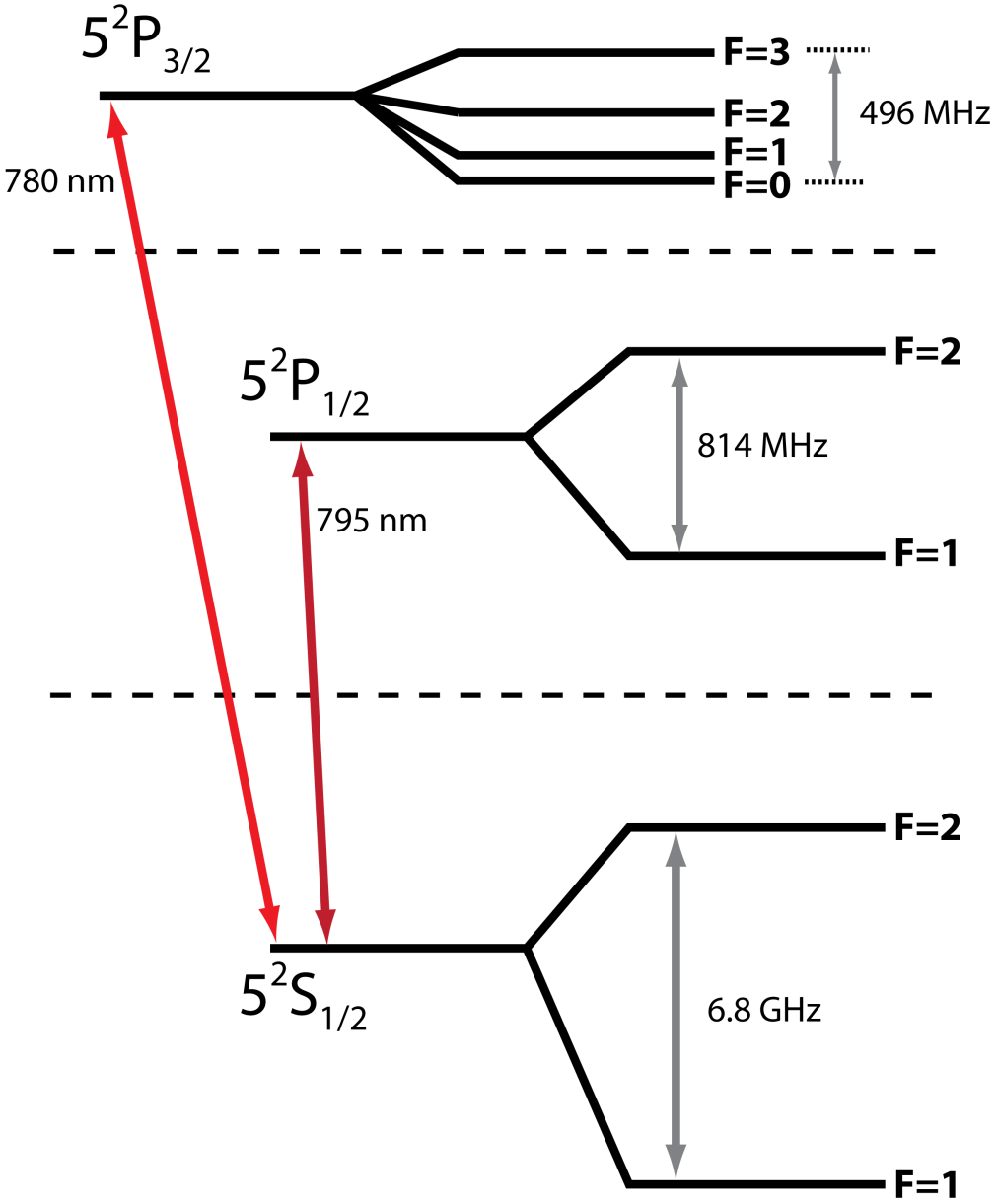

Figure 1.1 The two excited states of rubidium connected to the ground state by the D1 (795 nm) and D2 (780 nm) electric dipole transitions [28] (not to scale). We address the ground state hyperfine splitting with a 6.8 GHz microwave source.

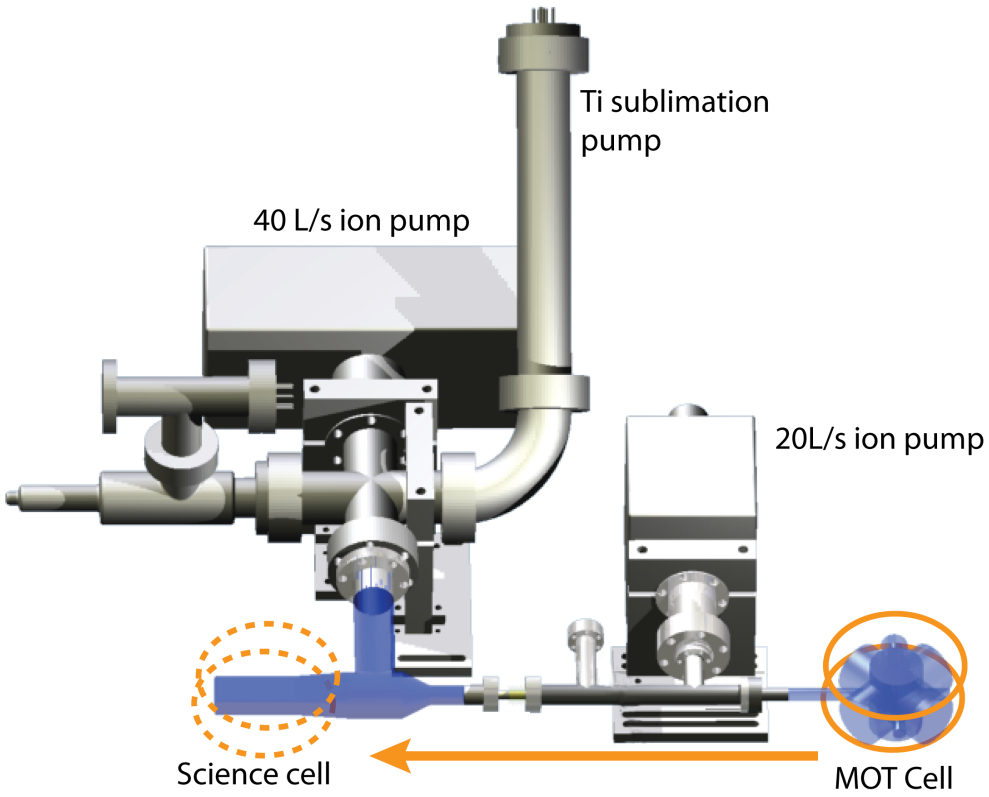

Figure 1.2 The vacuum system. A MOT collection cell is connected to the "science" cell by a $\sim$ 1 cm diameter tube. The solid orange circles indicate the initial position of the magnetic quadrupole coils at the MOT cell. A linear translation stage moves the coils (direction indicated by orange arrow) and atoms to the science cell in $\sim$ 1 second; the final position is indicated by the broken orange circles. The low vacuum pressure in the science cell ($< 10^{-11}$ Torr) is maintained by two ion pumps as well as a titanium-sublimation pump. In this configuration the small connecting tube creates a differential pressure between the MOT vapor cell and the science cell.

RF-frequency magnetic field is used to transfer atoms into an untrapped Zeeman state, removing atoms above a successively lower energy threshold as evaporation progresses [33]. This colder gas is loaded into a hybrid optical/magnetic trap, and evaporation is continued by changing the hybrid trap's support against gravity and depth. After transferring the atoms into the hybrid optical/magnetic trap, the cart returns to its original position allowing increased optical access.

The hybrid optical/magnetic trap consists of an optical dipole beam focused 100 μm below the center of a magnetic spherical quadrupole field [34, 35]. The atoms are confined in two directions by a focused far-red-detuned 1064 nm optical dipole beam with a 120 μm waist. Along the propagation axis of the focused beam, the magnetic field curvature confines the polarized atoms, creating a trap with a mean frequency of $\bar{\omega} = (\omega_x \omega_y \omega_z)^{1/3} = 2\pi 40$ Hz. The most energetic atoms are evaporated by either tilting, or later lowering, the confining potential created by the hybrid optical/magnetic potential. Reducing the magnetic field gradient or laser intensity evaporates atoms by reducing the support against gravity, or potential energy barrier confining the atoms, respectively. To decrease the atom number we continue to decrease the trap depth below the chemical potential of the condensate.

This system is capable of producing nearly pure BECs of up to $2 \cdot 10^5$ atoms every 100 seconds. For the measurements described in Chapter 3, nearly pure BECs of as few as 6000 atoms are produced to load an optical lattice with one or fewer atoms per site.

1.3.2 The Disordered Optical Lattice

A disordered optical lattice allows us to study the disordered Bose-Hubbard model. A clean lattice potential free of any disorder, formed by the standing waves of multiple orthogonal retro-reflected lasers, has already been used to demonstrate the transition from a superfluid to a 3D Mott insulator [36–38]. We extend this technique by adding controllable disorder to the lattice in the form of an optical speckle potential formed by a single far-blue-detuned laser beam focused through a diffuser and high-numerical-aperture lens [39]. By applying impulses to the gas to study transport, we were able to study the superfluid-to-disordered-insulator transition (see Chapter 3) predicted for the disordered Bose-Hubbard Hamiltonian (see Chapter 2).

These potentials are made possible by the AC Stark effect — an interaction between the atomic electric dipole moment and light's electric field [40]. When a laser is far-detuned from atomic resonance, the conservative potential V_{ACS} created by the AC Stark shift (for a 2-level atom) is:

$$V_{ACS}(r) = \frac{3\pi c^2}{2\omega_0^3} \frac{\Gamma}{\delta} I(r) \tag{1.1}$$

where c is the speed of light, $\omega_0 = 2\pi c/\lambda$ (λ is the wavelength of an atomic resonance), Γ is the linewidth of the resonance, $\delta = \omega - \omega_0$ is the detuning of the laser frequency ω from the atomic resonance, and $I(r)$ is the intensity of the laser. When δ is much larger

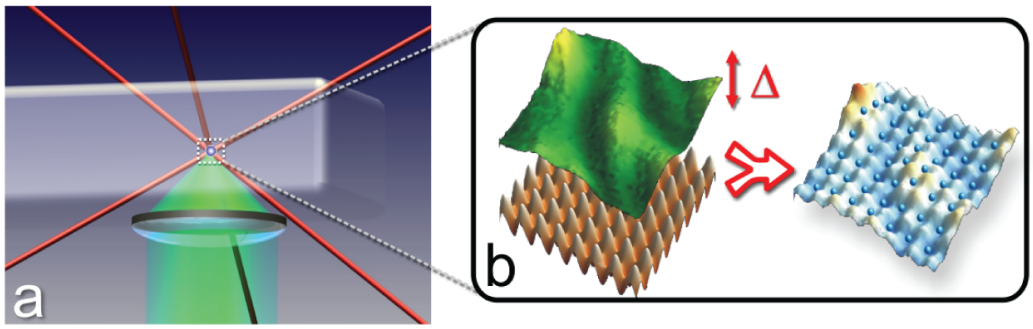

Figure 1.3 A schematic of optics combining the (green) disordered optical speckle beam with the (red) optical lattice (**a**). A 15 mm diameter lens focuses 532 nm light through a diffuser onto atoms in the science cell, 13 mm away. Three retro-reflected, 812 nm beams intersect to form a three-dimensional optical lattice. A slice through the lattice along a plane orthogonal to one of the lattice beams (**b**) is shown combined with the disorder potential with average value Δ in green. The combined potential (far right) demonstrates the fine-grain disorder size to scale, and is produced from a speckle intensity distribution measured ex-situ.

than the fine-structure splitting Δ_{FS}, the potential does not depend on the internal state of the atoms. Furthermore a large detuning δ allows for conservative potentials that do not heat the atoms significantly [40], since the light scattering rate is proportional to $1/\delta^2$. If laser light is detuned far to the red of the D1 and D2 transition, as it is for our clean lattice potential, the atoms are attracted to regions of higher intensity. Alternatively, the far-blue-detuned speckle potential repels atoms from areas of high light intensity.

The disordered lattice is formed by a $\lambda_S = 532$ nm (green) speckle beam propagating upward and three retro-reflected mutually orthogonal $\lambda_L = 812$ nm (red) optical lattice beams tilted at angles of 30°, 30°, 45° respectively from vertical (see Figure 1.3(a)). In addition to having nearly orthogonal polarization, the lattice beams are shifted in frequency by several MHz relative to each other. The relative frequency difference causes interference between the orthogonal beams to vary much faster than the atoms can respond, leaving an average static lattice potential. The 3D cubic lattice potential has a spacing between adjacent sites of $d = 406$ nm. The lattice potential for each beam is

$$V_L(x', y', z') = s(\cos^2 kx' + \cos^2 ky' + \cos^2 kz') \tag{1.2}$$

where $k = 2\pi/\lambda$, and x',y', and z' are the coordinates along the lattice directions. Each lattice beam has a Gaussian profile with a waist $w_L = 120$ μm. We measure the maximum barrier between lattice sites as $V_{max} = s$; s is the potential depth of each lattice beam standing wave measured in units of lattice photon recoil energy $E_R = \frac{\hbar^2 2\pi^2}{\lambda^2 m}$, where m is the mass of ^{87}Rb, and the lattice wavelength $\lambda = 812$ nm. Although the lattice depth does not change significantly across the gas, the curvature of the lattice beams causes the harmonic trap frequency trapping the atoms to increase as the lattice depth is increased (see Chapter 2). The speckle intensity is characterized by $\langle V_S \rangle = \Delta$, where $\langle V_S \rangle$ is the average speckle

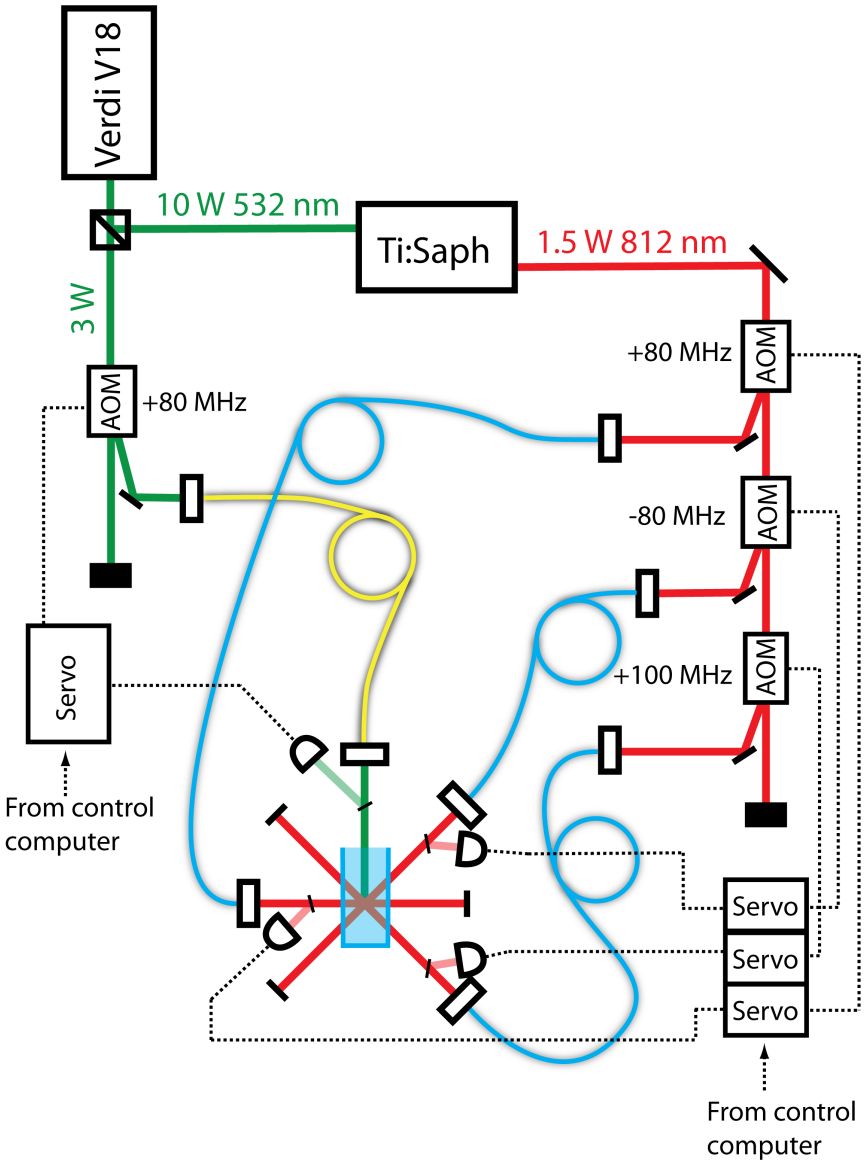

Figure 1.4 This diagram shows only the lasers involved in creating the disordered lattice. 13 W of green light is split into 10 W to pump a Ti:Saph ring-cavity laser, and 3 W for the speckle beam. The Ti:Saph laser produces up to 1.5 W of laser light that can be tuned from roughly 750-850 nm; in work considered in this dissertation, 812 nm light forms a red-detuned lattice. The power in each of the three lattice beams is controlled by an AOM connected to a servo which measures power at the other end of a single-mode polarization-preserving fiber (blue fibers). Each AOM is detuned by a different amount ($\pm$80, 100 MHz) to avoid interference between orthogonal lattice beams which would change the potential the atoms experience. The speckle light is controlled by a similar servo. However, the speckle beam is coupled to a non-polarization-preserving fiber (yellow fiber).

potential at the atoms.

The laser light which forms the disordered lattice is produced by an 18 W 532 nm Nd:YVO_4 laser (Coherent Verdi V-18) which does two things. First, it pumps the 1.5 W Ti:Sa laser (Tekhnoscan TIS-SF-077) which creates the 812 nm lattice beams (see Figure 1.4). Second, 532 nm light from the Verdi creates the optical speckle potential. The V-18 is run below its maximum power at 13 W, 10 W pumping the Ti:Sa and 3 W diverted to form the optical speckle beam. The 812 nm light is split into three beams using acousto-optical modulators (AOMs) that are also part of a servo feedback loop that controls the intensity of each beam independently. Each lattice beam is coupled into a polarization preserving single mode fiber which transports it to a platform above the science cell. The 532 nm speckle beam is similarly servoed by an AOM, but is coupled into a single mode fiber which does not preserve polarization. The speckle beam optics and servo pick-off are not polarization sensitive, nor is the interaction between the far-detuned light and atoms.

1.3.3 Optical Speckle

The disordered optical lattice we create is the first realization of a 3D disordered lattice with fine-grain disorder in all directions. This is in contrast to earlier experimental work with speckle in one dimension [1, 3, 4, 7], or with related experiments using bichromatic (i.e quasiperiodic) lattices [9, 10, 14] (see Chapter 2). This section will show how we model and precisely measure this 3D speckle potential.

Optical speckle is produced by green light passing through a holographic diffuser and a high-numerical-aperture lens. The lens is a plano convex (Lightpath) Gradium GPX 15-15 lens with a 15 mm diameter and 13 mm back focal length (for 532 nm light). The engineered holographic diffuser (Luminit LLC) is a disc of plastic with a thickness that varies randomly with position. This rough surface diffracts a parallel laser beam into a cone with angle w_Θ. The light is focused on the intersection of the lattice beams forming a fine-grain 3D speckle pattern with a Gaussian envelope of waist $w_S = 130$ μm. The speckle potential in a slice perpendicular (the x, y plane at the focus of the speckle beam) to the propagation direction $\vec{z}$ can be written down as

$$V_S(x, y) = V_M(x, y) e^{\frac{-2(x^2+y^2)}{w_S^2}} \tag{1.3}$$

where $V_S(x, y)$ is the (total) speckle potential, and V_M is the microscopic speckle disorder field bounded by the envelope. The size w_S of the envelope is determined by the spatial correlations of the diffuser thickness. The microscopic speckle potential V_M is determined solely by the numerical aperture of the lens and wavelength of light.

Although the microscopic speckle potential $V_M(x, y)$ is different at every point, we can characterize it by certain statistical properties. We characterize the speckle size by the two-point autocorrelation function Γ,

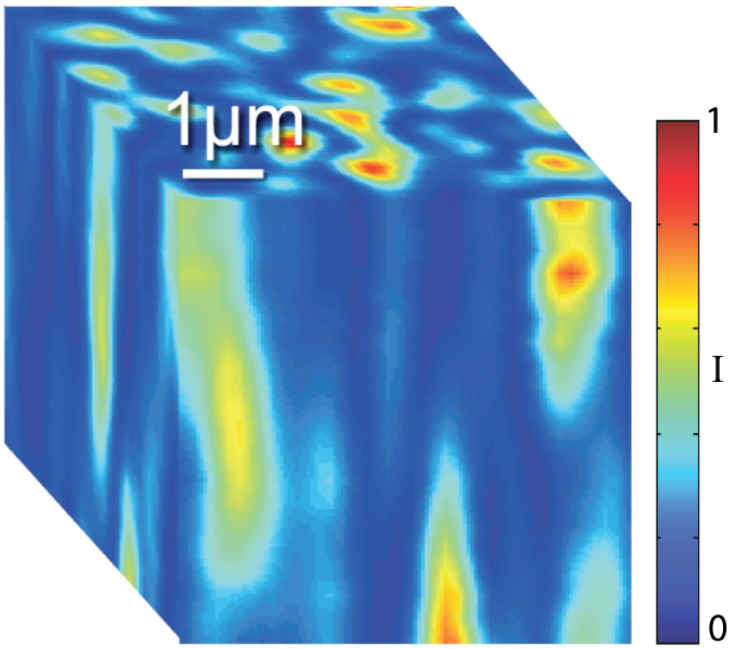

Figure 1.5 Measured intensity of the 3D speckle field. This image is composed of a stack of many images taken by a microscope on a translation stage. The intensity I is in arbitrary units between 0 and 1, indicated by the color scale on the right. The same optics as in the apparatus were used ex-situ to take these images before being integrated.

$$\Gamma(\vec{x}) = \frac{\langle I(\vec{r})I(\vec{r}+\vec{x})\rangle}{\langle I(\vec{r})\rangle^2} \tag{1.4}$$

where $I(\vec{r})$ is the intensity of light at position $\vec{r}$ with the angle brackets denoting a spatial average. For a circular aperture with constant intensity across it, Γ is best fit by a $sinc(x) = sin(x)/x$ function. However for our clipped Gaussian input intensity we found a Gaussian function is a good fit to the autocorrelation function

$$\Gamma(\vec{x}) = \frac{1}{2}[1 + e^{\frac{-x^2}{2\sigma(\vec{x})^2}}] \tag{1.5}$$

where $\vec{x}$ is the difference in position and $\sigma(\vec{x})$ is the disorder autocorrelation length along that direction. The value of σ defined here should not be confused with the value obtained from the definition $\Gamma = sinc[x/\sigma]$, the two differ by a factor of ~ 1.6 (see [13] for an example of the alternate definition). The function Γ is anisotropic for our speckle potential, with a cylindrical symmetry. The long axis has $\sigma_L = 3$ μm while the two short axes have $\sigma_T = 570$ nm each (in the convention of Ref. [13], $\sigma_L = 1.88$ μm, and $\sigma_T = 356$ nm). However along the lattice directions, which are all tilted with respect to the vertical, σ is less than twice the lattice spacing d, as shown in Figure 1.6.

A precisely known optical speckle field is key to emulating the disordered Bose-Hubbard model, as I will show in Chapter 2. To this end, we use three different methods to determine the most important characteristics of the speckle field: analytical formulas, computer simulation, and direct 3D imaging. These three methods produce consistent values for the autocorrelation function Γ, the anisotropy in Γ, the first order intensity distribution $P(I)$ of the intensity I, and the width of the speckle Gaussian envelope at the focus.

The properties of a speckle field can be calculated analytically by summing a number of random phasors [41]. The intensity maxima and minima of a speckle field at the focus of a laser beam (see Figure 1.5) are produced by the sum of all light with a random phase for each momentum component of the light field $\vec{k}$; where $\vec{k}$ is dependent on the position at which light passes through the focusing lens. To determine the width of the autocorrelation function, one only needs to know the effective numerical aperture and wavelength of light. The random phase produced by the diffuser only affects the waist envelope of the speckle field w_S, not the autocorrelation width.

The first-order intensity distribution measures the probability of a certain intensity I occurring, and is

$$P(I) = \frac{1}{\bar{I}} e^{-I/\bar{I}} \tag{1.6}$$

for an ideal speckle field, where $\bar{I}(r) = \frac{2P_s}{2\pi w_S^2} e^{\frac{-r^2}{2w_S^2}}$ is the average local intensity across the speckle field, P_s is the total power in the speckle beam, and $w_S = f w_\Theta$ is the width of the speckle envelope at the focus determined by the focal length f and the diffuser angular

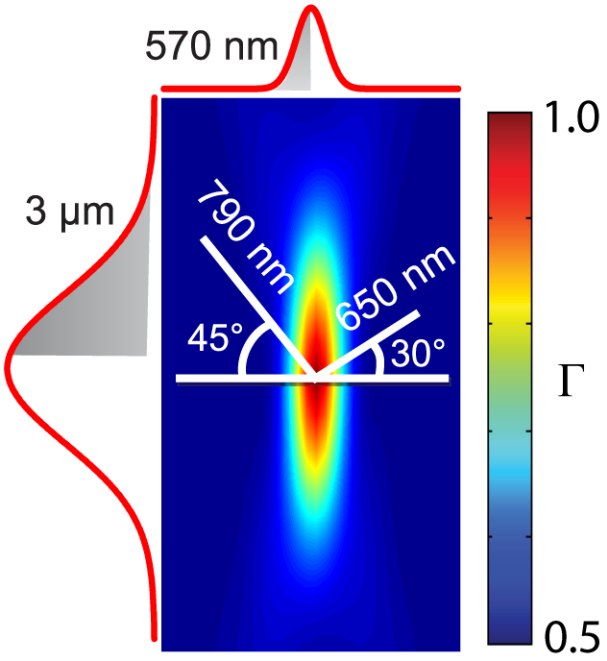

Figure 1.6 Measured two-point autocorrelation function of focused speckle light which was imaged ex-situ (see Figure 1.5). This 2D cross-section of the cylindrically symmetric 3D autocorrelation function is longer along the direction of propagation of the laser light (longitudinal) than in the two transverse directions. While the long direction has a 3 μm $1/e^2$ radius, along any of the lattice directions (white lines) the autocorrelation width is less than two lattice spacings. The color scale of the figure, indicated on the right, is between $\Gamma = 0.5$ (uncorrelated) and 1 (perfectly correlated).

width w_Θ.

The two-point autocorrelation depends only on numerical aperture and wavelength; nothing about the spatial correlations of thickness in the diffuser or aberrations in the optics affects these quantities [41]. Analytically calculating the width of Γ by summing random phasors, one can show that [41]

$$\sigma_L = 5.7\lambda(f/D)^2, \tag{1.7}$$

$$\sigma_T = 1.2\lambda(f/D), \tag{1.8}$$

$$\frac{\sigma_L}{\sigma_T} = 4.75\lambda(f/D). \tag{1.9}$$

Notice that the aspect ratio σ_L/σ_T is dependent on the numerical aperture $1/(f/D)$, where D is the diameter of the lens.

While these analytical formulas are a good first step to determining the performance of the optics used to create speckle. To produce quantitative measures of the speckle produced by optics in our experiment, we simulated the speckle field with a computer. The simulated field is produced by first creating an accurate model of the laser beam; in our case this is a Gaussian clipped by the edge of the lens and diffuser. This clipped function is then multiplied by a random phase at each pixel. This procedure will not give an accurate envelope, but will return speckle with the appropriate microscopic autocorrelation function. The matrix representing the illuminated diffuser is padded by doubling both its width and height by adding pixels with zero amplitude. Next a fast Fourier transform (FFT) is applied to the image, producing a speckle field (see Figure 1.7). Without padding, the resolution of the speckle field image is not high enough to resolve local intensity minima and maxima. From this simulation we were able to optimize the width of the collimated laser before it is incident on the high-numerical-aperture lens and diffuser. The intensity of the speckle field is decreased when a larger beam is clipped. We balanced this against the speckle autocorrelation width which increases when the laser is too narrow at the lens. By balancing these two design constraints we were able to create a lattice that was both fine-grain while retaining sufficient intensity to produced strongly disordered lattices.

The final and most important method we use to understand optical speckle is to directly image it in three dimensions ex-situ. Before integrating the speckle beam optics into the BEC apparatus, we assembled them in the same configuration on another part of the optical table. A CCD camera on a translation stage imaged the light after it had passed through the diffuser and high-numerical-aperture lens. By moving the translation stage in 240 nm steps, successive images built up the 3D intensity distribution of the speckle field. This measurement confirmed the analytical predictions and computer simulations of the speckle field for the optical components we used (see Figure 1.6). We verify that the autocorrelation function Γ of our speckle calculation matches the measured field and then use the calculation to simulate the disordered Bose-Hubbard parameters that exist in our

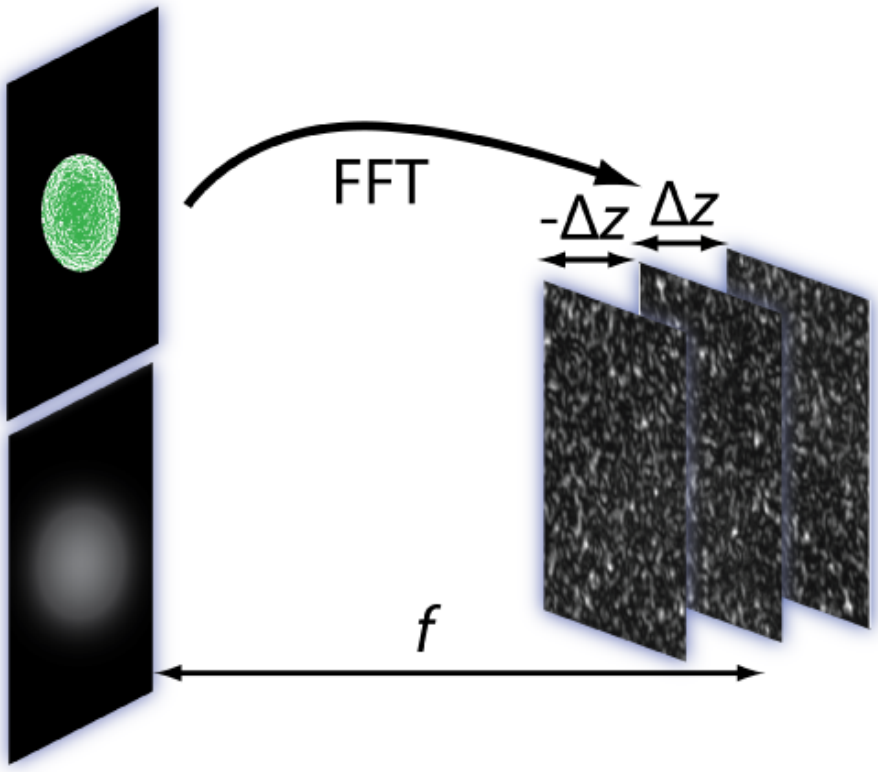

Figure 1.7 A speckle field is calculated numerically by first creating a matrix with complex phase and Gaussian amplitude representing the input laser (bottom left) modified by an aperture and random phase caused by a diffuser (top left). The propagation of light through a lens to the focus (a distance f) is equivalent to a (fast) Fourier transform (FFT). To simulate the speckle field in 3D, we calculate planes adjacent to the focus using a Fresnel transform. The Fresnel transform is accomplished by multiplying — before performing the FFT — the input field by a phase $\phi_F(\Delta z, x, y) = e^{(i\pi\Delta z)/(\lambda f^2)(x^2+y^2)}$ [42], where Δz is the distance from the focal plane to the target plane.

experimental disordered lattice (see Chapter 2) [43].

1.3.4 Imaging

Once atoms are loaded into the disordered optical lattice, we have a variety of techniques that manipulate the atoms and then record the resulting behavior. In our apparatus, all data is recorded using a CCD camera that images the atoms from two directions.

The column density (the 3D density integrated over one dimension) of the gas is found by measuring the optical depth (OD) of the atoms' shadow cast into a resonant laser beam. This procedure starts after the atoms are released from the trap — they are allowed to expand for between 5 to 30 milliseconds, the so-called "time-of-flight" (TOF). During expansion, a quantizing magnetic field of 3.1 G is maintained parallel to the imaging laser. The atoms, beginning in the $|F = 1,\ m_F = -1\rangle$ state, are transferred into the $|F = 2\rangle$ hyperfine level by applying the repump beam for less than a millisecond. Next light from the "probe" beam, resonant with the $|F = 2\rangle$ to $|F = 3\rangle$ cycling transition, is applied. The OD is measured by taking three successive images with the CCD camera. The first images the shadow from the atoms. The next two images are taken after the atoms are gone to eliminate variations in the probe beam intensity as well as stray light. The data from all three images is combined to find the OD of the atoms in the $|F = 2\rangle$ hyperfine state.

In order to reduce the OD when imaging very dense gases, we control the fraction of atoms in the $|F = 2\rangle$ state by changing the duration and detuning of the repumping pulse. Since only the atoms in the $|F = 2\rangle$ state scatter light from the imaging beam, changing the fraction of the gas in this state changes the fraction of atoms that are imaged. The rate at which atoms scatter repumping photons is proportional to the number in the $|F = 1\rangle$ manifold. Thus the number of atoms in the $|F = 1\rangle$ state N_1 decays exponentially while the repump beam is applied with an exponential decay time of $\tau(\delta_r)$, where τ is a function of the repump detuning δ_r. Thus the fraction in the $|F = 2\rangle$ state is

$$N_2/(N_2 + N_1) = 1 - e^{-t_p/\tau(\delta_r)} \tag{1.10}$$

where t_p is the length of the repump pulse. This allows us to adjust the fraction of atoms we image by controlling the pulse duration t_p and the detuning δ_r.

Two sets of optics in our apparatus form two orthogonal imaging paths that end on either the left or right partition of the CCD (see Figure 1.8). One of these directions is used mostly for alignment and calibration ("side"), while the other more sensitive set of optics is used to take quantitative data ("main"). The main imaging path is formed by a two-lens telescope with a magnification of 4.1. This magnification means that each of the 1024 by 1024 pixels on the CCD images 3.14 μm at the plane of the atoms. This resolution is slightly smaller than the 3.7 μm diffraction limited resolution [26] of the optics (defined as the $1/e^2$ width of an imaged point source). The side imaging direction has a similar

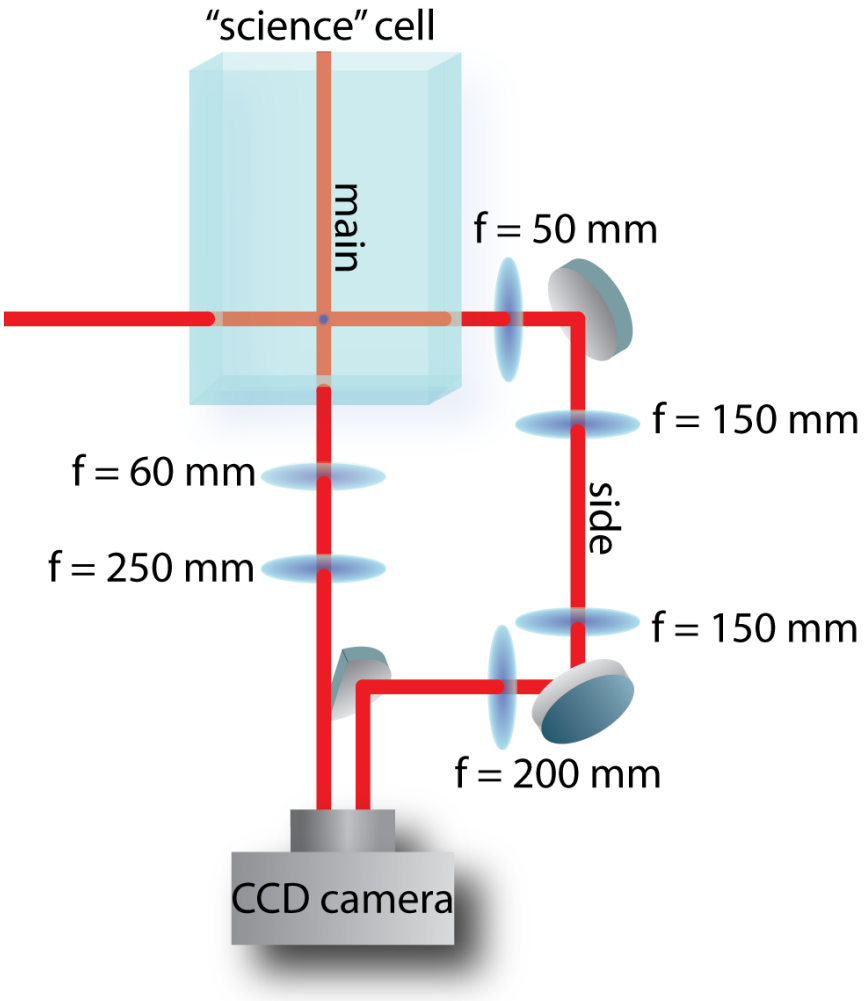

Figure 1.8 In the science cell (light blue volume) the atoms (dark spot) are imaged using two orthogonal imaging directions (red beams). Along the "main" imaging beam the light is imaged using a $f = 60$ mm focal length lens in a 4.1 to 1 telescope. For the "side" imaging direction, the light travels a longer distance which necessitates relay optics. The beams are combined onto either side of a CCD camera using an edge mirror.

magnification, but the much longer — and frequently adjusted — imaging path is noisier and has poorer resolution.

1.4 Summary of Results

1.4.1 Discovery of a Disordered Insulator in an Optical Lattice

As stated in section 1.2, our work is motivated by the desire to emulate models of condensed matter using ultra-cold atoms. In our work, a gas of ^{87}Rb atoms confined in a disordered lattice will serve as an emulator for the disordered Bose-Hubbard model. By studying the transport properties of the gas in lattice, we made a quantitative measurement of a superfluid-to-insulator transition in the presence of disorder. Specifically, we observed that a disordered insulator appears for sufficiently high disorder strength in the strongly quantum depleted superfluid regime.

The phase diagram of the disordered Bose-Hubbard model — reviewed in Chapter 2 — has a few outstanding questions which are unresolved theoretically. Although the regime of unit filling at zero temperature has been studied extensively, the features of the phase diagram (especially in 3D) with finite-temperature, non-unit filling, or with certain kinds of realistic disorder are unknown. Our experiment constrains the theory of the disordered Bose-Hubbard model by measuring the transport properties of the center-of-mass of the gas in the lattice. We explored the space of Bose-Hubbard parameters along two axes. On one axis, we varied the lattice depth to change the ratio of tunneling energy to interaction energy. The other axis we varied was the disorder strength. Using the center-of-mass (COM) velocity as a measure of dissipation, we map out the transition between superfluid and highly dissipative insulating phases.

Our measurements found a disordered insulator at $\Delta = 3\ E_R$ for $s \gtrsim 12\ E_R$; this measurement is quantitatively similar to theoretical predictions. However, our results in other parts of the phase diagram [44] did not show the same agreement with theory [23]. For low lattice depths, the gas remained a superfluid even for the highest disorder strengths we measured. At high lattice depths, we did not observe a "re-entrant" superfluid phase that was predicted to exist for small disorder strengths. In Chapter 3 these transport measurements will be discussed and compared with theory. The characteristics of our experiment that may explain the deviation of our results from recent quantum Monte-Carlo numerical simulation are also explored.

1.4.2 A Method for Producing High-Accuracy Holographic Traps for Cold Atoms

A disordered lattice is just one type of potential that can be created with far-off-resonance lasers. Using an electronically controlled hologram generator called a spatial light modulator

(SLM) (see Figure 4.3), an endless variety of arbitrary potentials can be created (see, for example, Refs [45, 46]). These traps could also allow us to investigate new lattice structures (see, for example, [47]). Alternatively, SLMs could create "atomtronic devices" [48].

Soon after I came to Illinois we investigated holographic atom traps. We discovered a crucial obstacle to creating these traps using an SLM. The SLMs needed a rasterized 2D phase map — called a kinoform — to manipulate the laser beam. However, the algorithms available to create these kinoforms could only create traps with full intensity speckle. These traps were not nearly smooth enough for use with ultra-cold atoms. To solve this problem we invented a new algorithm suited to trapping ultra-cold atoms. It is able to produce kinoforms that are free of speckle and far smoother than anything previously demonstrated [49].

The algorithm we developed is called the "mixed region amplitude freedom" (MRAF) algorithm. It is a variant of the class of iterative Fourier transform algorithms (IFTAs). To measure its performance in the context of ultra-cold atom traps compared to these existing algorithms, we developed a new set of metrics. We evaluated our new method against existing ones on the following bases:

- efficient use of laser light,
- accuracy of reproduction,
- roughness.

Roughness is an entirely new metric we developed which measures how suitable a potential is as an atom trap. Our new algorithm produced traps with superior accuracy and lower roughness than existing algorithms, at the expense of decreased efficiency.

At the time we investigated this technique, SLMs were not capable of reproducing the kinoform with high enough accuracy to take advantage of our new algorithm. In the years since, SLM performance has improved enough to produce usable holographic traps. Recent work at St. Andrews [50] reproduced, using an SLM, a ring trap we proposed [49]; the predicted and measured intensity show excellent agreement (see Figure 1.10).

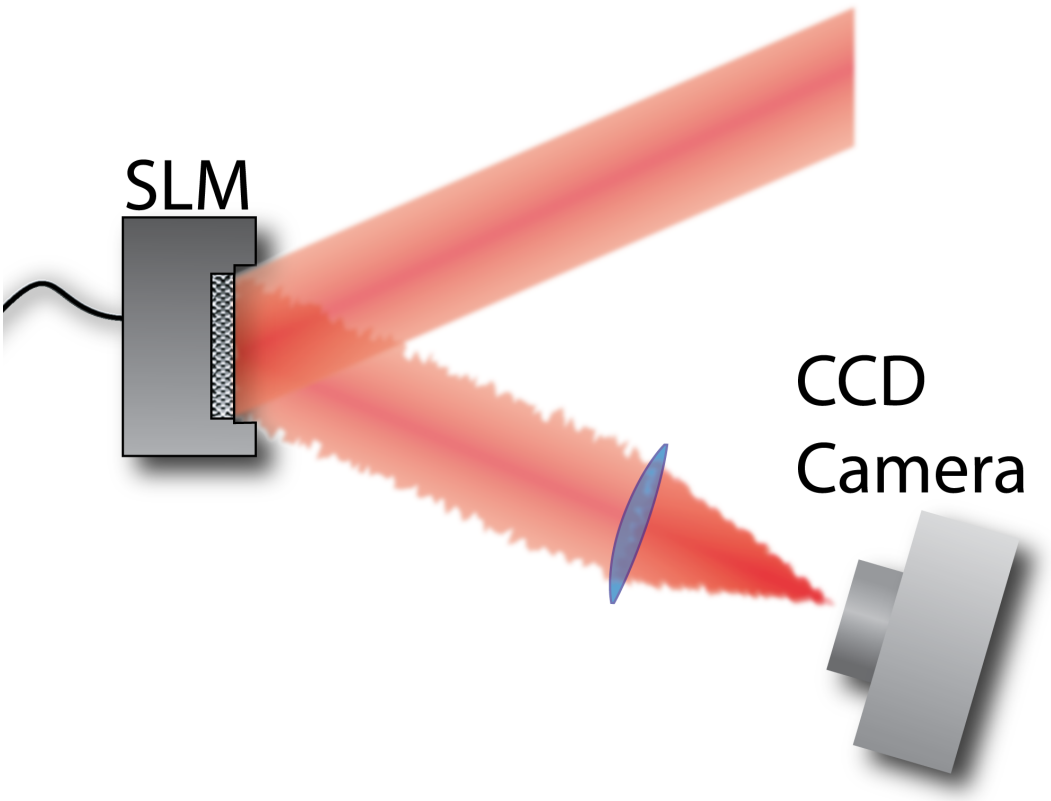

Figure 1.9 A laser beam incident on an SLM, filling the active surface. The surface of the SLM imprints the phase of the displayed kinoform on the light. The beam is focused onto a camera which images the resulting hologram intensity. Alternatively, the system could be integrated into a atomic physics experiment, with a cold atom gas in place of the camera.

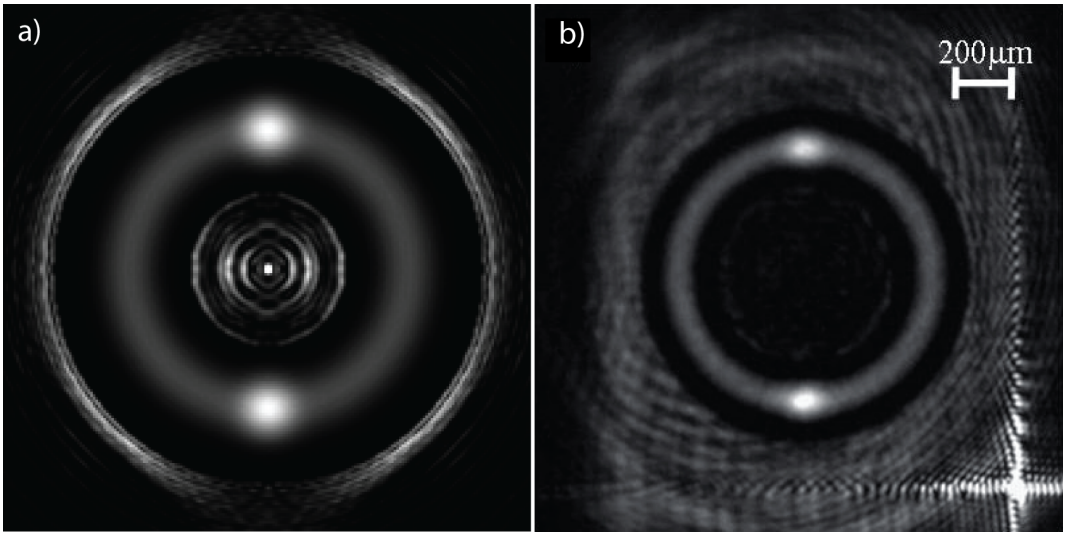

Figure 1.10 A theoretical hologram (**a**) from our 2008 paper [49] demonstrating an algorithm to produce holographic atom traps and an experimental reproduction of the same pattern (**b**). The mixed region amplitude freedom (MRAF) algorithm only constrains the intensity of light in the region where atoms will be present. In the intensity pattern predicted by our MRAF algorithm (**a**), atoms are intended to fill the Gaussian ring with two more intense Gaussian spots. Recently, our MRAF algorithm has been used with an SLM to experimentally produce this intensity pattern at St. Andrews (**b**) [50]. These traps can be used to stir a superfluid while confining it in a ring trap.

Chapter 2

Disordered Bose-Hubbard Model

2.1 Introduction

Cold atoms in the disordered optical lattice we create are described by the disordered Bose-Hubbard model [51]. Theoretical work over the last two decades (see discussion in Section 2.3) has left some open questions regarding this model, such as the nature of a disordered insulator and the presence of a "re-entrant superfluid". The purpose of our research is to use the extremely simple and well understood ultra-cold-atom-gas lattices to resolve questions about the behavior of systems described by the disordered Bose-Hubbard model. These experiments can illuminate how disorder and interactions combine to produce quantum phase transitions in the disordered Bose-Hubbard model.

The disordered Bose-Hubbard model describes bosons on a lattice considering only kinetic energy, short range interactions, and potential energy. This simplification ignores some factors that may play a significant role in solids such as magnetic fields, charge, higher bands, long-range interaction, and long range hopping. The most general disordered Bose-Hubbard Hamiltonian is,

$$H = -\sum_{\langle ij \rangle} t_{ij} b_i^\dagger b_j + \sum_i (\epsilon_i - \mu) n_i + \sum_i \frac{U_i}{2} n_i (n_i - 1), \tag{2.1}$$

where t_{ij} is the tunneling energy between neighboring sites i and j, U_i is the interaction energy on site i, b_i is the annihilation operator for site i, ϵ_i is the on-site energy including the trapping potential, μ is the chemical potential, and $n_i = \langle b_i^\dagger b_i \rangle$ is the number per site. In the disordered Bose-Hubbard model, disorder can cause t, U, and ϵ to be site-dependent, as indicated by the subscript. The parameter Δ measures the spread in in ϵ_i. For example, a bounded, uniform distribution of ϵ between $-\Delta$ and Δ is used in many theoretical treatments. While disorder in U is not usually considered theoretically, calculations of the disordered lattice in our experiment show disorder in all Bose-Hubbard parameters (see Section 2.2.1). Additionally, the gas is trapped in the disordered lattice by a harmonic potential, creating an inhomogeneous density profile. To relate the results from the Bose-Hubbard model in the thermodynamic limit, we will therefore need to use the local density approximation, as discussed in Section 2.2.4.

This model with just three parameters — characterizing the competition between kinetic

energy, interaction energy, and disorder — produces several quantum phase transitions. The "clean" Bose-Hubbard model in the limit $\Delta = 0$ E_R produces the well known Mott-insulator-to-superfluid phase transition at zero temperature [20]. When disorder is non-zero, the Bose-Hubbard model produces a richer phase diagram including new phases such as the Bose glass — a compressible insulator. Increasing disorder can turn the Mott insulator or superfluid into a Bose glass [20, 52, 53], but it may also turn a Mott insulator or Bose glass into a so-called "re-entrant superfluid" [22].

The disordered Bose-Hubbard model was formulated to understand unexplained phenomena in superfluids. An example superfluid is liquid ^{4}He, the first system in which Bose-Einstein condensation was observed [54–56]. Soon after the discovery of superfluidity, experiments (like the observation of the fountain effect [57]) began transporting liquid Helium through emery powder, a fine-grain disorder network. Experiments in the 1980s [58, 59] looked at liquid ^{4}He adsorbed onto engineered disordered substrates that, unlike emery powder, had well defined and controllable grain-size. Here, by changing the disordered network from one that was mostly substrate (Vycor) to one that was mostly empty (aerogel), changes in superfluid transport and critical temperature were observed [60–62]. The disordered Bose-Hubbard model has also been used to study supersolidity in ^{4}He [17, 18]. When the solid is annealed to decrease the amount of disordered fissures, the non-classical rotational inertia that characterizes the supersolid effect is no longer observed [63, 64]. From these examples it is apparent that disorder affects the transport properties of strongly interacting bosons.

The first theoretical inquiry was by Giamarchi and Shulz [52], who studied bosons in a disordered lattice using the renormalization group and found a ground state that included the Bose-glass phase when disorder was present, in addition to Mott insulator and superfluid phases (see Figure 2.6). Fisher et al. [20] wrote down the disordered Bose-Hubbard Hamiltonian (as in Eq. 2.1) in 1989 and produced the first candidate phase diagrams (see Figure 2.7) in terms of the chemical potential and Bose-Hubbard parameters. The theoretical work that followed these early results is summarized in Section 2.3. As we will discuss, the many different techniques used to study this model predicted qualitatively different phase diagrams. Several features, such as the existence of a direct Mott-insulator-to-superfluid phase transition in the presence of disorder, are still being debated [65].

Ultra-cold atoms in a disordered lattice are an important innovation in the study of the disorder Bose-Hubbard model, because the optical lattice potential can be measured precisely and the interactions between atoms are well-understood. The connection between Hubbard models and atoms in optical lattices was first shown theoretically in 1998 Jaksch et al. [66]. Four years later, Greiner et al. [36] experimentally realized the clean Bose-Hubbard model, measuring the superfluid-to-Mott-insulator transition using ultracold ^{87}Rb atoms. Experiments on disordered bosons were later conducted in one dimension by adding either optical speckle fields [1, 3, 4, 7, 8]; related work employed an additional incommensurate

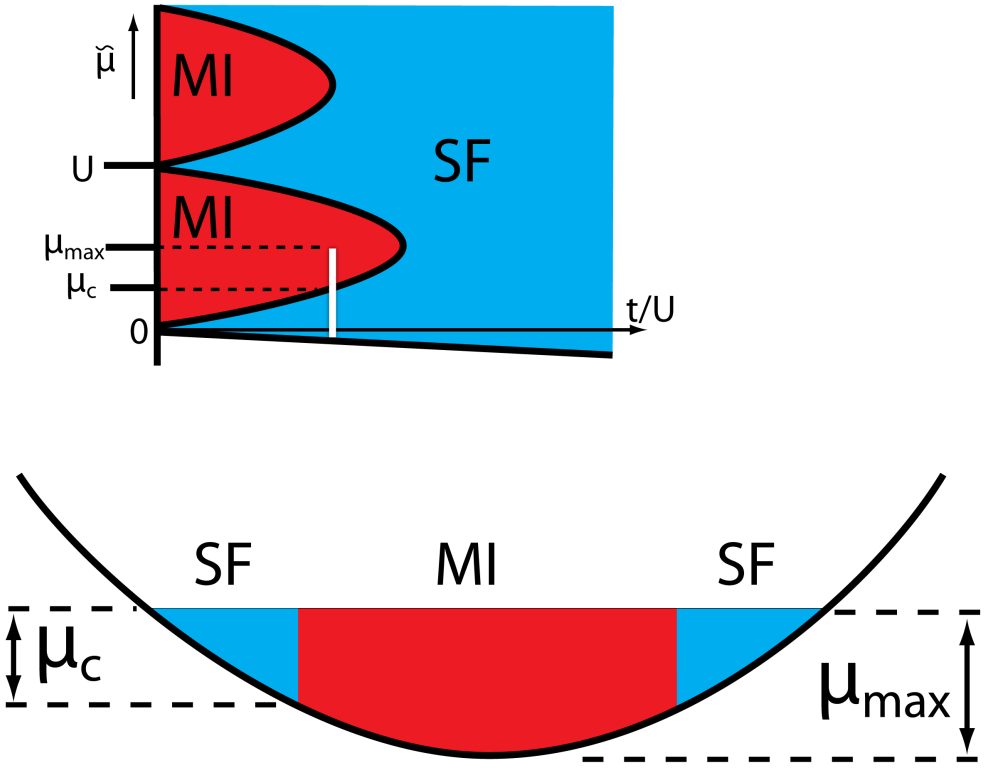

Figure 2.1 The clean Bose-Hubbard phase diagram (top) shows the range of chemical potentials for a gas in a $s = 14\ E_R$ lattice with a maximum density $n = 1$ corresponding to maximum chemical potential μ_{max} (indicated by the white line). Where the effective chemical potential $\tilde{\mu} > \mu_c$, the gas is a Mott insulator. At bottom, the same gas is show in the harmonic trap. The regions at lower effective chemical potentials at the edge of the gas are superfluid, while at the center, the gas is a Mott insulator. We use this configuration of phases for the results discussed in this dissertation.

lattice [2, 9, 10]. Neither was described by the disordered Bose-Hubbard model. By removing interactions using a Feshbach resonance [67, 68], or using an extremely dilute gas, the groups in Florence and Orsay were able to realize Anderson localization in an ultracold atomic vapor for the first time [13, 14]. Our work builds on these results by examining the effects of disorder on a strongly interacting gas in a 3D lattice, a regime that has not yet been explored using ultra-cold atoms.

Our experiment, which confines atoms in a harmonic trap, cannot be compared directly to theoretical predictions with homogenous density in the lattice. Instead of using a constant chemical potential μ for the entire gas, we define a spatially varying effective chemical potential $\tilde{\mu}(r) = \mu - V(r)$ where $V(r)$ is the harmonic potential at radius r [69]. Figure 2.1 shows how as $\tilde{\mu}$ changes with radius (bottom), the gas in a harmonic trap samples different regions of the Bose-Hubbard phase diagram (top). Section 2.2.4 will show how we take into account the inhomogeneous radial density profile of our trapped gas to calculate its properties in a clean lattice using the local density approximation.

To connect our experiment with existing research on the disordered Bose-Hubbard model, we must also calculate the experimental values of the Bose-Hubbard parameters ϵ, U, and t. In Section 2.3.4 I discuss a collaboration with the Ceperley group who used imaginary time projection methods [43] to translate the experimentally measured potential in our experiment to the disorder distributions useful to theorists. This precise description of disorder in an experiment is usually not possible in a condensed matter system where microscopic disorder and Bose-Hubbard parameters cannot be measured easily.

2.2 Clean Bose-Hubbard Model

An understanding of the clean Bose-Hubbard model and the phases present at $\Delta = 0$ E_R is a useful starting point before considering disordered phases. For a clean, three-dimensional lattice, mean-field theory calculates the clean phase diagram with high accuracy [70]. We employ this mean-field theory to estimate the density, compressibility, and entropy in a clean, harmonically trapped lattice. In a harmonic trap, the density of the gas varies with position, largest at the center and decreasing toward the edge. The Bose-Hubbard phase diagram is density dependent (see Figure 2.2), so controlling the number of atoms in the gas to produce a specific density is necessary to maintain a given maximum density. This is important because many of the theoretical phase diagrams we wish to compare to are at unit filling [23]. As we change the lattice depth, the number of atoms necessary to maintain unit filling in the center of the trap changes because of increased interactions and increased harmonic-trap strength (see Figure 2.3). By calculating the density profile of the gas for a range of lattice depths and harmonic trap frequencies, we can adjust the number of atoms in the lattice to maintain a fixed maximum density. We also convert condensate fraction N_0/N observed in time-of-flight imaging to in-trap entropy-per-particle S/N. Although we

are not able to directly calculate properties of the disordered lattice with this numerical technique, we at least have a well-defined starting point as we increase Δ.

The "clean" single-band Bose-Hubbard Hamiltonian is,

$$H = -t \sum_{\langle ij \rangle} b_i^\dagger b_j + \sum_i (\epsilon_i - \mu) n_i + \frac{U}{2} \sum_i n_i (n_i - 1). \tag{2.2}$$

In contrast to the disordered Hamiltonian, the clean Bose-Hubbard parameters, t and U are site independent. The gas is well-described by a single-band model for the lattice depths and temperatures in our experiments.

The many-body state of the Bose-Hubbard model is determined by the competition between the kinetic energy, proportional to t, and the interaction energy, proportional to U. When the interaction energy U dominates the tunneling energy t, the total energy is minimized by localizing a constant integer number of atoms to each site — a Mott insulator. When $U/6t < 5.8$, the ground state energy is minimized by delocalizing atoms which Bose-condense and form a superfluid [20].

2.2.1 Bose-Hubbard Parameters

The Bose-Hubbard parameters which specify the Hamiltonian must be computed to model the gas in the optical lattice. The single particle energy eigenstates of a periodic lattice are Bloch states, which are completely delocalized extended states (see, for example, [66]). The Bose-Hubbard model assumes that atoms are in the lowest band of the lattice and tunnel only to their nearest neighbor in a lattice with discrete sites. In reality, the atomic wavefunctions are not discrete. To model a continuous wavefunction as a discrete set of lattice sites, we pick a low-energy localized basis from which we can calculate the Bose-Hubbard parameters. This basis is produced by the appropriate superposition of Bloch waves: the localized Wannier wavefunctions

$$w(\mathbf{r} - \mathbf{R}_i) = \frac{1}{\sqrt{N}} \sum_{\mathbf{k}} \psi_{\mathbf{k}}(\mathbf{r}) e^{-i\ \mathbf{k}\cdot\mathbf{R}_i}, \tag{2.3}$$

where $\mathbf{r}$ is position, $\mathbf{R}_i$ is the center of the i^{th} lattice site, and $\psi_{\mathbf{k}}(\mathbf{r})$ are the Bloch functions of the ground band with quasimomentum $\mathbf{k}$.

Using the Wannier states calculated for a given lattice depth, we can calculate the Bose-Hubbard parameters [66],

$$t = \int d^3\mathbf{r} w^*(\mathbf{r} - \mathbf{R}_i) \left(-\frac{\hbar^2}{2m}\nabla^2 + V_0(\mathbf{r}) \right) w(\mathbf{r} - \mathbf{R}_j) \tag{2.4}$$

$$U = 4\pi \frac{a_s}{m} \hbar^2 \int d^3\mathbf{r} |w(\mathbf{r} - \mathbf{R}_i)|^4 \tag{2.5}$$

$$\epsilon_i = \int d^3\mathbf{r} w^*(\mathbf{r} - \mathbf{R}_i)[-\frac{\hbar^2}{2m}\nabla^2 + V_0(\mathbf{r})]w(\mathbf{r} - \mathbf{R}_i), \tag{2.6}$$

where V_0 is the potential energy, a_s is the s-wave scattering length, and m is the atomic mass. The potential V_0 is composed of a sinusoidal potential with high spatial frequency, and a smooth harmonic potential. The harmonic potential changes slowly enough that it can be ignored when calculating the Bose-Hubbard parameters.

2.2.2 Clean Phase Diagram

The phase diagram of the clean, zero-temperature uniform Bose-Hubbard model has two control parameters, the chemical potential μ and ratio zt/U, where the coordination number z is the number of nearest neighbors (in 3D, $z = 6$). Increasing the lattice depth causes the interaction energy to increase and the hopping energy to decrease exponentially [66]. In this section I will describe the distinguishing characteristics of the Mott-insulator and superfluid phases that appear as μ and t/U are varied. When t is large, it may be energetically favorable for atoms to exist at a negative chemical potential. Thus, in Figure 2.2 the phase diagram is displayed using $(\tilde{\mu}+6t)/U$ instead of $\tilde{\mu}/U$ for the vertical axis so that the density is zero along the abscissa.

The superfluid phase has a non-zero conductivity and finite condensate fraction N_0/N, where N_0 is generally (we will use a slightly different but equivalent definition later when describing the experiment) the number of atoms in the lowest energy single-particle macroscopically occupied eigenstate, and N is the total number of atoms. For a finite-size sample, the conductivity is not infinite due to phase slips [71]. Apparent in Figure 2.2, interactions reduce the fraction of atoms in the condensate, an effect known as quantum depletion. Further distinguishing the superfluid from a Mott insulator, the compressibility of the superfluid state is finite [20].

The Mott insulator consists of atoms localized to single sites with uniform integer density. It is distinguished from other insulators (e.g., the disordered Bose glass) by its incompressibility. The lack of compressibility is caused by a gap in the density of states, proportional to the interaction energy U, the Mott gap [20].

The Mott gap is the energy associated with the creation of a particle and hole at neighboring sites requiring energy E_p+E_h. The gapped system is insensitive to excitations below the finite Mott gap energy; thus the system is incompressible and insulating. In the limit $t \ll U$ the energy E_p to add a particle to a site with n atoms is the difference in energy for $n+1$ and n particles at that site. Similarly the hole energy E_h is the difference in energy

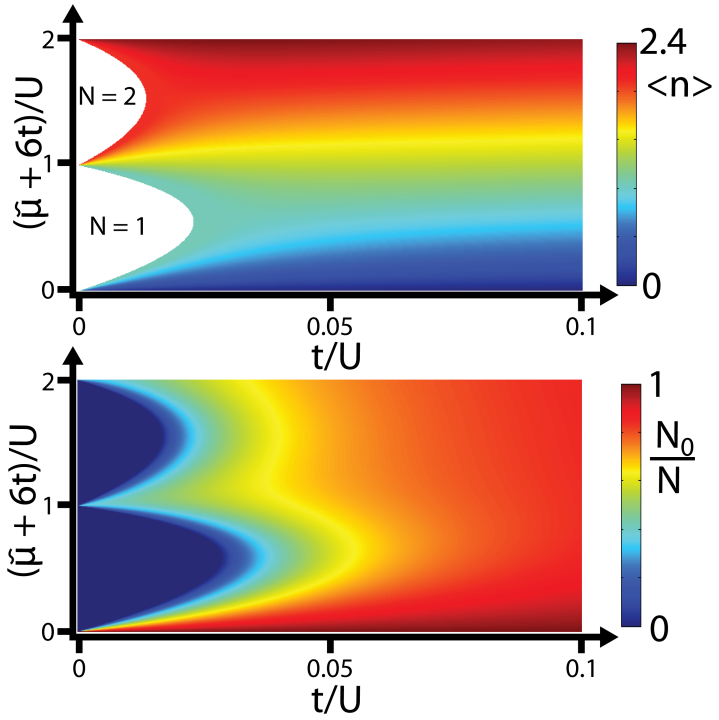

Figure 2.2 Particles per site (top) and condensate fraction (bottom) calculated by site-decoupled mean-field theory at zero temperature. In the white regions, condensate falls to zero and the density is integer valued, indicating a Mott insulator with N particles. The areas with finite condensate fraction are superfluid. The vertical scale uses $(\tilde{\mu} + 6t)/U$ so that zero-density is on the x-axis. The density in our harmonic trap varies from roughly one atom per site in the center to zero at the edge.

between $n-1$ and n atoms per site. For $t \ll U$,

$$E_p = \frac{U}{2}(n+1)(n) - \frac{U}{2}(n)(n-1) = U \cdot n, \tag{2.7}$$

$$E_h = \frac{U}{2}(n-1)(n-2) - \frac{U}{2}(n)(n-1) = -U(n-1), \tag{2.8}$$

$$E_p + E_h = U. \tag{2.9}$$

Thus, in this regime, this Mott gap is proportional to the interaction energy U. This is why the range of each Mott lobe (see Figure 2.2) has width $\Delta\mu = U$ in the limit that $t \to 0$.

A distinguishing characteristic of the two "clean" phases is the compressibility, defined as the infinitesimal change in density associated with an infinitesimal change in chemical potential [72]

$$\kappa = \frac{\partial n}{\partial \mu}. \tag{2.10}$$

When a gap is present, as in the Mott insulator, the compressibility is zero, and over a finite range of μ the density is fixed. For a gas in a harmonic trap, as in our experiment, the compressibility is related to the derivative of the density [73]

$$\kappa = -\frac{n'(r)}{rm\omega^2}, \tag{2.11}$$

where $n'(r)$ is the spatial derivative of density, ω is the harmonic trap frequency, r is the radial position from the center of the harmonic trap, and m is the mass of the atom. In a Mott insulator the density is constant so $\kappa = 0$, while for a superfluid $\kappa \neq 0$.

The fluctuation-dissipation theorem also relates number fluctuations to the compressibility of the gas [74]

$$\delta n^2 \approx \kappa k_B T. \tag{2.12}$$

Equations 2.10, 2.11, and 2.12 give three different ways to measure the compressibility of a gas:

- The trap frequency may be varied, increasing the maximum chemical potential, and consequently the size of the gas or maximum filling may change.
- The density profile can be measured, in situ, when a harmonic trap is present.
- The density fluctuations may be measured at a known temperature.

The last two methods have been demonstrated in two dimensions [73].

2.2.3 Mean-Field Calculation

This section will describe the site-decoupled mean-field theory (SDMFT) (i.e., Gutzwiller ansatz) [66, 75, 76] we use to simulate density profiles for a harmonically trapped gas (see Section 2.2). We use the results of SDMFT for the clean lattice to control the central density (to one atom per site) by adjusting the number of atoms N as the lattice potential depth is varied. However, a SDMFT calculation cannot directly predict density for the disordered lattice. We cannot do this because a verified theory of the disordered Bose-Hubbard model does not exist. Therefore, this calculation is used a effective substitute. We have several reasons to expect that the central density is not strongly affected by the application of disorder. First, the measured diameter of the gas does not change significantly when disorder is applied. Second, the broad envelope of the speckle field produces an unimportantly small change in the harmonic trap confinement. Therefore the disorder only leads to a potential offset, which is unlikely to affect the chemical potential. Finally, if this approach is not perfect, it likely reasonably close; we find that the disorder required to drive the superfluid-insulator transition closely matches QMC at unit filling [23].

Following Refs. [76–78], we apply a Gutzwiller ansatz to the clean Bose-Hubbard Hamiltonian (Equation 2.2)

$$|\phi_i\rangle = \sum_{n=0}^{m} f_n^{(i)} |n_i\rangle, \tag{2.13}$$

where $|\phi_i\rangle$ is the state on site i composed of number states $|n_i\rangle$. The calculation is truncated to a maximum m atoms per site. We replace the hopping operators with a decoupled approximation

$$a_i^\dagger a_j = \langle a_i^\dagger \rangle a_j + \langle a_j \rangle a_i^\dagger + \langle a_i^\dagger \rangle \langle a_j \rangle. \tag{2.14}$$

This substitution produces a mean-field Hamiltonian

$$H_i^{MF} = \frac{U}{2} \hat{n}_i(\hat{n}_i - 1) - \mu \hat{n}_i - t\psi(a_i + a_i^\dagger) + t|\psi|^2, \tag{2.15}$$

where $\psi = \langle a_i \rangle$ is the mean field parameter. When the mean-field Hamiltonian is expanded in the $|n_i\rangle$ basis, terms with increasing expectation value of $\hat{n}_i$ are on the diagonal, and terms proportional to the nearest-neighbor creation (annihilation) on the upper (lower) off-diagonal. The matrix is truncated at a high enough atom number m such that the result of the calculation does not change by increasing the number further.

We solve the Hamiltonian variationally by changing the value of the mean-field parameter ψ to minimize the lowest energy eigenvalue. The expectation value of this mean-field parameter squared is the condensate density (Eq. 2.19). The condensate density is non-zero when the state is a superfluid, and vanishes when it is a Mott insulator. The eigenvector associated with the smallest eigenvalue represents the number of atoms at each site. A su-

perfluid is not an eigenstate of the number basis, and will have a nonzero variance $\langle n - \langle n \rangle \rangle^2$ in the atom number. When $t = 0$ or $\psi = 0$, the Hamiltonian is diagonal in the number basis, and the variance in the number per site is zero, i.e., a Mott insulator.

The condensate density is the expectation value of the creation operator squared:

$$\psi = \langle \phi_i | a | \phi_i \rangle \tag{2.16}$$
$$= \sum_n \sum_l f_i^n f_i^l \langle n | a | l \rangle \tag{2.17}$$
$$= \sum_n f_i^n f_i^{n-1} \sqrt{n} \tag{2.18}$$
$$n_0 = |\psi|^2. \tag{2.19}$$

where n_0 is the number of particles in the condensate per site. When the temperature is non-zero, the thermal state is a sum of eigenstates with energies ϵ_i [79],

$$\langle n_0 \rangle = \left(\sum_i e^{-\epsilon_i \beta} \sum_n f_i^n f_i^{n-1} \sqrt{i} \right)^2 / Z^2 \tag{2.20}$$
$$Z = \sum_i e^{-\epsilon_i \beta} \tag{2.21}$$

Where $\langle n_0 \rangle$ is the thermally weighted sum of the creation operator expectation values, equivalent to the condensate density at finite temperature. The canonical partition function Z is used as opposed to the grand canonical because the number of particles in each eigenstate is fixed. Entropy is calculated as

$$S = k_B(\ln Z + \beta u), \text{ where} \tag{2.22}$$
$$u = \sum_i \epsilon_i e^{-\epsilon_i \beta} / Z. \tag{2.23}$$

This calculation of entropy assumes that the gas is in thermal equilibrium after ramping up the lattice. Time-dependent calculations [80] show that for lattice depths at which $U \geq t$ the system may reach a non-equilibrium steady state. Thus, the method we used to calculate entropy is likely most accurate in the superfluid regime [79]. This calculation also does not account for low energy excitations such as phonons and therefore may overestimate the condensate fraction at low temperature. These can be captured accurately by dynamical mean-field theory, although only in the limit that density $n \gg 1$ [81].

2.2.4 Calculations Including a Harmonic Trap

We use the results of SDMFT calculations to simulate our experiments by taking into account the effects on the gas from the harmonic trapping potential. The gas is most dense in the center of the trap, and the density vanishes where the trapping potential energy is equal to the chemical potential of the gas, as shown in Figure 2.1. Because the phase diagram is dependent on the changing effective chemical potential, the trap is divided into concentric shells of different phases [66, 69]. We find the in-trap density profile by treating each site in our trapped lattice as if it had the same properties as a site in an infinite homogeneous lattice, i.e., the local density approximation [82]. It should be noted that the local density approximation has been shown to break down near phase boundaries, at least in 2D [83]. We assign an effective chemical potential $\tilde{\mu} = \mu - \frac{1}{2}m\omega^2 r^2$ to each point and use the density, condensate fraction, and entropy calculated with the SDMFT. The local density approximation assumes that the harmonic potential $V_T(r) = \frac{1}{2}m\omega^2 r^2$ varies slowly enough that the local phase of the atoms can be calculated as if it were part of an infinitely large homogenous region.

The lattice itself changes the harmonic trapping potential, where ω_T is the bare harmonic potential without the lattice. The varying intensity across the Gaussian optical lattice beam creates an additional harmonic potential with frequency [84],

$$\omega_L^2 = \frac{4E_R}{mw_L^2}(P_\delta 2s - \sqrt{s}) \tag{2.24}$$

where w_L is the Gaussian waist of the lattice beam, $E_R = \frac{\hbar^2 k^2}{2m}$ is the recoil energy of the lattice, and m is the atomic mass, s is the lattice depth, and $P_\delta = 1$ when the lattice is red detuned and zero otherwise. The two frequencies add in quadrature to give a combined trap frequency $\omega_{tot} = \sqrt{\omega_T^2 + \omega_L^2}$.

To calculate the number of atoms necessary to create a certain maximum density (e.g., $\langle n \rangle = 1$, as shown in Figure 2.3) we self-consistently solve for the radial density profile (see Eq. 2.25). We select a maximum chemical potential μ_{max} which determines the function $\tilde{\mu}(r) = \mu_{max} - \frac{1}{2}m\omega^2 r^2$. The total number, average condensate fraction, and average entropy per particle in the ensemble are calculated by summing over all three dimensions. To solve for the maximum chemical potential μ we determine the number by integrating the radial density $\rho(r)$,

$$N = \frac{4\pi}{(\lambda/2)^3}\int \rho(r) r^2 dr. \tag{2.25}$$

and change μ until N is equal to the desired number of atoms.

Finite temperature changes the Bose-Hubbard phase diagram. For example, as the temperature is increased, T_c for the superfluid drops to zero as $U \to U_c$ [75]. The Mott insulator is less sensitive; thermal effects allow the number to fluctuate at a higher energy scale

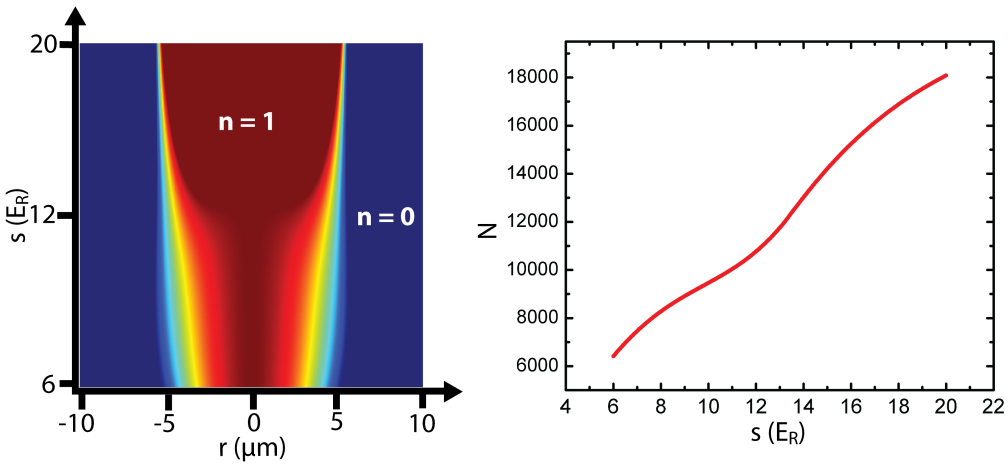

Figure 2.3 Radial in-trap density profile (left) for a central filling of 1 particle per site, for varying lattice depth. These profiles were calculated to keep the maximum density fixed for different lattice depths s. Because the radial density profile changes as s changes, the total number of particles N in the trap must be adjusted as well (right). Calculated for a trap with frequency $\omega = 2\pi \cdot 40$ Hz at zero temperature.

($k_B T \sim U$) [69, 70, 85], corresponding to roughly twice the highest critical temperature of the superfluid in our experiments. We used a finite temperature calculation to estimate the temperature and entropy per particle based on measured number and condensate fraction at a given lattice depth. The temperature of the gas is not constant while the lattice changes; adiabatically varying the lattice depth changes the density of states by flattening the bands and thus lowering the temperature of the gas [86, 87]. Due to this changing temperature we cannot estimate the in-lattice temperature by simply measuring the temperature after we release by adiabatically turning off the lattice. However, the second-law of thermodynamics allows us to use the entropy per particle S/N after such an adiabatic release from the lattice as an upper bound on the S/N in lattice.

To estimate the entropy per particle S/N in a clean lattice, we compare condensate fraction N_0/N between theory and experiment. Given the experimentally determined parameters such as number N, trap frequency ω, lattice depth s, and N_0/N, we find S/N by solving for N_0/N at different temperatures in our SDMFT calculation. As shown in Figure 2.4, N_0/N decreases as the temperature is increased. As that figure shows, condensate only exists in the superfluid region of the trap. Strong quantum depletion near the Mott-insulating phase both reduces the condensate fraction and the temperature at which the condensate disappears — as compared to the weakly interacting superfluid regime. Temperature can be determined by matching predicted N_0/N from experiment with theory. Figure 2.5 shows experimentally measured N_0/N from which S/N has been determined using this SDMFT calculation. These data are useful for characterizing the accuracy of entropy estimation using the second law of thermodynamics [44]. Note that problems with this method have been discussed in Ref. [79].

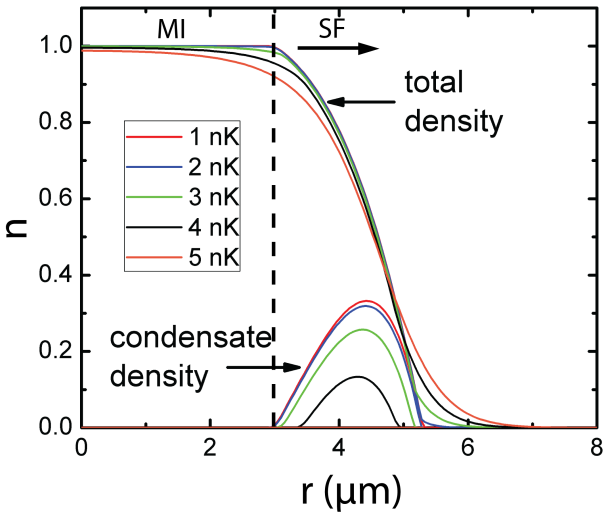

Figure 2.4 Profiles of radial density n and condensate density at finite temperature. Calculated for a $s = 14\ E_R$ lattice with wavelength $\lambda = 812$ nm and $2\pi \cdot 40$ Hz external harmonic trap. Condensate density goes to zero as the state crosses the critical temperature of ~ 4.5 nK. For small values of radius (r) (to the left side of the vertical dotted line) the state is a Mott insulator (MI); at the edge of the cloud the lattice is superfluid (SF) at low temperature.

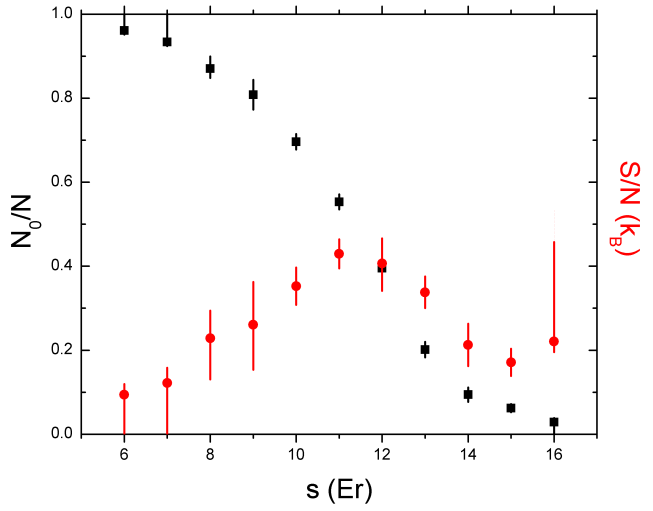

Figure 2.5 Entropy per particle in a clean lattice (red) is deduced from experimentally measured condensate fraction (black). As the entropy per particle at a fixed lattice depth increases, the condensate fraction falls. Using a finite-temperature mean-field theory simulation of our lattice, we calculate the temperature of the the lattice by matching experimental and calculated condensate fraction at a given lattice depth. Once the temperature is known, the entropy per particle is calculated.

An interesting consequence of the local density approximation (LDA) is that average quantities in a harmonic trap are only dependant on the maximum chemical potential at the center of the trap. Thus, it is possible to make "state diagrams" for gases trapped in arbitrary quadratic trap potentials [74, 82]. This is discussed in more depth in Appendix 1.

2.3 Disordered Bose-Hubbard Model

The nature of the interplay of disorder and interaction in many-body quantum mechanical systems is an important and open question. In strongly interacting bosonic systems, related phenomena may be captured by the disordered Bose-Hubbard model. For example, in systems like superfluid Helium in disordered media [57–62] or in thin films [88, 89], changes in conductivity have been modeled using the disordered Bose-Hubbard model. Engineered systems like Josephson junction arrays [19, 90–92] and disordered ultra-cold atomic gases [4–6, 39, 44] can emulate the physics described by the disordered Bose-Hubbard model. In addition to being used to emulate condensed matter systems, the behavior ultra-cold systems in the presence of disorder is an important topic on its own. The solutions to this simple model that focus clearly on the important interplay between disorder and interaction may also be important in explaining other outstanding mysteries regarding granular superconductors [93] and supersolidity [17, 63, 64].

Interacting bosons localize into different insulating ground states depending on the strength and type of the disorder added to a lattice. Below a critical value of disorder, both the superfluid and Mott-insulator phases retain their essential characteristics: the superfluid is delocalized and the Mott insulator is localized and incompressible. When Giamarchi and Schulz [52, 53] studied one-dimensional, disordered, lattice bosons using a renormalization group method, they found, for sufficiently strong disorder, bosons localized to a disordered insulating phase — the Bose glass, as shown in Figure 2.6. Particles in a Bose glass are are localized as in a Mott insulator, but there is no gap for particle-hole excitations, and thus the gas is compressible. This initial work using renormalization group techniques revealed neither the phase diagram nor the microscopic nature of the Bose glass.

Many different techniques have been used since the original study of by Giamarchi and Shulz to study disordered bosons. These include generalizations of the Bogoliubov and Baliev theories [94–96], mean-field theories [20, 70, 75, 76, 78, 97–99], field-theoretic calculations [20, 100–104], renormalization group theory — the one-dimensional solution [22] as well as Refs. [52, 105–107], quantum Monte-Carlo simulations [21, 23, 108–117], strong-coupling expansions [118, 119], and direct numerical diagonalization [120].

Among this research, there is consensus on the existence of the superfluid, Mott-insulator, and Bose-glass phases when disorder is present. However, quantitative predictions for the phase boundaries are diverse. Additionally, disorder can have many different probability distributions which contain different types of spatial correlations; the impact of these cor-

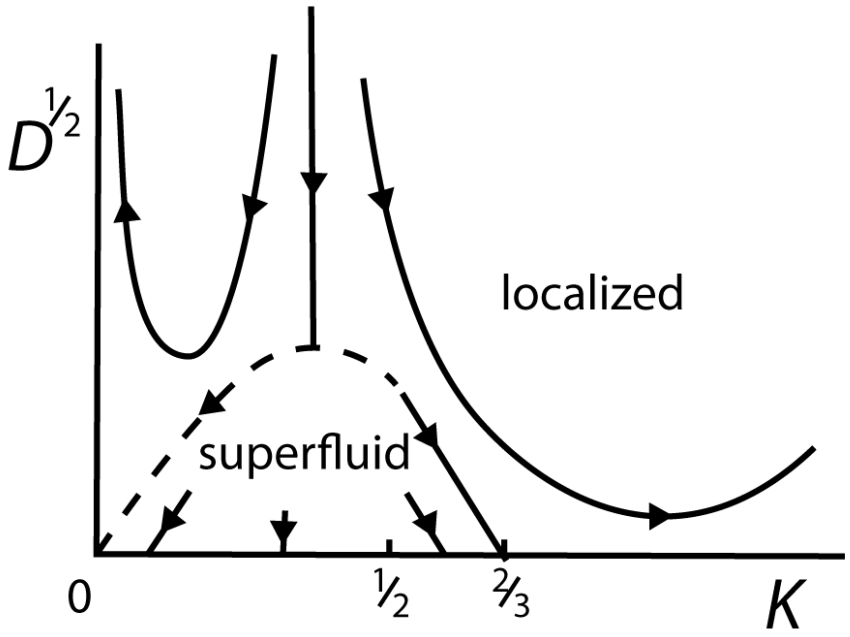

Figure 2.6 Renormalization group flow reproduced from Ref. [52] showing the existence of a superfluid and two insulators for one-dimensional interacting bosons with disorder. The vertical axis, $D^{1/2}$, is inversely proportional to correlation length; the horizontal axis, K, is proportional to disorder strength. The arrows indicate the direction of successively larger course-graining. The dashed line indicates a region where the method is inconclusive. Above the disorder value $K = 2/3$ the state is always a Bose glass.

relations on the phase diagram is not fully understood. We will show in this section how the optical speckle in our experiment causes disorder in all of the Bose-Hubbard parameters. The microscopic nature of the disorder is important as there can be major qualitative differences in the phase diagram when correlations are present [23, 121].

2.3.1 Phase Diagram

This section will describe what is known about the qualitative features of the disordered Bose-Hubbard phase diagram in the thermodynamic limit, highlighting the areas where there is consensus as well as controversial features. There are five different features I will discuss: the Mott-insulator-to-Bose-glass transition, the superfluid-to-Bose-glass transition, Anderson localization in the non-interacting limit, controversy over a direct superfluid-to-Mott-insulator transition when disorder is present, and the existence of a re-entrant superfluid.

There is consensus among theorists that, in the limit that $t \ll U$, sufficiently strong disorder will destroy the Mott insulator (even if bounded, i.e., there is a finite range for the disordered Bose-Hubbard parameters). For $\Delta < U/2$, increasing disorder decreases the gap [110], eliminating it completely when $\Delta = U/2$ [20, 23, 99, 104, 108, 118]. For any point on the phase diagram that is an insulator at $\Delta = 0$, when disorder with a bound larger than $\Delta = U/2$ is present, there must always exist a region of arbitrarily large size where the chemical potential is high or low enough for a superfluid to exist [23]. A superfluid embedded in a Mott insulator creates a density of states at infinitesimal excitation energies, destroying the gap and forming a Bose glass.

There is also consistent agreement that the superfluid is destroyed when the disorder is too strong to be screened by interactions (see Section 2.3.3) and a critical fraction of sites become localized [20, 23]. For particles to be completely delocalized there must be linked superfluid regions across the entire sample; when two regions arbitrarily far apart become linked by superfluid sites, there is a percolation transition. In three dimensions, this leads to a robust superfluid that persists at finite temperature and high disorder [23, 44].

In the limit that $U \to 0$, at least a fraction of the gas becomes an insulator at any disorder via Anderson localization [122, 123]. Anderson localization is a single particle effect that occurs in both bosons and fermions. The existence of a mobility edge in 3D causes the localized Anderson glass to be destroyed when finite momentum states are populated either through interactions or finite temperature [124, 125].

When the Mott insulator is destroyed by disorder it can either become a superfluid or a Bose glass. There is disagreement over whether the gas can ever have a direct transition (in t/U) from a Mott insulator to a superfluid in the presence of disorder without an intervening Bose glass (see Figure 2.7). Groups have predicted such a direct transition [21, 96, 100, 103, 113–115, 117], even quite recently [18, 99]. However, other groups have claimed that no direct transition is possible [119], and recently Pollet et al. claim to prove the absence of

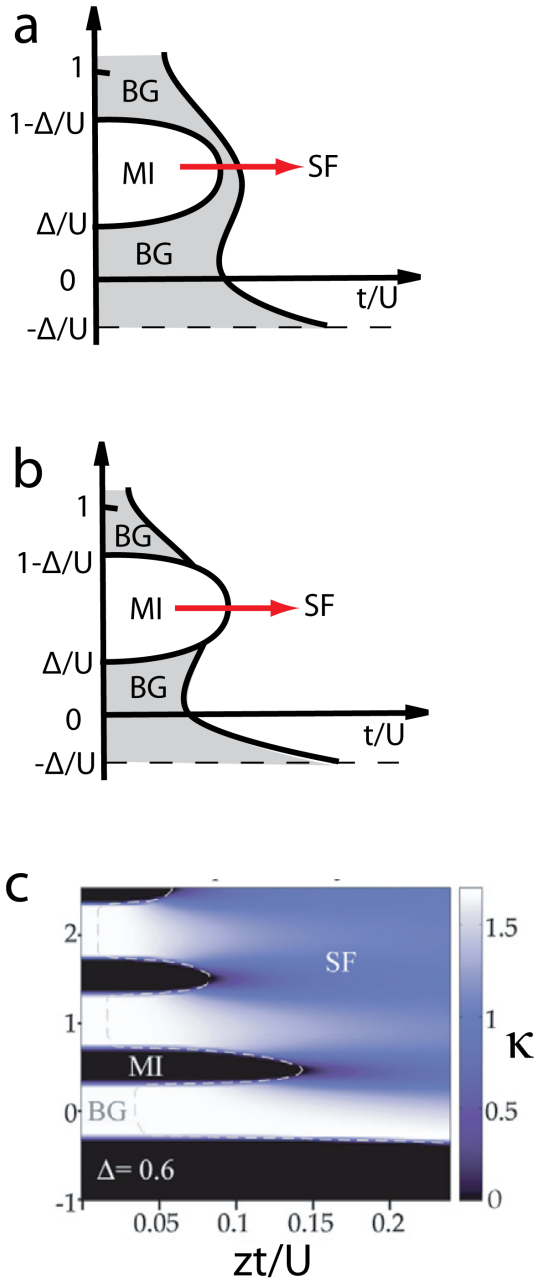

Figure 2.7 Differing phase diagrams for the disordered Bose-Hubbard model. Ref. [20] predicted a Bose glass (**a**), but left open the possibility of a direct SF/MI transition — with no intervening Bose glass — in the presence of disorder (**b**). The red arrows indicate the MI to SF transition at unit filling for an indirect transition (**a**) and a direct transition (**b**). (**c**) is reproduced from Ref. [99], which predicts a direct superfluid to MI transition using a stochastic mean-field theory. The color scale in **c** indicates the compressibility κ which distinguishes the MI from the BG and SF.

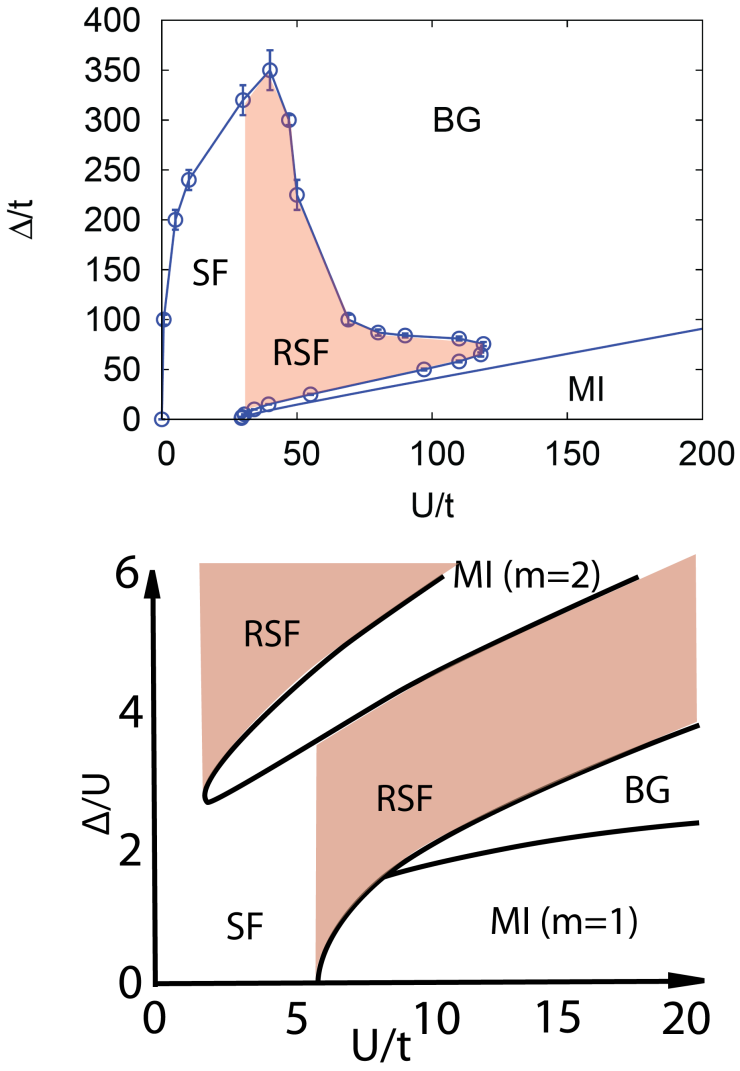

Figure 2.8 (Top) QMC phase diagram for a disordered Bose-Hubbard system at $T = 0$ and unit filling with random disorder in ϵ reproduced from Ref. [23]. The quantum Monte-Carlo calculation of the phase diagram predicts a re-entrant superfluid (RSF) (indicated by red shading) phase at $T = 0$, while excluding the possibility of a direct SF-to-MI transition with finite disorder [65]. (Bottom) Ref. [18] predicts a RSF, a disorder induced MI, and a direct SF-to-MI transition using the replica trick at small finite temperatures. The two different MI lobes have two different fillings m.

a direct transition conclusively [65]. Figure 2.7 shows phase diagrams representative of the different predictions. Because arguments against a direct transition rely on the existence of rare regions, finite-size ultracold-atom experiments may not be able to easily prove or disprove these conjectures [23].

Finally we will consider the case when an insulator becomes a superfluid when disorder is added — the re-entrant superfluid. This phase was predicted to exist by Rapsch et al. [22] and confirmed in the recent QMC of Gurarie et al. [23] and others [18, 99]. No critical temperature bounds were predicted for the re-entrant superfluid "finger" (seen in Figure 2.8). A simple model by Zhou and Das Sarma [126] predicts that the re-entrant superfluid may have a much lower critical temperature than the superfluid without disorder. This may make it difficult to observe the re-entrant superfluidity experimentally.

2.3.2 Understanding the Phase Diagram

Even without an exact solution to the phase diagram, the features highlighted in the last section can be understood qualitatively using toy models. Examining simple models can provide intuition into otherwise counter-intuitive theoretical predictions, and help us understand the microscopic behaviors that drive the many-body phases. The toy models will be discussed in terms of three phenomena:

- disorder changes a superfluid to a Bose glass,
- disorder changes a Mott insulator to a Bose glass,
- disorder changes a Bose glass into a superfluid.

The mechanism that changes a superfluid to a Bose glass can be understood in terms of microscopic puddles of superfluid alongside regions of insulator [23, 97]. When disorder localizes atoms on some fraction of sites, randomly across the lattice, a superfluid may still survive if the remaining superfluid sites are connected. If disorder in a region is sufficiently weak, the region will remain superfluid. Alternatively, when the disorder becomes too strong, the state localizes and destroys the superfluid. As long as there exists a connected path of superfluid sites, an atom can be delocalized across its entire length.

This transition is modeled by percolation theory [23, 127]. When the probability for any region to remain superfluid, P, is near unity, only rare regions will be in the localized state, and the superfluid regions will remain connected. When the probability of being in a superfluid state is near zero, rare regions of weakly delocalized particles will exist in small puddles not connected to each other. As shown in Figure 3.20, a percolation transition occurs when there exists a set of superfluid puddles that connect and grow to infinite size. For a 3D cubic lattice, this occurs when $P = 0.31$. On the other hand, for a 1D lattice, the percolation transition takes place at $P = 1$ (i.e., infinitesimal Δ) since any localized site will keep points on either side disconnected.

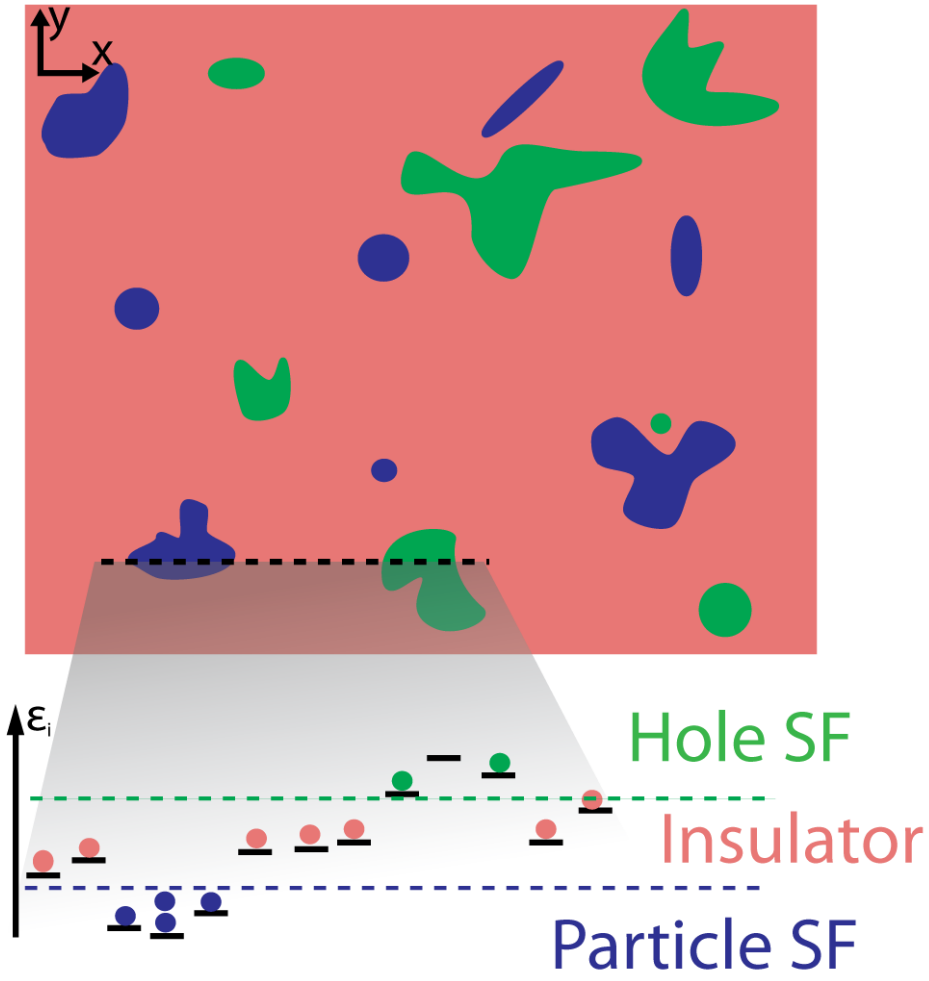

Figure 2.9 This illustration adapted from Weichman et al. [104] shows puddles of superfluid particle (blue) and hole (green) excitations in a Mott insulator (pink). When the $\mu < \mu_h$, where the gas is locally at a chemical potential below the MI lobe, holes in the Mott insulator condense and form a superfluid. Alternatively when $\mu > \mu_p$, where the gas is locally at a chemical potential above the MI lobe, a superfluid of particles forms. When many connected sites become SF a puddle forms. These puddles change an incompressible Mott insulator into a compressible Bose glass. Because the superfluid cannot move from one side of the sample to the other, the state remains insulator. In the percolation transition described by Gurarie et al. [23] (giving $\Delta_c/U = 10$), a superfluid with $\langle n \rangle = 1$ undergoes a transition to a Bose glass when an $n = 0$ insulator breaks the superfluid into puddles.

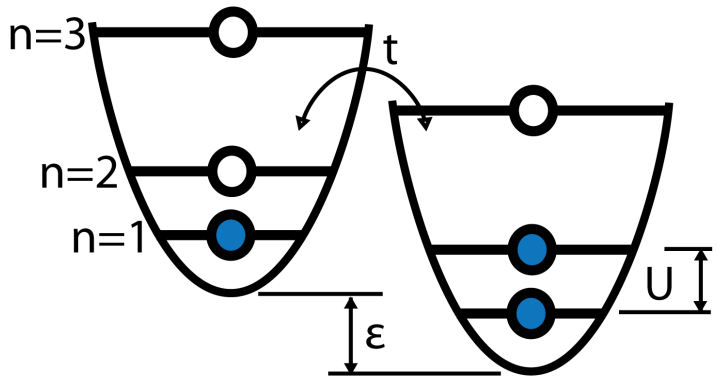

Figure 2.10 Two adjacent wells minimize their energy by localizing when the interaction energy is sufficiently strong. When the disorder in ϵ causes the on-site energies to be different by an amount near the interaction energy U, the atoms (represented by filled blue circles) can lower their energy by delocalizing across the two sites. Rare regions where disorder creates many nearby sites with delocalized atoms can support a superfluid.

For a percolation transition in the disordered Bose-Hubbard model, the probability P of a site being localized is proportional to $\sqrt{\Delta/U}$ for unit average filling (as shown in Section 2.3.4 and Ref. [23]). Equating this to the percolation threshold of $P = 0.31$ gives a critical disorder of $\Delta \sim 10U$ for the superfluid-to-Bose-glass transition. This value matches the QMC calculation reported by Gurarie et al. closely [23], and may explain their numerical results.

Weichman et al. [104] describe how disorder creates delocalized puddles of particles or holes, turning a Mott insulator into a Bose glass. In a clean Mott insulator, the Mott gap prevents a particle from tunneling to a neighboring site. When disorder changes the energy between neighboring sites by U, the energy cost to move to a neighboring site must vanish, as shown in Figure 2.10. If the disorder is slowly varying, the difference in energy between nearest neighbors may never be U. However, the Mott insulator still becomes superfluid because disorder changes ϵ sufficiently so the region has an incommensurate filling which produces a superfluid.

From this toy model we can see why infinitesimal amounts of disorder will always produce a Bose glass separating the Mott insulator from the superfluid everywhere but the tip of the Mott-insulator lobe. For a Mott insulator near the superfluid transition, a small amount of disorder will produce rare regions that become superfluid. If a Mott insulator has any superfluid regions inside it, it is compressible, i.e., it is a Bose glass.

The most surprising prediction of the disordered Bose-Hubbard phase diagram is the existence of a re-entrant superfluid phase. The re-entrant phase emerges from a Bose glass by increasing either the interaction energy or the disorder strength. The behavior is non-monotonic in the sense that increasing the interaction energy or disorder further will return the state to a Bose glass. A recent paper by Zhou and Das Sarma [126] provides a simple

system that exhibits the re-entrant behavior. This toy model gives an intuitive explanation that helps explain the predictions made in the more complicated disordered Bose-Hubbard model.

Zhou and Das Sarma approximate a disordered lattice with just two sites. The Hamiltonian is analogous to the Bose-Hubbard Hamiltonian,

$$H = -t(b_L^\dagger b_R + c.c.) + \frac{U}{2}\sum_\sigma n_\sigma(n_\sigma - 1) + \frac{\epsilon}{2}(n_R - n_L), \tag{2.26}$$

where b_L and b_R are the annihilation operators for the left and right wells respectively, $\sigma = \{L, R\}$, and n_L and n_R are the number operators. The parameters t, U, and ϵ can varied and quantities like the coherence, $C = \langle b_L b_R \rangle / N$, can be analytically calculated. Disorder is simulated by averaging over a distribution of different energy differences, $P(\epsilon)$. The disorder-averaged coherence is then,

$$\bar{C} = \int d\epsilon P(\epsilon) C_\epsilon \tag{2.27}$$

which is analogous to the superfluid fraction in a lattice.

As shown in Figure 2.11, for this simple double-well model, the coherence value is increased for small amounts of disorder before it drops again, similar to the re-entrant superfluid "finger" in the QMC calculation of Gurarie et al. [23]. The mechanism is similar to the one that creates a Bose glass: disorder creates nearby sites that have a difference in energy of about U, allowing atoms to delocalize through resonant tunneling (see Figure 2.10). If sufficiently many sites become delocalized, a superfluid can percolate across the entire lattice. The re-entrant coherence created in this model is destroyed at very low temperatures, (i.e., less than 1 nK), suggesting that current experiments at finite temperature may not be able to observe re-entrant superfluid.

2.3.3 Anderson Localization and Screening

Up to this point, we have considered strongly interacting particles. Starting from the non-interacting Anderson localization limit of $U = 0$, we will go on to examine how screening delocalizes particles when interactions are added. Anderson localization is a single particle effect which is observed in many disordered systems from condensed matter to photonic waveguides [128, 129]. As such, it is a pathological effect of the Bose-Hubbard model as $U \to 0$. The description of Anderson localization in the following section will distinguish the work in this thesis from other recent experiments with disordered optical lattices that do not explore the strongly interacting limit.

If delocalized non-interacting particles are imagined as propagating waves, Anderson localization occurs when these waves are reflected with random amplitude or phase from barriers or scatterers [124]. Even for disorder strengths small compared to the kinetic energy of the particles, interference effects between the scattered waves cause the particles

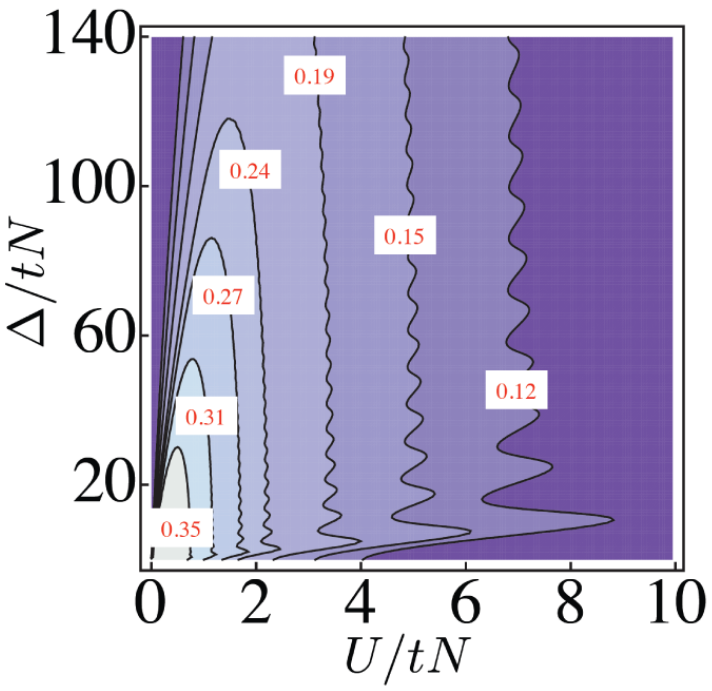

Figure 2.11 Contours of constant disorder averaged coherence C (red numbers) phase diagram for N particles in a double well (reproduced from Ref. [126]) at $T = 0$. Δ is the disorder strength, U is the interaction energy, t is the tunneling energy between wells, and N is the number of particles. For small disorder values, increasing disorder increases C. The increase in coherence resembles the "superfluid finger" in Figure 2.8

.

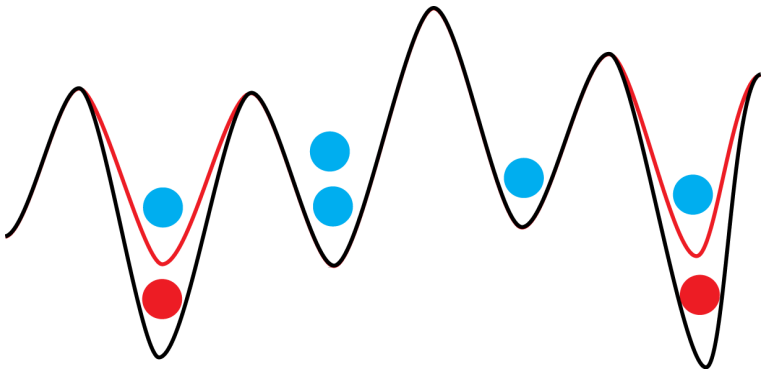

Figure 2.12 A schematic of localized atoms (red) screening a disordered potential (black line) allowing delocalized atoms (blue) to see a smooth, modified potential (red line). A site with a localized atom has a potential energy higher by U.

to localize. In one and two dimensions, all states are localized for infinitesimal disorder, although as the kinetic energy of the particle increases, the localization length also increases. For particles in three dimensions there exists a transition between localized and delocalized states at a kinetic energy called the mobility edge.

In the experiments described in this thesis, we are unable to study Anderson localization because interactions are always present in our lattice. Anderson localization was successfully realized by other groups in one dimension alternatively by using a Feshbach resonance [14], or by reducing density via ballistic expansion to suppress the effects of interactions [13].

When the on-site interaction energy is increased and becomes comparable to the disorder energy, Anderson localization will be suppressed by screening [94, 130]. Screening can be understood by imagining a disordered lattice with successively greater number of atoms added to it. When there is only one atom in a system, the interaction energy is zero and the particle will become localized. The next atom in the system will experience a modified effective potential from the repulsive interaction from the first, localized atom. This effective potential will make it less energetically favorable to exist in the same region as the first localized atom. If the disorder is sufficiently strong compared to the interaction energy, the atom will stay localized in the same region, if not it will move to another region. As more atoms per unit volume are added to the system, all regions will eventually contain enough localized atoms to completely screen the disorder with repulsive interactions. After all regions are saturated with localized screening atoms, additional atoms will see a smooth potential, and will Bose condense — becoming superfluid. This is shown in Figure 3.3.3, where the localized atoms in red screen the disorder experienced by the delocalized atoms in blue.

Alternatively, as emphasized by Lee and Gunn [94, 130], the condensate is described as healing itself over a length scale $\lambda_H = \sqrt{\frac{2td^2}{\bar{n}U}}$ where d is the lattice spacing, and $\bar{n}$ is the average density. In the non-interacting limit, the healing length becomes too long to screen disorder and atoms are scattered from the condensate. Experiments have observed

localization in the weakly interacting regime where the disorder size is larger than the healing length [1–4, 7]

2.3.4 Disorder Correlation

The theoretical predictions of the disordered Bose-Hubbard model described so far make various assumptions about the nature of the disorder. For instance, the distribution of the on-site energies ϵ, can be either bounded or decay exponentially. Some qualitative features, like the absence of direct Mott-insulator-to-superfluid transition when $\Delta \neq 0$, do not change for any random bounded disorder [23], but the position of phase transition can change based on the specific disorder realization in some calculations [22]. We can see in the example of Anderson localization that disorder correlations are important. The position of the mobility edge in a three-dimensional Anderson-localized gas is dependent on the disorder distribution [123, 124]. In the case of a quasiperiodic, lattice a mobility edge at finite disorder can exist in one dimension rather than in three dimensions necessary for uncorrelated disorder [14]. If correlation in disorder have important effects for Anderson localization, we should be careful to take into account their effects when studying strongly interacting systems, as in the disordered Bose-Hubbard model.

To see how correlations between disorder in ϵ can change the qualitative features of the disordered Bose-Hubbard phase diagram, we consider the difference between two different disordered systems. Figure 2.14 compares the phase diagrams for random disorder vs. a bichromatic lattice with two incommensurate wavelengths. The two phase diagrams show qualitatively different features — in particular, there is never an intervening Bose glass between the Mott insulator and superfluid in a bichromatic lattice.

To understand how these two distributions differ, consider Figure 2.13 which compares the nearest-neighbor joint probability distribution of ϵ for quasidisorder and random disorder. This plot supposes that there is a lattice with depth $s = 5\ E_R$. If we looked a random site in this lattice with $\epsilon_i = 1\ E_R$, we can measure the probability distribution of the disorder ϵ_{i+1} at its neighbor, i.e., the joint probability distribution. This joint probability function $P(\epsilon_i|\epsilon_{i+1})$ is the probability that: for two neighboring sites in a lattice, if site i has disorder $\epsilon_i = x$, then $P(x|y)$ is the probability that site $i+1$ has disorder $\epsilon_{i+1} = y$. If the sites are uncorrelated (grey line), then the probability $P(x|y)$ is equal to the single site probability of having $\epsilon_{i+1} = y$ (see Eq. 1.6). However, the more correlated neighboring sites are, the more closely $P(x|\epsilon_{i+1})$ will resemble a Kronecker δ function at x. In Figure 2.13 we compare the fine-grain speckle in our experiment (green line) to three other types of distributions. Our speckle is most similar to the fully uncorrelated speckle and clearly distinct from the coarse ($\sigma = 5\ \mu$m) speckle (similar to the experiment in Ref. [4]) which appears as a sharp peak around the value of ϵ_i ($1\ E_R$). Because an incommensurate bichromatic lattice (red line) has fully determined values for neighboring sites, there are only two possible values its neighbors could have, shown by the two δ functions — which show the

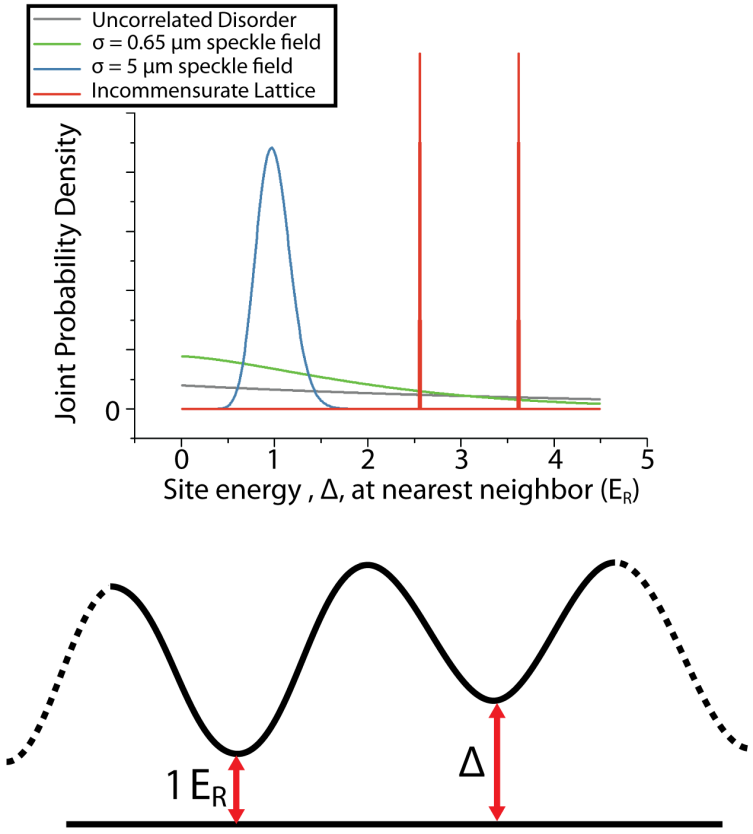

Figure 2.13 This plot shows the joint probability $P(\epsilon_i|\epsilon_{i+1})$ distribution of nearest neighbor site energies for disorder with 5 E_R average disorder strength when a site has exactly $\epsilon_i = 1\ E_R$ of disorder and its neighbor has $\epsilon_{i+1} = \Delta$ of disorder. σ is the width of the autocorrelation function. For disorder with large σ, nearby sites have nearly the same energy, thus a tight distribution around 1 E_R. For fine-grain disorder (i.e., small σ), nearby sites are almost completely uncorrelated, and a large range of disorder strengths may exist nearby, similar to the case of completely uncorrelated disorder. For "quasidisorder" formed by an incommensurate lattice, nearby energies are completely correlated, and can only have two values. The lower schematic shows the lattice with sites i and $i+1$. The value of disorder at site i is fixed at 1 E_R. The distribution of Δ at site $i+1$ is given by the joint probability distribution in the top graph.

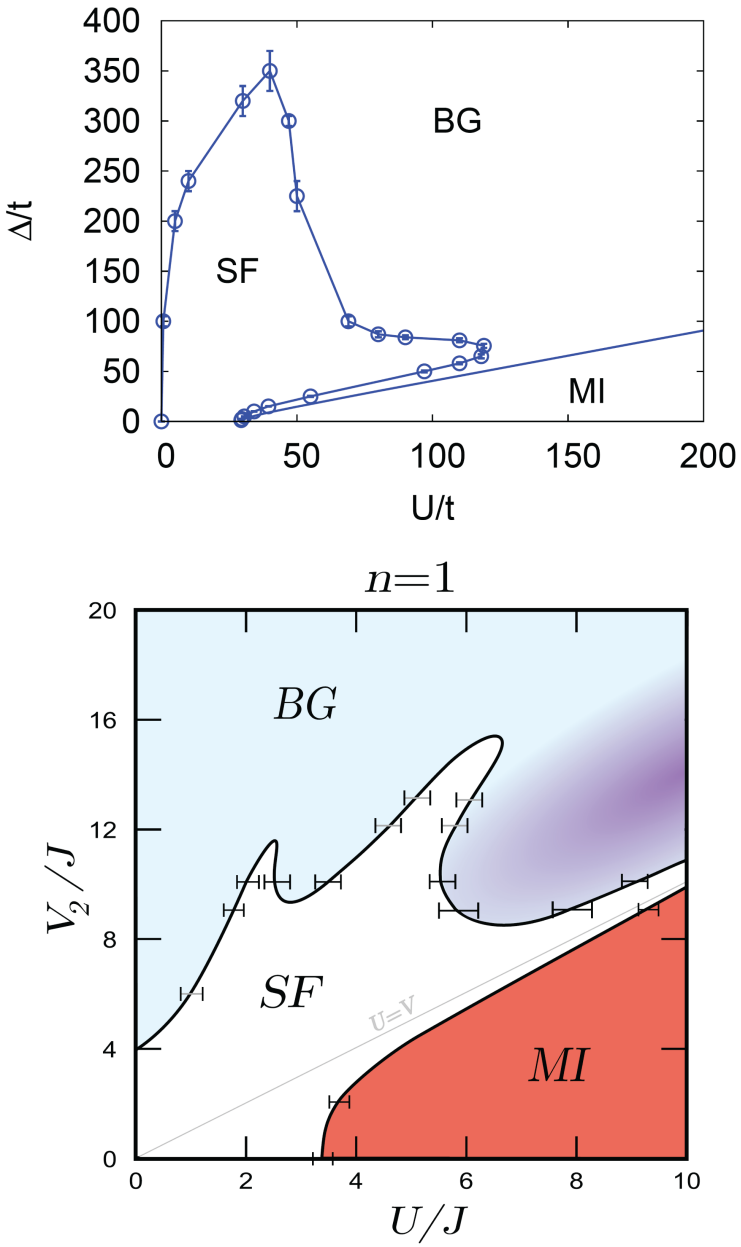

Figure 2.14 Top: phase diagram for $T = 0$ unit filling in a lattice with random disorder reproduced from Ref. [23]. Bottom: reproduced from Ref. [121], the zero-temperature phase diagram for bosons in an incommensurate bichromatic lattice (here, a second lattice of depth V_2 is added to a lattice with Hubbard parameters U and t (often labeled J)). In the quasiperiodic lattice phase diagram (bottom), as opposed to the random disorder (top), there is no intervening Bose-glass phase between the Mott insulator and superfluid phases.

perfect correlation between adjacent sites in a bichromatic lattice.

Another way to understand the importance of the difference between random disorder and quasiperiodic lattices is to look at the momentum distributions after the disordered lattice is snapped off. The bichromatic lattices will produce additional peaks corresponding to the additional lattice wavelength [12] (see Figure 2.15) which are not present for a lattice with random disorder. This clearly shows how correlations within a disordered lattice can have a large effect on observables.

The strong differences between the random and quasirandom distributions in Figure 2.13 may help explain differences in the respective phase diagram produced by the two methods as shown in Figure 2.14. In lattices with uncorrelated disorder, there is always a Bose glass when disorder is present between the superfluid phase and the Mott insulator (with the exception of the "tip" of the Mott lobe, possibly). This matches the intuition gained from the toy model in Section 2.3.2, and was expected from the earliest studies of the disordered Bose-Hubbard phase diagram [20]. In a recent calculation of the phase diagram for a quasiperiodic lattice (Figure 2.14) there is no Bose-glass phase between the superfluid and Mott insulator. Clearly the difference arises from the greater degree of correlation in the quasidisordered state; an intervening Bose glass in at least some region of the Mott insulator is a generic feature of all theories including random disorder in the thermodynamic limit. As shown in Figure 2.13 our fine-grain disorder is very similar to white-noise, uncorrelated disorder. This is in contrast to quasidisorder which has strong correlations between sites due to the periodic bichromatic lattice that creates the quasidisorder.

The influence of increased correlations on the quasiperiodic-lattice phase diagram may come from the absence of rare regions that have consistent values of disorder. A Bose glass forms when rare regions can form superfluid puddles. In a bichromatic lattice the correlations prevent these rare regions from occurring. To see this, consider a bichromatic lattice with perturbing lattice of intensity Δ and wavelength λ_2. There exists in this quasiperiodic lattice a site within E_s of the minimum possible energy. If the following criteria are satisfied:

$$|\lambda_1 - \lambda_2| > \lambda_2 \cos^{-1}(E_s/\Delta) \text{ and} \tag{2.28}$$

$$\lambda_1 > \lambda_2 \cos^{-1}(E_s/\Delta), \tag{2.29}$$

there exists no neighboring sites within E_s of the minimum possible energy. Randomly disordered lattices have a finite chance that such rare, nearby sites will exist. This absence of rare regions is another example of the differences in the distribution of nearest neighbor sites can also be seen in Figure 2.13. Fine grain disorder closely matches the distribution of totally uncorrelated disorder, while quasidisorder exhibits sharp correlations between nearby sites.

The dependence of the qualitative features of the phase diagram on disorder correla-

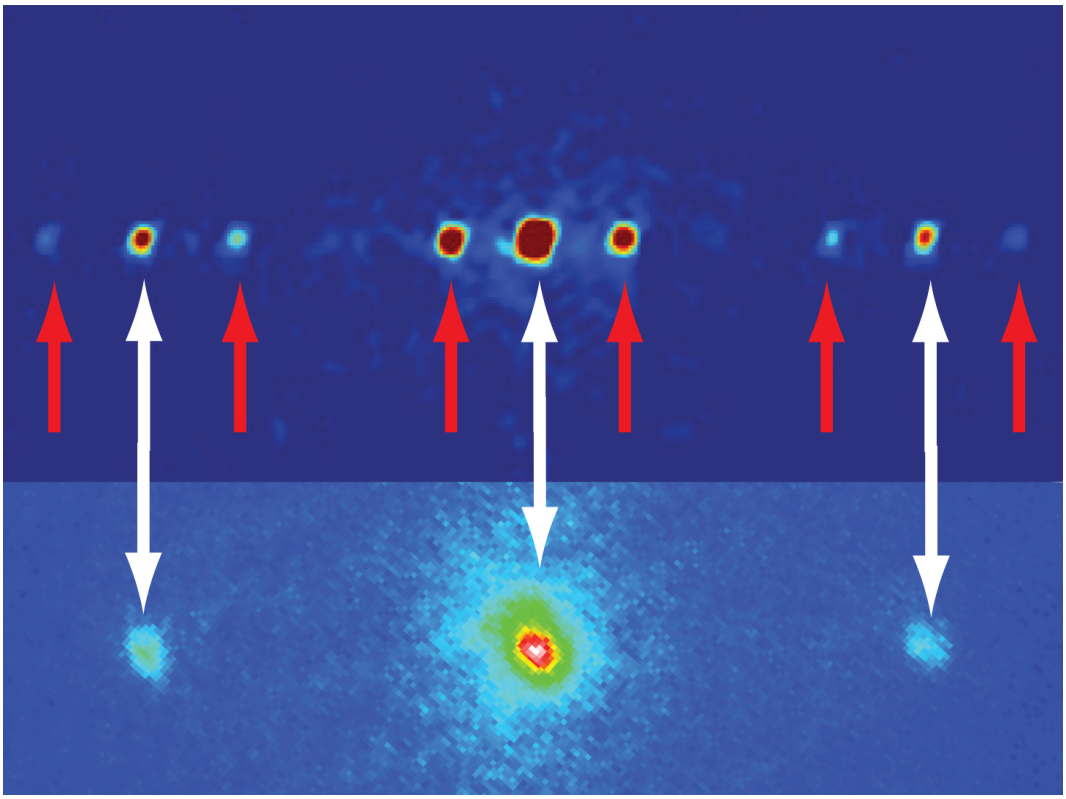

Figure 2.15 (Top) A TOF image of a gas of bosons released from an incommensurate bichromatic lattice after the lattice potential is turned off instantaneously (reproduced from Ref. [12]). The presence of two lattice wavelengths is demonstrated by the additional diffracted peaks (red arrows). In a lattice with random disorder, only the peaks indicated by the white arrows would be present. This is shown (bottom) for a 1D slice of a snap-off diffraction TOF image (from our experiment) for a $\Delta = 1\ E_R$, $s = 6\ E_R$ disordered lattice.

tions necessitates that we specify as precisely as possible the correlations that exist in our disordered lattice, described in Chapter 1. David Ceperley and his student Sheng Quan Zhou [39, 43] used the disordered optical lattice potential from our apparatus to produce the distribution of on-site energy, ϵ, as well as in t — so-called "off-diagonal" disorder — and U (see Figure 2.16). These parameters can be used to simulate the full optical potential with a simplified discrete lattice. The discrete lattice can be evaluated more efficiently using quantum-Monte-Carlo techniques [131, 132].

S.Q. Zhou and Ceperley [43] coarse-grain the real disordered potential from our experiment to a set of Bose-Hubbard parameters on discrete lattice sites. The relative size and anisotropy of the speckle field was preserved in these calculations, as was the orientation of the lattice to the long axis of the speckle. To produce disordered Bose-Hubbard parameters, first continuum wavefunctions are constructed that are simultaneously low energy and well localized to each site in the disordered lattice. Next, Bose-Hubbard parameters on each site are computed by the method in Equation 2.4. The coarse-grained lattice model and continuum models are ensured to have the same density and response to external perturbations by matching the density matrices at low energy.

The disordered Bose-Hubbard parameter distributions, shown in Figure 2.16, are determined by averaging over sites produced from many different disorder realizations. The on-site energies ϵ reflect the speckle field's negative exponential intensity distribution. There is little spread in the interaction energy U (relative to the mean value). The fine-grain nature of the speckle field produces large changes in the hopping energies t, that are exponentially dependent on the size of the barrier separating neighboring lattice sites. The hopping energy between nearest neighbors t_{ij} is correlated to the difference in site energies $|\epsilon_i - \epsilon_j|$, although it is not correlated to the overall change in site energy ϵ_i. This indicates that the off-diagonal disorder in our experiment is due to the fine-grain nature of our disorder.

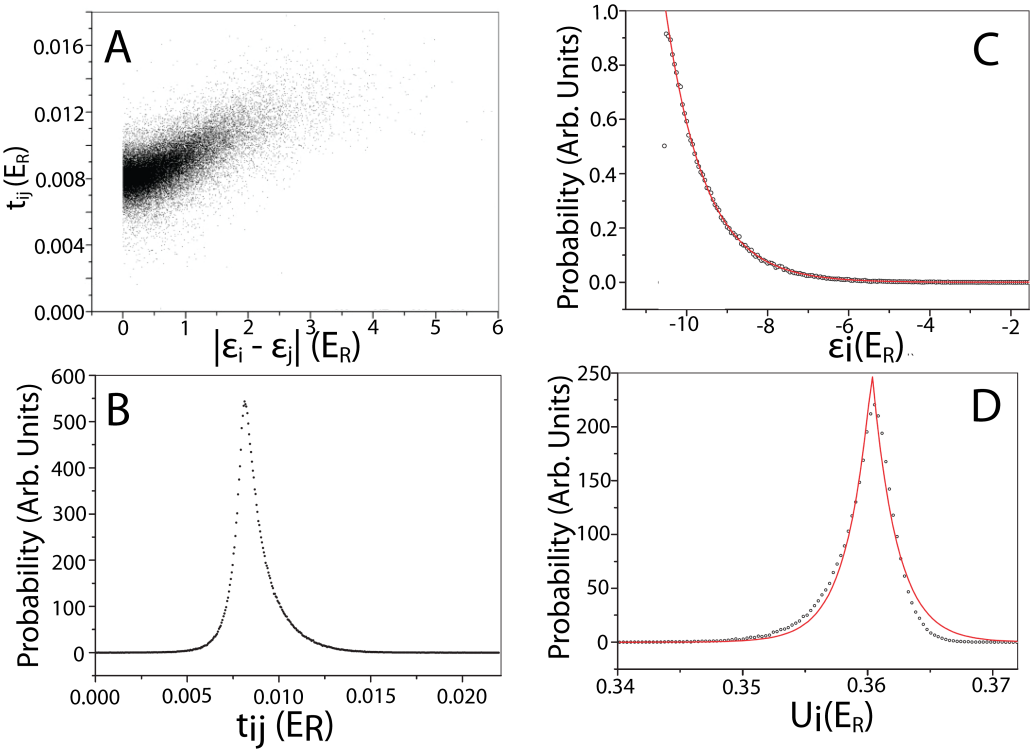

Figure 2.16 Zhou and Ceperley [43] constructed a localized, low-energy set of basis functions on a lattice matching the geometry and disorder in our experiments. Panel (**a**) is a scatter plot showing the correlation between on-site energy between neighboring sites, $|\epsilon_i - \epsilon_j|$, and nearest-neighbor hopping energy, t_{ij}. While both the on-site (**c**) and hopping (**b**) energies are shown to vary greatly with disorder, the on-site interaction energy(**d**) does not vary significantly. The fit in (**c**) is to an exponential; the fit in (**d**) is to a Laplace function.

Chapter 3

Disordered Bose-Hubbard Transport

3.1 Introduction

The topic of this chapter is measurements of transport in a disordered lattice. The primary result of this thesis is the discovery of an insulating state of bosonic atoms when disorder is added to an optical lattice. We found that this insulating state occurs when the condensate fraction vanishes; we will compare condensate fraction between the low-density gas in this work and a higher-density gas in our earlier experiments [39]. This set of measurements is an important step in resolving the phase diagram of the disordered Bose-Hubbard model described in Chapter 2. We will discuss how recent theoretical predictions [23] compare to our results.

Transport measurements allow us to directly probe changes in the superfluid-to-insulator transition and test theoretical predictions of its location on the phase diagram. To measure transport, we apply an impulse to the harmonically trapped gas of atoms in an optical lattice and measure the resulting velocity. Whether the velocity is zero or finite distinguishes between an entirely insulating gas and one with a finite superfluid-fraction. Adding disorder, we observed a change in the lattice depth s^* where the entire gas becomes insulating. The scale of disorder necessary to produce this insulating state matches a recent theoretical prediction [23]. We also observed that increased disorder strength leads to increased dissipation for all lattice depths we measured ($s = 6$–$19\ E_R$), contrary to theoretical predictions. Because finite temperature may explain this discrepancy, we have included bounds on the entropy per particle in our lattice. This was done using measurements of condensate fraction before loading into the lattice and after adiabatically turning off the lattice. These measurements of entropy before and after constrain the entropy of the gas in the lattice due to the second law of thermodynamics.

We found the transition from a superfluid to an insulator is correlated with condensate fraction vanishing. We measure condensate fraction by fitting images taken after time of flight (TOF) to a bimodal distribution. These measurements were taken in the low-filling limit of roughly one atom per site; in previous work with higher density, the condensate fraction never vanished [39]. This difference in behavior can be explained by the prediction that a disordered insulator will first appear at low filling [20]. We will discuss how interactions and screening of disorder may lead to the difference in condensate fraction between

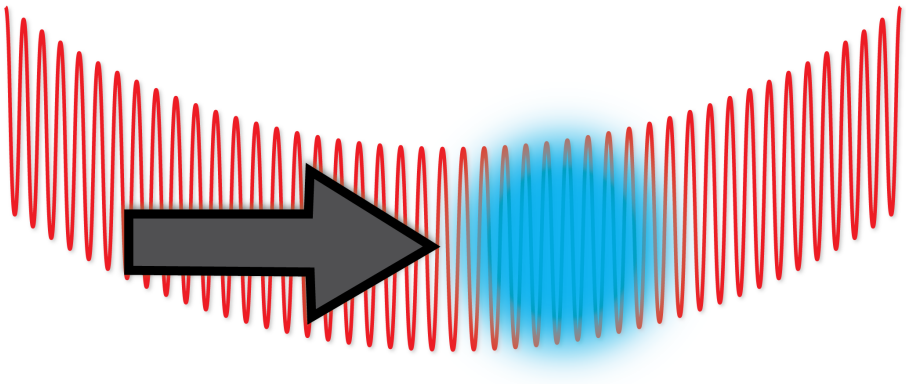

Figure 3.1 In this schematic picture, not to scale, a gas of neutral atoms (blue) in an optical lattice (red) undergoes damped harmonic motion after an impulse (grey arrow).

high and low fillings. Additionally, we address the effect of finite-temperature and heating on the insulator transition. We constrain the entropy per particle of our measurements, and show that the cessation of transport in the presence of disorder is not solely due to heating.

These measurements of transport are important because they constrain theories on the disordered Bose-Hubbard model. We are able to directly compare our experiment to theory because we determine the microscopic Bose-Hubbard parameters from our measured disordered lattice potential (see Chapter 2); this is difficult in experiments on solids. As previously mentioned, we only observe partial agreement with the most recent theory. While some of the discrepancy may be explained by finite temperature, another explanation is the difference between features of our disordered potential and the ones used in theory. For example, our trapped gas has an inhomogeneous density profile which is not included in the most recent numerical results. Also, our disordered lattice has an off-diagonal disorder component and intensity correlations not considered theoretically. These correlations affect transport — in certain regimes we observed anisotropic damping which reflected the anisotropy in the disorder intensity autocorrelation function. We will discuss the features of our disordered lattice potential that differ from an ideal, random disorder and how they may affect the results in this chapter.

3.2 Transport Measurements

We measure transport in a disordered lattice to test for the presence of an insulating state as we vary disorder strength Δ and lattice depth s. We characterize transport by measuring dissipation of the gas center-of-mass (COM) motion after a rapid impulse of length τ is applied, as shown in Figure 3.1. The damping rate γ for neutral bosons is equivalent to electrical resistivity in a solid. When resistance or damping becomes infinite, the gas is an insulator.

We have adapted this transport measurement technique from an earlier experiment in

our group led by David McKay [71]. In that work we studied transport of a gas of ^{87}Rb atoms in a "clean" lattice in the superfluid regime where quantum depletion is low. By measuring the damping rate as a function of temperature and lattice depth, we were able to show that the damping in the gas's COM motion was caused by phase slips. Phase slips are topological defects in a superfluid wave-function that allow energy to dissipate. These phase slips had previously been observed in superfluid ^{4}He by Richard Packard's group at Berkeley [133, 134] and likely affect thin superconducting wires [135, 136].

To find the transition between a conducting and insulating state, we use a measurement sensitive in the regime $\gamma \gg 1/\tau \gg \omega$, where ω is the frequency of the harmonic confining potential. Instead of measuring the motion as a function of time, we only measure the initial velocity v_i by measuring immediately after the impulse. When $\gamma \to \infty$, $v_i \to 0$. We identify the lattice depth above which $v_i = 0$ as s^*, the critical lattice depth at which the insulator transition occurs.

The main result of this thesis is the observation of a disordered insulator. For very high values of the lattice depth s, the gas is insulating even at $\Delta = 0\ E_R$ as it is a Mott-insulator. The critical value s^* for this transition becomes lower as the disorder strength Δ is increased. Where s^* decreases for finite disorder, a disordered insulator exists. For even the highest Δ we measure, the lattice remained non-insulating at low lattice depths — contrary to recent numerical calculations [23]. Nor did we observe a predicted insulator-to-superfluid transition (i.e., s^* increases for finite disorder) the so-called "re-entrant superfluid".

3.2.1 Transport measurements in optical lattices

Measurement of the damping γ of center-of-mass motion of neutral bosons in an optical lattice is directly analogous to measurements of electrical resistivity ρ_e in a solid. In the case of an electrically conducting solid, the force on the charge carriers is $F \propto -\rho_e v$, where v is the velocity of the charge carrier. The equivalent quantity to electrical current in a solid is mass-transport in an optical lattice where force is proportional to velocity, $F = -\gamma v$. The equivalence of γ and ρ_e is not coincidental — electrical resistance is essentially a measure of dissipation.

Dissipation in trapped atoms cannot be measured by the same techniques as the equivalent dissipation of electrons in solids. In solids, electrons can flow in through electrical leads and continue across the entire system. The atoms in an optical lattice must stay confined within the harmonic trapping potential, so damped harmonic motion must be measured as opposed to resistance. Since the atoms oscillate in the trap, the potential gradient cannot be left on during measurement as in a solid. Instead, an impulse is quickly applied without allowing the COM position to change significantly.

We use two different techniques to measure γ in the regimes $\gamma < \omega$ and $\gamma \gg 1/\tau \gg \omega$. When γ is small, we are able to fit a damped sinusoidal function to the data as shown in Figure 3.2. Although we could also fit damped motion for large γ, near an insulator

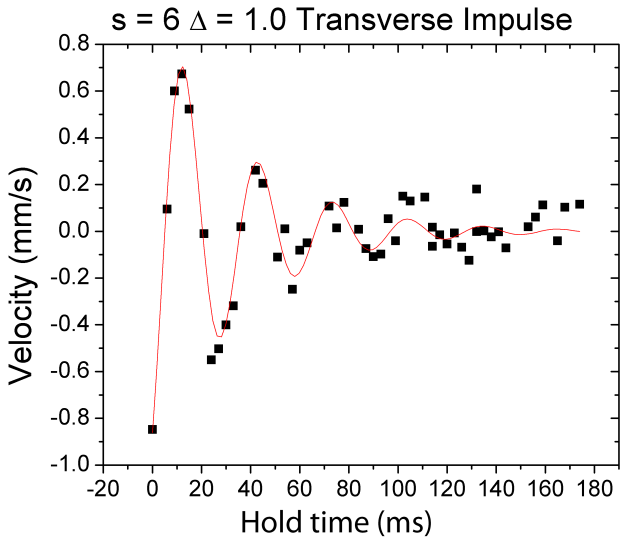

Figure 3.2 Velocity measured after TOF for atoms released from an $s = 6\ E_R$, $\Delta = 1.0\ E_R$ disordered lattice with $N = 7000$ atoms at $N_0/N > 0.9$. The COM motion of the atoms was allowed to evolve for a hold time after an impulse in the direction transverse to the disorder propagation direction. A damped sinusoidal function is used to fit the position of the atoms after a 20 ms TOF, which determines the damping rate γ.

transition we use a technique that requires much less data to measure changes in γ and $\gamma \to \infty$. Because $\gamma \gg 1/\tau$, the initial velocity v_o (directly after the impulse) becomes smaller as γ becomes larger. In the regime $\gamma \ll \omega$, the initial velocity will be proportional to the impulse, i.e., $v_i = \frac{F\tau}{m^*}$. However when γ is large ($\gamma \gg 1/\tau \gg \omega$) the COM oscillation will quickly reach its terminal velocity where $F/m = -\gamma v$, thus initial velocity after the impulse decays as $v_i = \frac{1}{\gamma\tau}\frac{F\tau}{m*}$. The dependence of v_i on γ allows a convenient way to measure the insulator transition; as $\gamma \to \infty$, $v_i \to 0$, and the entire lattice becomes an insulator.

We calculate velocity $v = D/t_{TOF}$ where D is the difference in the position of of the gas COM with and without an impulse after time-of-flight (TOF), and t_{TOF} is the elapsed between the release from trap and absorption imaging. As shown in Figure 3.3, even without an applied impulse, the position changes as the lattice depth and disorder are varied. This is due to small misalignments of the the lattice and disorder beams that change the equilibrium position of the atoms as the strength of the lattice or disorder increases. The curvature in the lattice and speckle potentials slightly changes the zero-velocity position of the COM after time of flight. The COM position without an applied impulse (green points) is fit linearly with respect to lattice depth to produce an offset which is subtracted from data with an impulse (black points) before calculating velocity.

To accurately measure the COM of the atomic gas after TOF, we use a two-component fit corresponding to the condensate and non-condensate components. The centers of these two functions are allowed to vary independently, producing different displacements, and thus

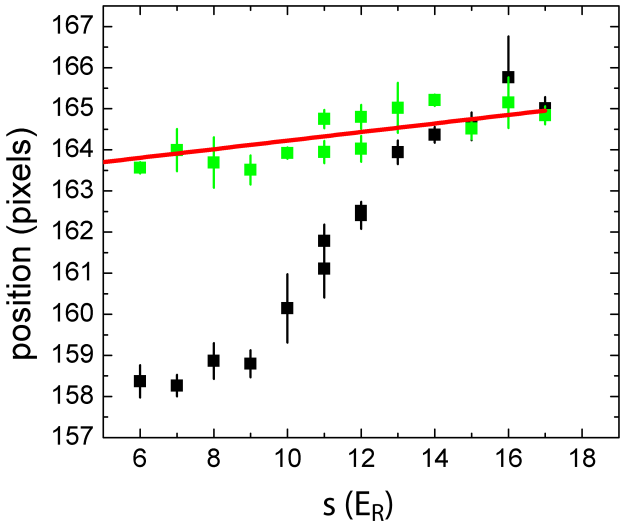

Figure 3.3 Plot of COM position with (black) and without an applied impulse (green). The linear fit to the COM without an impulse (red) is used to correct for shifts due to the lattice or disorder beam intensity. This data was taken with $\Delta = 3\ E_R$, N = 14000 at low temperature where the initial $N_0/N > 0.9$.

different velocities for each component. The total COM velocity of the gas is calculated by adding the velocities weighted for the numbers of atoms in each component. Figure 3.4 shows that the condensate fraction continues to move after the non-condensate fraction has stopped. Using the COM of the entire gas, rather than one component, allows a consistent measurement when the condensate becomes smaller than we can measure. In Section 3.3, we discuss how condensate fraction is correlated with transport measurements.

We apply an impulse to the atoms in two directions: longitudinally and transversely to the propagation direction of the speckle beam. As explained in Section 1.3.3, the speckle intensity autocorrelation length is longer in the longitudinal direction than in the transverse. To account for this difference, we probe transport in each of these directions separately. These impulses are produced by two different methods. To apply an impulse to the atoms in the longitudinal direction we displace the trap vertically for a short time by moving the confining 1064 nm optical dipole beam. To produce the transverse impulse, we quickly apply a magnetic field gradient. Figure 3.5 shows the relative directions of superfluid flow after the applied impulse relative to the anisotropic speckle intensity. Figure 3.6 shows schematically how the two different impulses move the atoms in orthogonal directions. It also shows the relative force as a function of time during the impulse.

To produce a force in the vertical direction, we move the optical dipole trap upward for 3 milliseconds. In a harmonic trap, a shift in the trap position is equivalent to a linear potential gradient. The force F produced by this shift in the trap potential $V(x)$ is

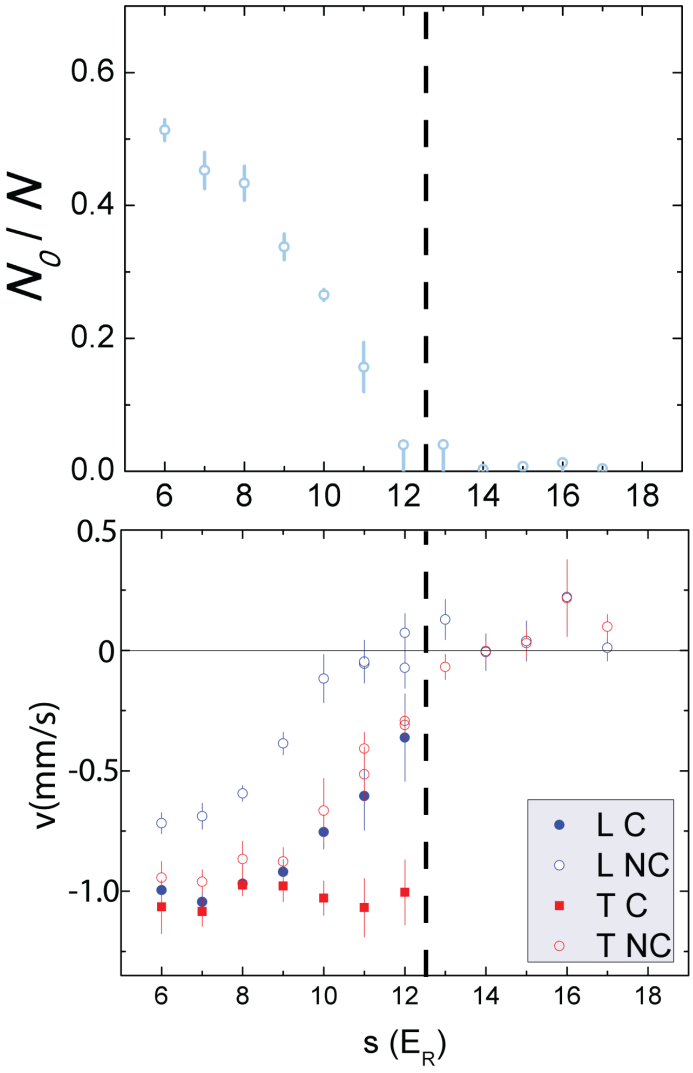

Figure 3.4 The condensate fraction N_0/N (top) and initial velocity versus lattice depth (bottom) for $\Delta = 3\ E_R$ in both longitudinal (L, blue) and transverse (T, red) directions with the measured velocities for condensate (labeled LC or TC) (closed points) and non-condensate (labeled LNC or TNC) (empty points). Center-of-mass velocity is a average of both condensate and non-condensate velocities weighted by condensate fraction. The error in condensate velocity becomes very high after $s = 12\ E_R$ because the condensate component is too small to fit (indicated by vertical dashed line); the condensate velocity for those points is not shown. The velocities of the condensates for longitudinal and transverse impulses differ after $s = 9\ E_R$, the longitudinal initial velocity decreasing, while the transverse remains unaffected.

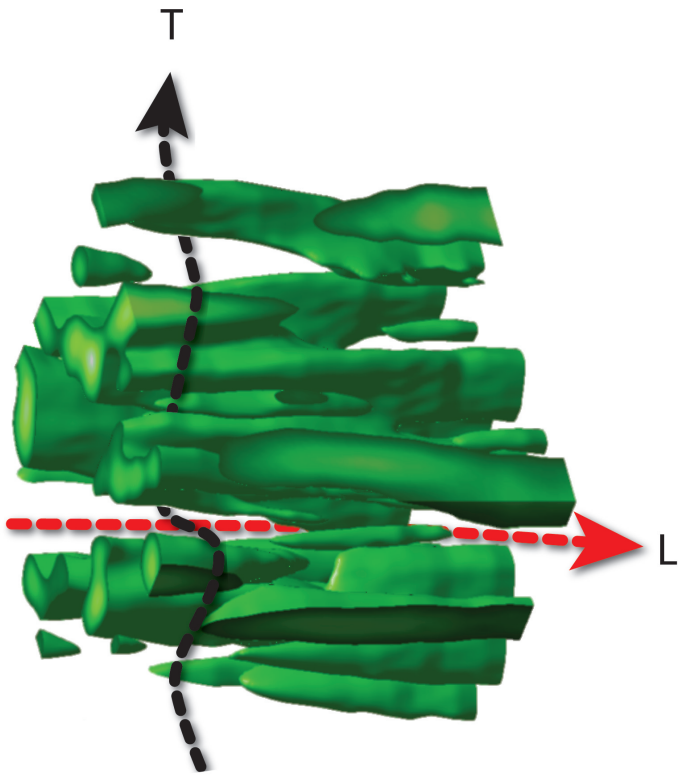

Figure 3.5 Isopotentials of a speckle potential measured with a microscope. Points with intensity below the mean are transparent, while points above are green. The impulse directions used in transport measurements are shown for the longitudinal (transverse) direction in red (black). For sufficient intensity, disorder may cause the regions of the lattice with high intensity speckle to become unoccupied [23]. Transport in the lattice could still occur by flowing around these unoccupied regions as indicated by the arrows.

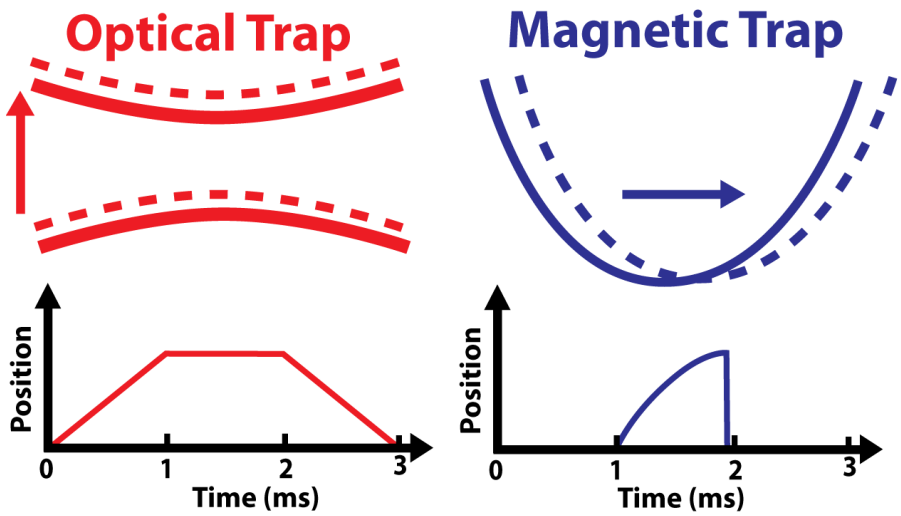

Figure 3.6 A schematic demonstrating how impulses are produced in the longitudinal (red) and transverse direction (blue). In the longitudinal direction, an impulse is produced by moving the optical dipole trap confining the atoms in the vertical direction. The plot below it shows the position as a function of time. The position in varied to produce the desired velocity after an impulse. The magnetic trap is displaced horizontally by applying an additional magnetic gradient. The position as a function of time is asymmetric due to the finite time it takes for the magnetic coil current to turn on. The velocity after the applied impulse is adjusted to achieve a velocity of 1 mm/s by varying the total time the magnetic field is on between 0.96 ms and 0.99 ms.

determined according to

$$V(x+d) = V(x) - Fx + E \tag{3.1}$$
$$= -1/2m\omega^2(x+d)^2 \tag{3.2}$$
$$= -1/2m\omega^2x^2 - m\omega^2xd - 1/2m\omega^2d)^2, \tag{3.3}$$

and therefore

$$F = m\omega^2 d, \tag{3.4}$$

where m is the mass of ^{87}Rb, d is the trap displacement, ω is the frequency of the potential created by the optical dipole beam, and E is an energy offset.

The optics used to produce the dipole trap allow a simple means to change its position. The beam for the dipole trap goes through an acousto-optical modulator (AOM) and then a lens where it is focused onto the atoms. Because the beam is parallel at the AOM and focused at the atoms, the two planes are Fourier conjugate. An angular deviation at the AOM plane will cause a shift in position of the dipole trap d at the focus.

$$d = f\Theta \tag{3.5}$$

where f is the focal length of the lens and Θ is the angular deviation caused by the AOM

$$\Theta = \frac{\lambda}{\Lambda} \tag{3.6}$$

($\Lambda = v_s/\nu$ is the wavelength of the acoustic wave inside the AOM, λ is the wavelength of light, v_s is the speed of sound in the AOM, and ν is the RF driving frequency). For the optics in our experiment, a 115 kHz change in AOM frequency will produce a 5 μm change in the trap position. This, in turn, will produce a velocity in the the bare harmonic trap of 1 mm/s when applied for 2 ms in a harmonic trap with frequency $\omega_z = 2\pi \cdot 50$Hz. We shape the impulse by ramping the dipole beam from its initial position to the final position d in 1 ms — hold for 1 ms — and then ramp back linearly in 1 ms.

To produce an impulse in the transverse direction (perpendicular to gravity), we apply a magnetic field gradient. The low-field-seeking $|F = 1, m_F = -1\rangle$ atoms feel a potential,

$$V_i(x) = m_F g_F \mu_B |B(x)|, \tag{3.7}$$

and thus the force is

$$F_x = -m_F g_F \mu_B \frac{d|B(x)|}{dx}, \tag{3.8}$$

where m_F is the Zeeman level, $g_F = -1/2$ is the g-factor for the $F = 1$ hyperfine manifold, μ_B is the Bohr magneton, B is the magnetic field, $V_i(x)$ is the potential energy, and F_x is the force from the magnetic field gradient in the x direction. By adjusting the length of

the pulse, we control the magnitude of the impulse $\Delta p = \int F_x(t)dt$ such that the maximum velocity of the gas is 1 mm/s.

3.2.2 Disordered Insulator

We use the technique described in the last section to measure dissipation as a function of lattice depth s and disorder strength Δ. Using this technique — which is sensitive to very large γ — we found the lattice depth s^* at which the dissipation is infinite (i.e., in-trap velocity is zero). We found the disordered insulator by measuring the change in this transition to an insulator as s and Δ varied.

We measured the position of the insulator transition at three different disorder strengths, $\Delta = \{0, 0.75, 3\}\ E_R$. As shown in Figure 3.7, between $\Delta = 0\ E_R$ and $\Delta = 0.75\ E_R$, the transition does not change significantly, and the velocity becomes consistent with zero above $U/t = 60$ in both the longitudinal and transverse directions. For $\Delta = 3\ E_R$, the transition to insulator moves to a much lower lattice depth corresponding to $U/t = 20$. Even though $\Delta \gg U$ can produce an insulator at high lattice depths (i.e., $s = 10$–$12\ E_R$), at lower lattice depths (i.e., $s = 6$–$10\ E_R$) we do not observe a disordered insulator for the highest Δ we could achieve, contrary to recent numerical predictions [23]. The area on the phase diagram which has become a disordered insulator is shown superimposed on the $\Delta = 0\ E_R$ phase diagram in Figure 3.9. Because the entire gas is insulating when $\Delta = 3\ E_R$ we know that the entire range of effective chemical potentials present in this trap at values $U/t > 20$ are insulating. Conversely, below this threshold, insulating regions may exist in the lattice, but remain undetected. The top of the blue box in Figure 3.9 which marks the disordered insulator is determined by our estimate of the maximum number per site $n = 1$. In Section 3.3.4 I will show how we infer from previous data [39] that for larger n, the entire gas in not an insulator at $\Delta = 3\ E_R$.

Transport measurements were taken between $s = 6$–$18\ E_R$: from a pure superfluid with high condensate fraction, to a nearly pure insulator with zero condensate fraction. Number is kept fixed at $N = 14000$ for all lattice depths we measure. Site-decoupled mean-field-theory calculations show that, in a clean lattice, this corresponds to a maximum density of 1.4 atoms per site at $s = 6\ E_R$ and a Mott-insulator with exactly one atom per site above $s = 13\ E_R$ (see Figure 3.8). We do not have a method to calculate in-trap profiles with a disordered lattice, however we were unable to see a change in the in-trap size when disorder was added to a lattice. This implies that the radius changes by less than 10%, an uncertainty due to the resolution of our imaging system.

3.2.3 Re-entrant superfluid

The so-called "re-entrant" superfluid refers to a superfluid that is produced by adding disorder to an insulator. As was mentioned in Chapter 2, this phase is predicted by several groups [18, 22, 23]. The phase diagram produced in these investigations predict a superfluid

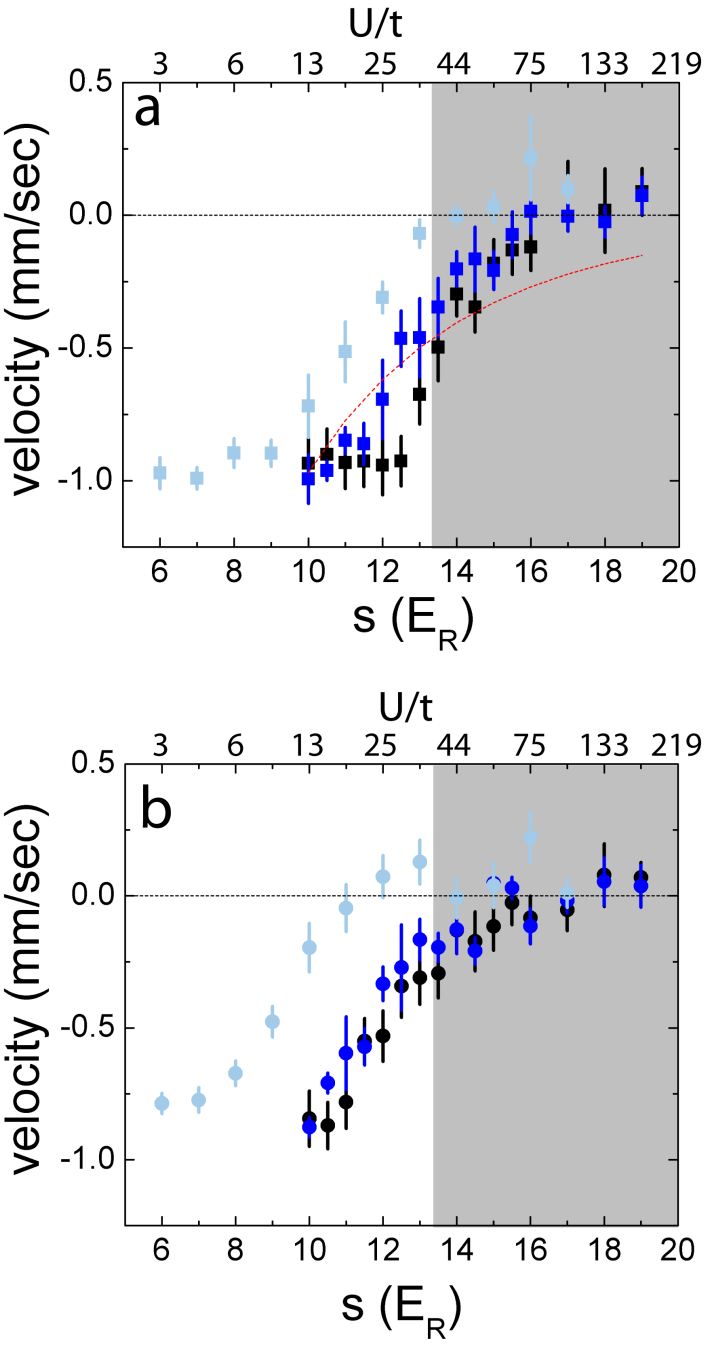

Figure 3.7 Center-of-mass velocity after an impulse in the transverse (**a**) and longitudinal (**b**) directions for $\Delta = 0$ (black), $\Delta = 0.75$ (dark blue), and $\Delta = 3$ (light blue). The red, dotted line indicates the decrease in initial velocity that would only be caused by the change in effective mass in a clean lattice. When the velocity beocomes zero (horizontal dotted lines) the state is an insulator.

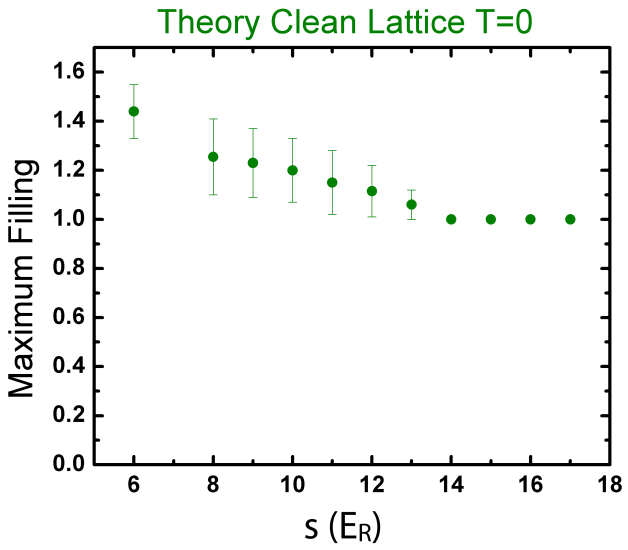

Figure 3.8 Maximum density (atoms per site) plotted against lattice depth from a site-decoupled-mean-field-theory calculation in a clean lattice. The points and error bars are derived from the measured number in transport experiments. Number was kept roughly constant at 15000 atoms. The changing interaction energy, U, causes the maximum density to decrease at higher lattice depths. After $s = 13.3\ E_R$, the middle of the lattice is a Mott insulator.

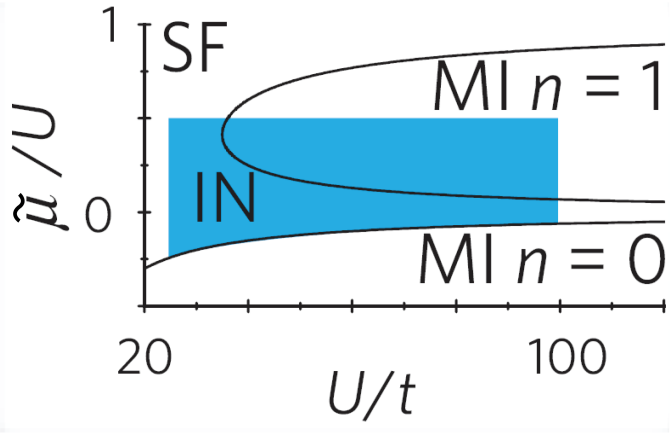

Figure 3.9 Superimposed on a clean Bose-Hubbard phase diagram, the blue box shows the region where $\Delta = 3\ E_R$ disorder creates a disordered insulator. The range of chemical potentials which become insulating reflects the inhomogeneous density in the harmonic trap. The range of U/t reflects the range of lattice depths we measure in our experiment.

"finger" above the Mott-insulating state. To observe this superfluid region, we measured dissipation of COM motion at lattice strengths just above the Mott-insulator transition. For these values of s near the clean superfluid/Mott-insulator transition, we expect to see a re-entrant superfluid phase for the smallest Δ.

However, we did not observe the re-entrant superfluid. We measured the initial velocity at fixed lattice depth, s = 13.5, 14, and 14.5 E_R (near the clean superfluid/insulator transition s = 13.3 E_R), and varied the disorder in the range, Δ = 0–1 E_R. Rather than increasing the observed initial velocity as would occur if a re-entrant superfluid was present, increasing disorder always decreased the initial velocity, as shown for example data in Figure 3.10. For all lattice depths we measured we consistently observed that adding disorder decreased conductivity, precluding the existence of a re-entrant superfluid in our experiment.

The discrepancy between theory and our experiment may be explained by the either finite temperature, the harmonic trapping potential in our experiment, or by differences in the disordered Bose-Hubbard parameters (i.e., off-diagonal disorder). Recent predictions of the re-entrant superfluid by Gurarie et al. [23] do not calculate a critical temperature, but a toy-model suggests that the temperature where the superfluid disappears may be smaller than the temperature in our experiments [126]. Although the QMC calculations that predict a re-entrant superfluid were also calculated for a finite-sized lattice like ours, the chemical potential across the lattice in those simulations was uniform while the effective chemical potential across the lattice in our experiment changes due to the harmonic trapping potential. These theoretical predictions of re-entrant superfluidity also do not consider the strong disorder in t that is present in our experiment.

3.3 Condensate Fraction

Condensate fraction, in addition to the velocity measurements described in the last section, is an important observable we use to study an atomic gas in a lattice. We measure this quantity by fitting the bimodal atomic density distribution after time-of-flight (TOF) imaging. The narrower of the two peaks is defined as the condensate. When the condensate fraction is measured after a bandmapping trap release [137–139], the narrow width of the condensate indicates a smaller range of quasimomenta. The small values of quasimomentum imply both a lower energy and larger spatial coherence than the broader non-condensate. We found that the two quantities, COM velocity after impulse and condensate fraction, are closely related; when the condensate fraction goes to zero, the COM velocity vanishes and the gas is an insulator.

In Section 3.3.1, we will describe how condensate fraction is measured simultaneously with velocity in TOF measurements. Section 3.3.2 will describe how these condensate fraction measurements can be used to find temperature in a clean lattice, and estimate

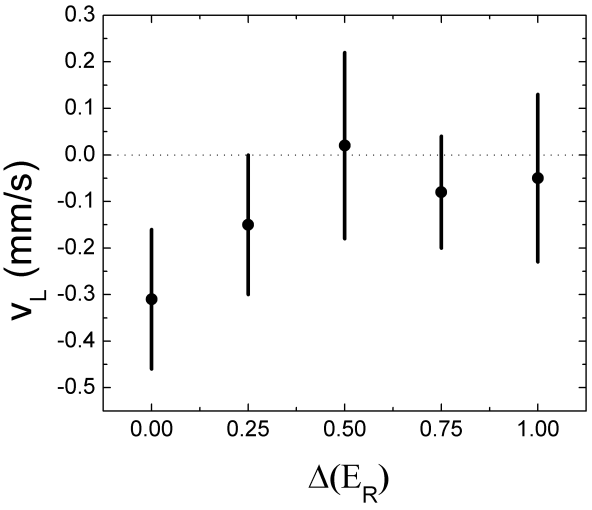

Figure 3.10 COM velocity for $s = 14\ E_R$ after a longitudinal impulse. The velocity monotonically decreases as a function of disorder strength, suggesting a decreasing superfluid fraction and the absence of a re-entrant superfluid. The error bars represent the statistical uncertainty from, on average, 7 runs per point.

the entropy-per-particle in the disordered lattice. Using bounds on temperature, we can show that the superfluid-to-disordered-insulator is not caused solely by heating. Bounds on entropy-per-particle based on condensate fraction measurements may explain the deviation between theory and experiment.

Finally in Section 3.3.3, measurements of condensate fraction combined with the anisotropic shape of the quasimomentum distribution give insight into interaction-induced screening of the disordered potential. A fraction of the atoms become localized, and the repulsive interactions between atoms acts in a way to smooth the nearby disorder through screening depending on the density of localized atoms. We will use this phenomenon of screening to provide an explanation for condensate fraction and velocity vanishing simultaneously. This screening hypothesis also explains the difference in condensate fraction between high and low density gases in disordered lattices.

3.3.1 Measuring Condensate Fraction

We measure condensate fraction using absorption imaging after TOF. Depending on what we would like to measure, we use one of two trap turn-off techniques. When we turn the lattice off quickly using bandmapping, we measure the bimodal quasimomentum distribution which reveals condensate fraction of the gas in-lattice [140, 141]. Numerical simulations show that this bandmapping procedure begins to fail above $k_B T \gtrsim 3t \sim 25$ nK at $s = 6\ E_R$ [139]; we approach this temperature for the "warm" data we will present — meaning we possibly underestimate S/N for warmer gases. Turning the lattice off more slowly, or

"adiabatically", allows us to place an upper bound on the entropy of the gas in-lattice. The appropriate fitting functions used to identify the two parts of the bimodal density distribution are selected based on maximum density to produce consistent results for gases with different numbers of atoms.

Band-mapping converts the lattice quasimomentum to free-space momentum. It does so by turning off the lattice in a way such that the time it takes for the lattice to turn on is slow compared to the period of an individual lattice site, but fast compared to the overall confining trap period; we use a band-mapping time of 200 μs in our experiment. In the lattice, the Bose-condensed atoms occupy the a sharp quasimomentum peak in the lowest band, thus the quasimomentum distribution shows the condensate fraction of the gas in-lattice.

When estimating the entropy per particle in the lattice, we use an adiabatic lattice ramp-off to maximize the condensate fraction (see Figure 3.11). The time scale that maximizes condensate fraction after ramping down the lattice is 15 ms. A gas with higher condensate fraction has lower entropy (see Equation 3.11). Therefore by turning off the lattice in a way that maximizes the condensate fraction after release, this technique adds the smallest amount of entropy possible.

To determine the condensate fraction from an absorption image, the bimodal distribution is fit to two peaked functions (parabolic Thomas-Fermi or Gaussian) with different widths, and in some cases, different center positions. N_0 is defined as the integral of the curve with smaller width. When the condensate fraction is near zero or one, the fitting algorithm is unable to measure very small amounts of condensate or non-condensate respectively. Therefore in these regimes we are unable to determine condensate fraction precisely. We simulated our ability to measure condensate fraction by creating bimodal functions with well defined condensate fraction and adding realistic imaging noise. Using our fitting function to analyze these images produced estimates for upper and lower bounds on the condensate fraction our imaging system is capable of measuring. These bounds are reflected by error bars which extend either to $N_0/N = 1$ or 0 in Figures 3.17 and 3.18.

The function used to fit the atomic gas density distribution after TOF is different for high and low numbers of atoms. When atom number is sufficiently large the kinetic energy of the cloud is small compared to the interaction energy. In this case, the density distribution after TOF [142] is well-described by the Thomas-Fermi (TF) distribution [143],

$$n(\mathbf{r}) = [\mu - V(\mathbf{r})]/U_0 \tag{3.9}$$

where $V(\mathbf{r})$ is the harmonic trap, and U_0 is the interaction energy. Since $V(\mathbf{r})$ is harmonic, the form of the density $n_{TF}(x, y, z)$ is parabolic,

$$n_{TF}(x, y, z) = n_0 \left(1 - \frac{x^2}{w_x^2} - \frac{y^2}{w_y^2} - \frac{z^2}{w_z^2}\right), \tag{3.10}$$

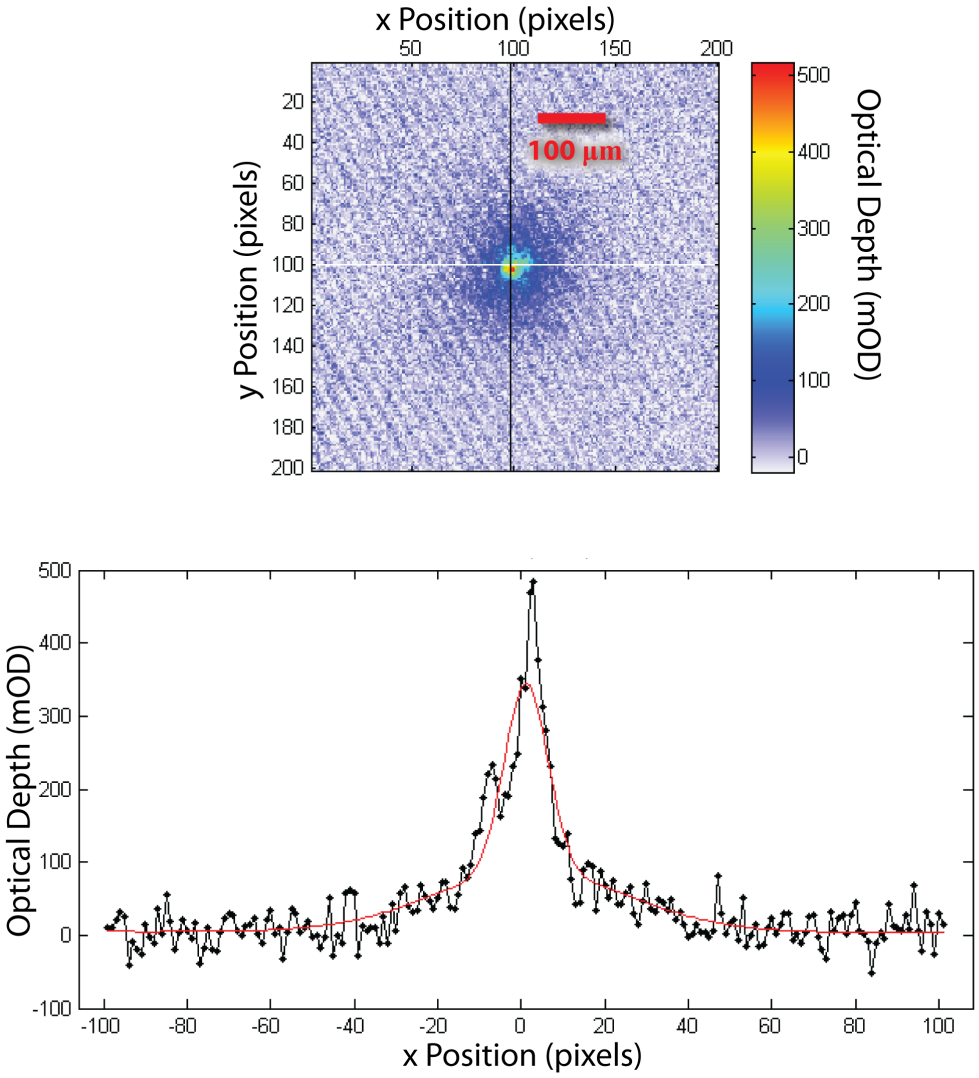

Figure 3.11 An absorption image (top) is fit by two Gaussian functions with separate centers. A vertical, one dimensional slice (along the vertical cross-hair in the top image) is shown with data (black) and fit (red). The image is data taken at $s = 12\ E_R$, $\Delta = 0\ E_R$ after a transverse impulse. The horizontal and vertical positions are in pixels (3.15 μm per pixel) and the color scale is in OD /1000 (optical depth). The narrow central peak (condensate), and the broad tail (non-condensate) have independent centers, widths, and heights.

where n_0 is the maximum density, w_i is the width of the Thomas-Fermi distribution in the x_i direction, where $x_i = \{x, y, z\}$ is the distance from the center of the gas. Because this function is separable, and in the case of our trap nearly isotropic, the condensate column density we image is also parabolic.

At low density the interaction energy is not large enough to produce a sharp parabolic distribution and the condensate will not have a sharp edge. When fit by a two-component function, with a parabolic function for the condensate and a Gaussian function for the non-condensate, our fitting algorithm returns decreasing condensate fraction as the width of the non-condensate approaches the width of the condensate. This would imply that as the energy of the gas decreases the entropy increases, which is not physically possible for a system in equilibrium. Instead, if we use a two component function with two different Gaussian functions to fit the condensate and non-condensate, the condensate fraction always increases as the width of the gas decreases, producing an accurate fit. A Gaussian function is expected to be a better fit at low number because kinetic energy of the condensate becomes comparable to interaction energy of the condensate, thus the atomic cloud is no longer in the Thomas-Fermi regime [142]. We determine the lowest number for which the Thomas-Fermi profile is accurate by fitting nearly pure BECs. When the Thomas-Fermi fit fails, the χ^2 of the residual is minimized by a bimodal distribution in which the average spread in momentum for the Gaussian function is smaller than that for the Thomas-Fermi.

The condensate and non-condensate portions of the gas may have different velocities after an impulse. To simultaneously fit the two components, the centers of the two fitting functions were allowed to vary independently. For these reasons, all of the data for condensate fraction in the low filling limit is fit by two functions which have separate centers if an impulse has been applied. Using this fitting method we did not observe a change condensate fraction within our uncertainty when the two components had different velocities. To ensure this was the case we fit clouds at the same value of s, Δ, and temperature with and without an impulse. Neither the impulse nor the different fitting technique changed the value of N_0/N.

3.3.2 Entropy from Condensate Fraction

Measurement of condensate fraction allows us to place bounds on the entropy per particle of the atoms in a disordered lattice. By measuring entropy before and after loading the gas into a lattice, we can use the second law of thermodynamics to place bounds on entropy while the gas is in the lattice. The entropy bounds allow us to prove that the disordered insulator we observe is not solely caused by heating. Entropy per particle is measured from the condensate fraction of atoms in a bare harmonic trap without the lattice — either before the lattice is turned on, or after it is turned off adiabatically. The bounds on entropy per particle show that the transition to a disordered insulator is reversible. The bounds on entropy per particle may also allow comparison between our experiments and theoretical

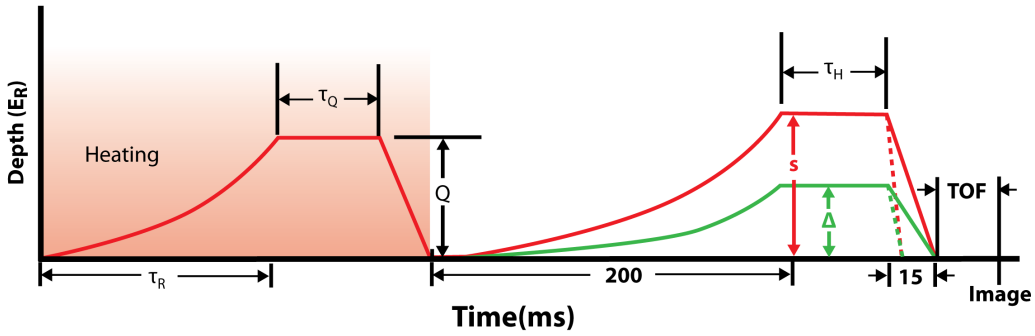

Figure 3.12 A time line showing the intensity of the three lattice beams in red, and disorder in green. When higher temperature is required, he lattice is first turned to a depth Q, using an exponential ramp of length τ_R (typically 200 ms), and then held at Q for time τ_Q (typically 100 ms). The lattice is ramped down slowly, and left off for 30 ms to allow the atoms to reach thermal equilibrium. The condensate fraction in the bare harmonic trap is measured, and Q is adjusted to produce the desired initial temperature. For data taken at the lowest temperature, this heating step is omitted entirely. The disordered lattice potential, consisting of the lattice of height s, and disorder of height Δ, are turned on simultaneously so that the ratio of the power in all beams is fixed. The beams are turned on in an exponential ramp with a time constant $\tau_L = 100$ ms over a total time of 200 ms. Once the lattice is at full strength, an impulse may be applied. In experiments measuring oscillations, the lattice is left on for a hold time τ_{Hold}; in measurements of initial velocity, $\tau_{Hold} = 0$. The disordered lattice is ramped off in either 15 ms for the adiabatic release, or in 200 μs for the bandmapping release (dotted line). The confining harmonic trap is turned off, and the atoms allowed to fall for a time-of-flight (TOF). Finally, we take an absorption image.

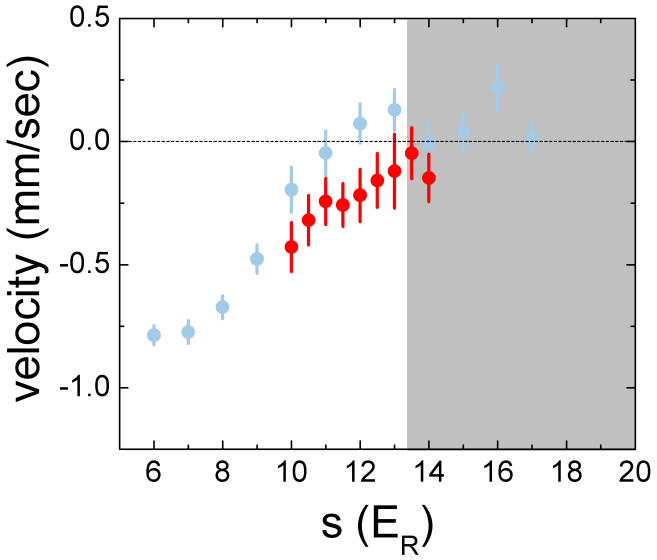

Figure 3.13 Transport measurements comparing high (red points) and low entropy (blue points, see Figure 3.7) gases. The velocity of a gas in a clean lattice with added added heat are compared to a lower entropy gas in a strongly disordered ($\Delta = 3\ E_R$) lattice. The bounds on entropy in the red data are strictly higher than those of the gas in the disordered lattice (see Figure 3.14). This data shows that the transition is reversible, i.e., it is not solely caused by heating.

predictions at finite temperature.

We varied the temperature of the gas before it was loaded into the optical lattice to test if the absence of transport after an impulse is due to increased disorder, or merely increased temperature. We heat the gas by applying a lattice and holding the atoms in it before loading into a disordered potential. The atoms are loaded into a clean lattice for several hundred milliseconds (see Figure 3.12). Varying the depth of the lattice controls the heat added to the gas via spontaneous scattering of the lattice light. After the heating stage, atoms are allowed to thermalize before the disordered lattice is applied. This method does not affect the atom number and allows entropy to be measured in a bare harmonic trap before being loaded into the disordered lattice. To ensure we take data at a consistent temperature, the initial temperature is measured frequently during data collection.

By adding heat to the gas before loading into the lattice, we measured the effects of entropy on the transport properties of the atoms in a lattice. Increasing entropy has been shown to reduce the conductivity of a lattice in prior experiments [71]. We performed transport measurements at $s = 6$–$18\ E_R$, $\Delta = 0$–$3\ E_R$, and for $S/N < 1k_B$ at the lowest to $S/N > 2k_B$ at the highest (see Figure 3.14). The high-entropy gas in a clean lattice had a strictly higher entropy per particle than the maximum bound for the lower entropy disordered insulator. Heating a gas in the clean lattice causes a much smaller change in s^* than does the application of strong disorder (see Figure 3.13). Although the high-entropy, clean lattice had an initial entropy per particle that exceeded the maximum possible entropy per particle of the disordered insulator, the gas in a clean lattice still had finite non-insulator fraction at lattice depths where the disordered lattice was completely insulating. This shows that the gas in a disordered lattice has undergone a phase transition to an insulator which is not caused solely by heating. Figure 3.13 compares a warmer gas in a clean lattice, to a colder gas in a strongly disordered lattice ($\Delta = 3\ E_R$). The warm gas has condensate fraction $N_0/N = 0.45$ before loading into the clean lattice, compared to $N_0/N > 0.9$ for the colder gas we then load into a disordered lattice. The warm gas (red) is still moving after an impulse at lattice depths where the gas in a disordered lattice (light blue) has become an insulator entirely. I will now show how we place bounds on entropy that prove the entropy per particle is higher in-lattice for the warm gas than for the disordered gas.

To estimate the bounds on entropy, we measure the average entropy per particle in a bare harmonic trap where we know the entropy per particle for a given condensate fraction. We measure the entropy per particle twice in a harmonic trap without the lattice; first before the lattice is applied, and then after the lattice is adiabatically turned off. The second law of thermodynamics constrains total entropy (thus the average entropy per particle) to never to decrease over time in a closed system. Thus, the initial entropy per particle S/N before loading the gas into the lattice sets a lower bound. The entropy per particle after release from the lattice sets an upper bound on the in-lattice entropy. Condensate fraction in a

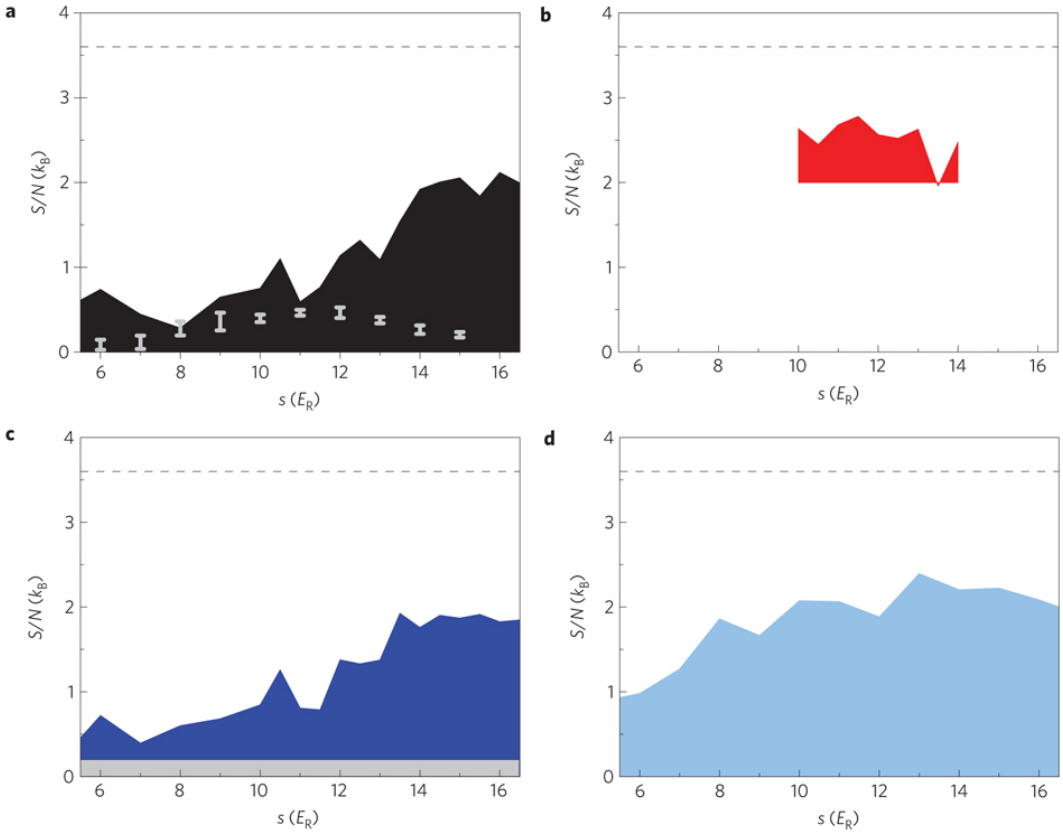

Figure 3.14 The entropy per particle S/N is determined to lie with the colored regions for $\Delta = 0\ E_R$ (black, **a**), $\Delta = 0\ E_R$ at high temperature (red, **b**), $\Delta = 0.75\ E_R$ (dark blue, **c**), and $\Delta = 3\ E_R$ (light blue **d**). The S/N corresponding to the critical temperature in a weakly interacting, parabolically confined system is indicated by the dashed black line. The systematic uncertainty in the lower bound related to resolving high N_0/N is shown by the light-grey band in **c**. The error bars shown in the figure represent the statistical uncertainty from the spread in measured N_0/N used to determine S/N. There is typically both a $0.2k_B$ systematic and $0.2k_B$ statistical uncertainty in the upper bound of S/N.

bare harmonic trap [143] is related to entropy per particle by

$$S/N = k_B 3.6(1 - N_0/N) \tag{3.11}$$

where S is the total entropy, N_0 is the number of atoms in the condensate, and N is the total number. This non-interacting formula can be corrected to take into account interactions [87, 144], however this correction changes the entropy by less than 10 percent for all the data shown in this thesis.

Figure 3.14 shows the upper bound on S/N calculated from N_0/N after adiabatic release versus s for four different regimes: the clean lattice at low temperature (black) or with heating (red), and either $\Delta = 0.75\ E_R$ (dark blue) or $\Delta = 3\ E_R$ (light blue) at lower temperature ($N_0/N > 0.9$ before loading into the lattice). The lower bound on the warm (red) sample exceeds the upper bound on the cooler, strongly disordered gas (light blue). As a check on these bounds on S/N we can compare S/N found by another technique. We find that the S/N determined from band-mapped N_0/N measured in the clean lattice (light-grey points) is close to the lower bound for all s, even though the upper bound increases significantly for $s > 12\ E_R$. We calculate S/N for these points using the local density approximation and site-decoupled mean-field theory to self-consistently solve for the temperature and chemical potential. Above $s \simeq 12\ E_R$ we believe the method of estimating entropy from band-mapped N_0/N underestimates S/N. On the other hand, finding entropy after adiabatic release over-estimates entropy, especially above the Mott insulator transition ($s = 13.3\ E_R$) because the lattice ramp adds heat when crossing the Mott-insulator-to-superfluid transition [145]. The minor, disorder-induced heating implied by the increase in the upper bound for $\Delta = 3\ E_R$ between $s = 8$ and $11\ E_R$ may be the same artefact of this measurement technique.

3.3.3 Screening

Interactions can counteract the strength of a disordered potential. The interactions between delocalized and localized atoms can "screen" the disorder, decreasing its effective strength, and allowing the rest of the atoms to remain delocalized [94, 130]. For low lattice depths ($s = 6\ E_R$, as opposed to the strongly interacting regime where we observe a disordered insulator) we see evidence that the anisotropic disorder distribution begins to localize atoms in the direction where the disorder correlation length is shortest, as shown in Figure 3.15. While a fraction of the atoms become localized, the remaining atoms are still in the condensate. However, in the strongly interacting regime ($s = 12\ E_R$), all atoms become localized, corresponding to vanishing conductivity.

The TOF images in Figure 3.15 reveal evidence that screening is responsible for the destruction of the condensate we observed when a disordered insulator appears. In these images, delocalized atoms appear as a sharp peak, while localized atoms are spread out

to higher quasimomenta. For a clean lattice at $s = 6\ E_R$, most of the atoms are delocalized as shown by the high condensate fraction. When the lattice is disordered by an amount $\Delta = 3\ E_R$, a large fraction of the atoms localize. Instead of localizing isotropically, these atoms have a spread in non-condensate quasimomentum that is twice as large in the transverse direction, where the disorder varies on a shorter length scale as compared to the orthogonal direction. This is demonstrated schematically in Figure 3.16. The width of the condensate quasimomentum does not change. Figure 3.16 shows how the larger spread in quasimomentum implies that the atoms are have a shorter localization length ξ in the transverse direction.

When the lattice depth is increased to $s = 12\ E_R$, the quasimomentum distribution is isotropic in both the clean and disordered case. For $\Delta = 3\ E_R$, the condensate disappears and the non-condensate has the same width as it would for a Mott insulator in a clean lattice. Because the atoms are already localized to single sites, the disorder cannot localize them further. It is important to note that an anisotropic distribution in the quasimomentum distribution is only found in the weakly interacting regime, but never in the strongly interacting regime where we observed the disordered insulator.

Figure 3.17 shows that increasing disorder causes the condensate fraction to decrease for all lattice depths. For the highest disorder strength $\Delta = 3\ E_R$ the condensate vanishes at $s = 12\ E_R$, the same value as s^* (where the entire gas becomes insulating). Sufficiently strong disorder overwhelms the interaction energy and screening is no longer sufficient to allow a delocalized condensate.

3.3.4 Controlling Number

We observe a strong dependence of condensate fraction on the maximum density of a gas in a disordered lattice. The transport measurements described in this thesis were taken in the low-filling regime where the density at the center of the lattice, $\langle n \rangle$, is near 1. In our previous study seen in Figure 3.18, White et al. [39], the central filling was 2–3 atoms per site. In that experiment we observed that increasing disorder for either $s = \{6, 12, 14\}E_R$ (green, red, and blue respectively) always decreases the condensate fraction. The relative difference in condensate fraction between the high and low-filling limits changes when disorder is added; importantly N_0/N vanishes only in the low-filling limit. This section will present this comparison of N_0/N for two different density regimes, as well as the techniques used to collect and analyze the data.

Condensate fraction changes significantly as the maximum density in our lattice is reduced (see Figure 3.19). Comparable data was taken for the high and low-filling regimes at $\Delta = \{0, 0.75, 3\}\ E_R$ and $s = \{6, 12, 14\}\ E_R$. For $\Delta = 0\ E_R$, the differences in measured condensate fractions match the expectations based on theory (see Figure 2.2). At $s = 6$, the two regimes exhibit similarly high condensate fraction, with error bars extending to $N_0/N = 1$. The lattice depths $s = 12$ and $14\ E_R$ fall on either side of the superfluid/Mott-

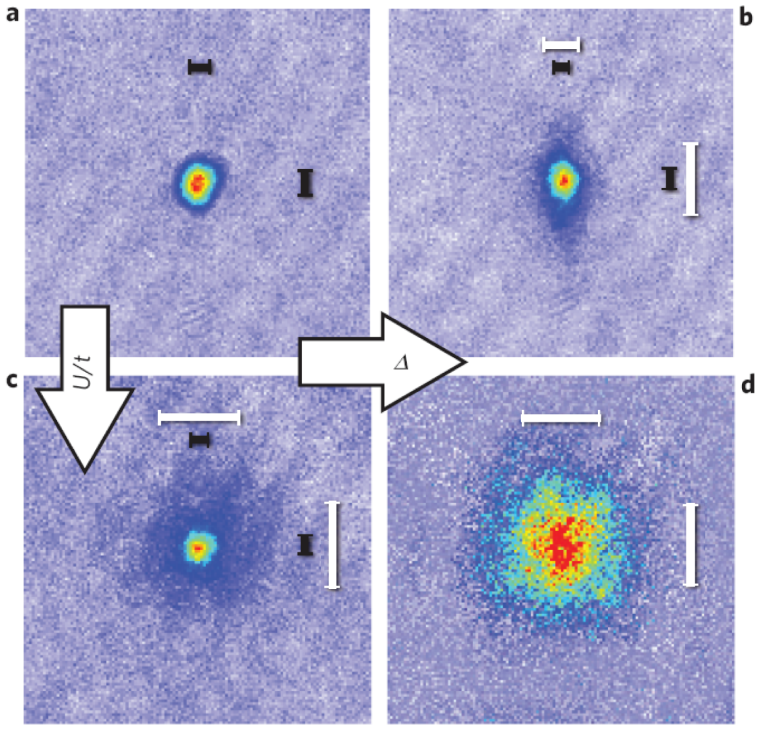

Figure 3.15 Images taken after band-mapping from the disordered lattice and TOF are shown in false color for $s = 6\ E_R$, $\Delta = 0\ E_R$ (**a**), $s = 6\ E_R$, $\Delta = 3\ E_R$ (**b**), $s = 12\ E_R$, $\Delta = 0\ E_R$ (**c**) and $s = 12\ E_R$, $\Delta = 3\ E_R$ (**d**). The TOF is 25 ms for $s = 6\ E_R$ and 15 E_R ms for $s = 12\ E_R$; the field of view for each image is 0.6 mm. The images are fitted to two-component Gaussian distributions to determine the condensate fraction and the sizes and location of the condensate and non-condensate. The black and white bars correspond to twice the fitted r.m.s. radius for the condensate and non-condensate components.

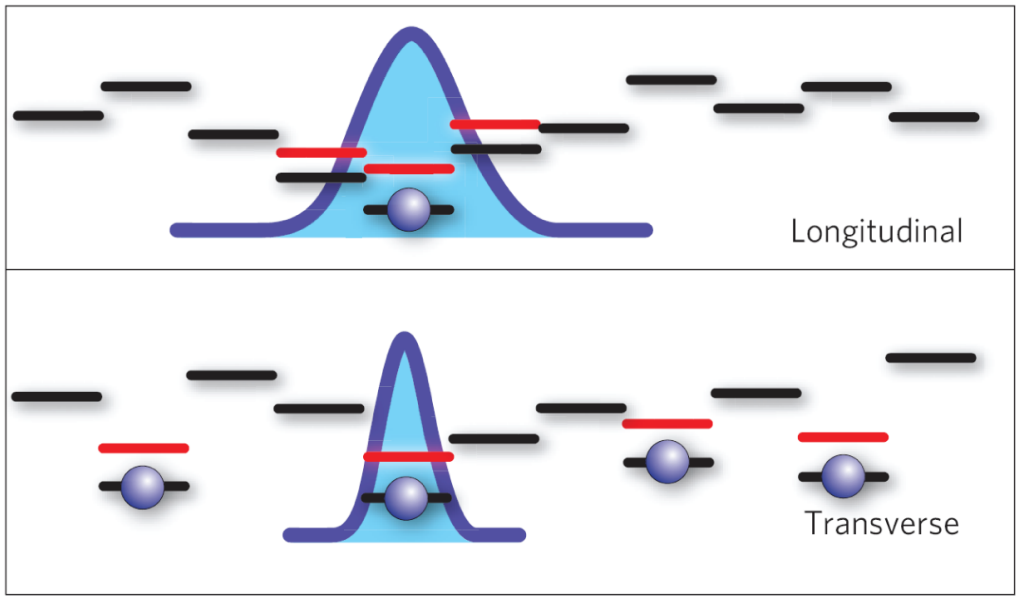

Figure 3.16 A simple model-suggested by the behavior in Figure 3.15 (**b**) that may be used to understand the effect of disorder on the quasimomentum distribution. Atoms (blue spheres) localize to regions (blue curves) to screen the disordered potential (black) and create a more uniform effective potential (red).

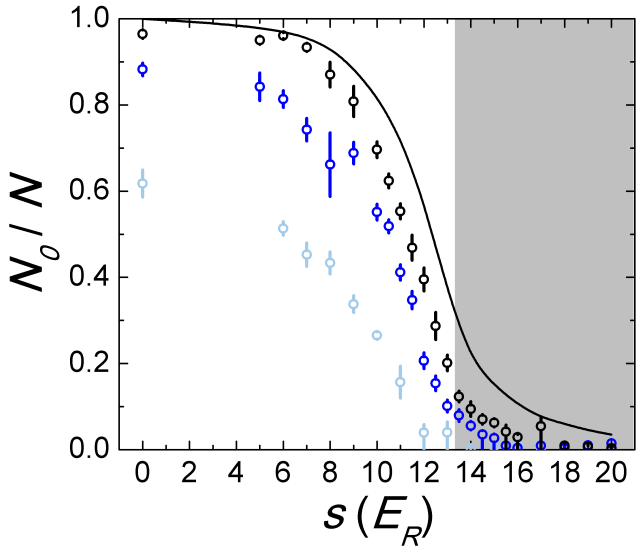

Figure 3.17 Condensate fraction (N_0/N) measured against lattice depth for $\Delta = 0$ E_R (black), $\Delta = 0.75$ E_R (dark blue), and $\Delta = 3$ E_R (light blue) for transport measurements. The black line is the zero-temperature condensate fraction calculated using site-decoupled mean-field theory and measured experimental parameters. The deviation of the experimentally measured clean-lattice condensate fraction and zero-temperature calculation show the data is at finite entropy. For the highest disorder, $\Delta = 3$ E_R, condensate fraction goes to zero at $s = 12$ E_R, compared to $s = 15$ E_R for the lower disorder values. In all three cases, the transition of the entire lattice to an insulator occurs when condensate fraction goes to zero.

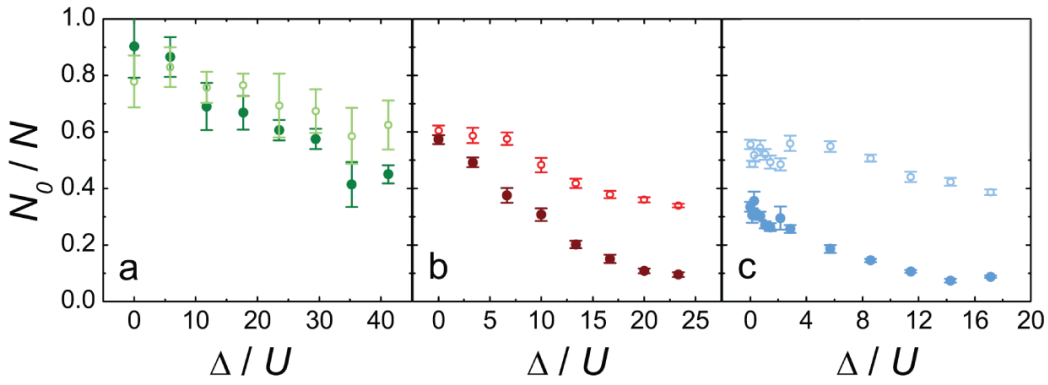

Figure 3.18 Data reproduced from Ref. [39], showing condensate fraction in the high-filling regime (3 atoms per site) for $s = 6\ E_R$ (a), $s = 12\ E_R$ (b), and $s = 14\ E_R$ (c) for bandmap release (closed circles) and adibatic release (open circles). In the high-filling regime, many atoms are in a superfluid at a higher chemical potential than the $n = 1$ Mott insulator. The condensate in this superfluid is robust against disorder. For instance for $\Delta/U = 10$, $s = 12\ E_R$, the condensate fraction after bandmap release nonzero in the high filling limit and consistent with zero in the low filling limit.

insulator transition, which begins at $s = 13.3\ E_R$. At $s = 12\ E_R$, $\Delta = 0\ E_R$, the condensate fraction is lower in the low-filling regime due to the increased fraction of atoms near the $n = 1$ Mott-insulator lobe, which is strongly quantum depleted. Similarly, for $s = 14\ E_R$, $\Delta = 0\ E_R$, a greater fraction of the low-filling lattice is in the Mott insulator or the strongly quantum depleted region adjacent to it. These $\Delta = 0\ E_R$ data show qualitatively different behavior in the low-filling regime, where the inhomogeneous lattice samples the interesting region around the $n = 1$ Mott-insulator lobe.

On the other hand, when disorder is present the condensate fraction in the low-filling regime is always lower than the high-filling regime. Importantly, at $s = 12$ and $14\ E_R$, the condensate fraction goes to zero only in the low-filling regime.

3.4 Properties of Speckle Disorder

To understand the results described in this chapter, it is important to understand the speckle we use to create the disordered lattice and how it may be different from other experiments or theoretical treatments. The optical speckle field we use creates a disordered potential that differs from the white-noise disorder used in most theoretical treatments. This difference from white noise disorder can be summarized into five important features:

- speckle leads to "off-diagonal" disorder in t;
- the first-order intensity distribution is asymmetric with an exponentially decaying tail;
- the anisotropic intensity correlations along non-lattice directions;

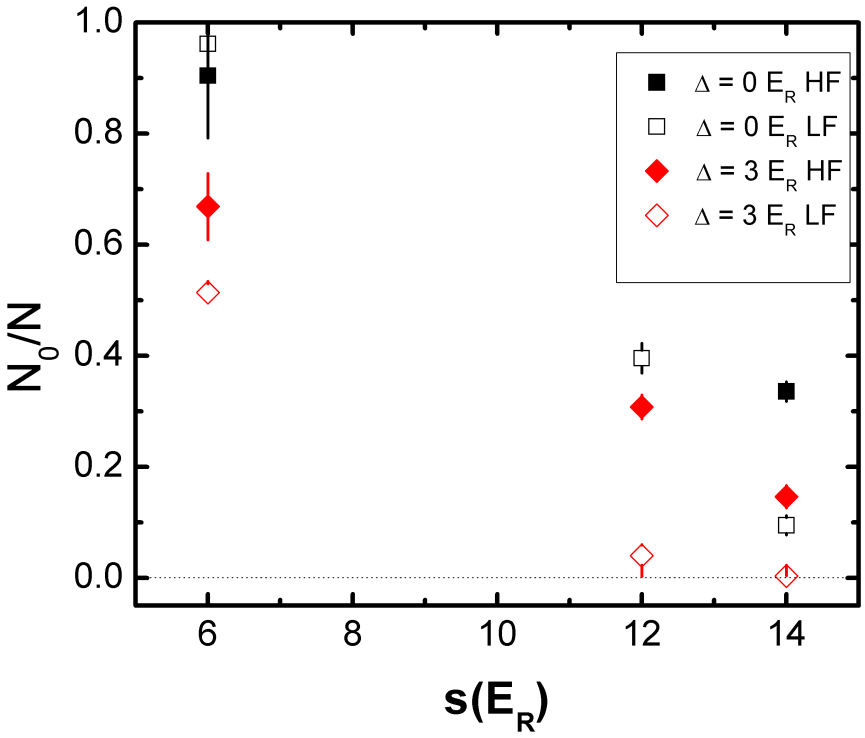

Figure 3.19 A comparison of data from our work in Ref. [39] and Ref. [44], showing condensate fraction in the high-filling (HF) regime (closed points) and low-filling (LF) regime (open points). At high lattice depth s, the condensate fraction measured after bandmapping is lower in the low filling limit than the high filling limit for both clean ($\Delta = 0$, black squares) and disordered ($\Delta = 3$, blue circles) lattices. We found that an insulating state coincided with the condensate fraction N_0/N going to zero. The finite condensate fraction for all disorder strengths we measured in the HF regime indicates that the disordered insulator only exists at LF for the disorder strengths we measured.

- one-dimensional topological defects in the light field create lines of exactly zero disorder which extend across the entire lattice (albeit, not along lattice directions);
- loops of zero-intensity exist in the speckle distribution.

This section will examine how these differences might affect our results. In the well-studied strongly correlated regime, where we observe a disordered insulator, the off-diagonal nature of the disorder in the Bose-Hubbard parameters and the one-sided distribution may be of importance. In the limit of $t \simeq U$, at a much lower lattice depth from where we observed the disordered insulator, the atoms have a longer correlation length. This may cause long-range correlations along non-lattice directions to become more important. A few results from this poorly understood regime will be presented.

Among the points listed above, the off-diagonal nature of our disorder (see Section 2.3.4) is most relevant to the main results of this thesis. Studies of bosons in a one-dimensional lattice with off-diagonal disorder have predicted the existence of both a Bose-glass and Mott-glass phases [116, 146, 147]. Off-diagonal disorder has not been studied in three dimensions, nor has it been included in recent QMC calculations [23].

Also relevant to the strongly correlated regime is the different first-order intensity distribution of speckle compared to white-noise disorder. In the next section we will show that disorder created by speckle can still cause the percolation transition predicted by Gurarie et al. [23]. I reproduce their analysis for our the negative exponential speckle intensity distribution and determine the correct percolation threshold in terms of Δ.

To see the last feature in my list, the effects of anisotropy in speckle disorder, we had to look at low lattice depths where the ratio t/U is much larger, away from where we observed the disordered insulator. We measured transport over a range of Δ in this weakly interacting regime and observed anisotropy in the damping rates. A short discussion of optical vortices — which share the 5.4-to-1 anisotropy — is included; the presence of these topological defects in a disordered lattice may be an interesting topic for future study.

3.4.1 Percolation Transition

The superfluid-to-disordered-insulator phase transition discussed in Section 3.2.2 is predicted to be a percolation transition. In the low-filling regime, disorder excludes atoms from enough sites so that no path of nearest-neighbor-connected, occupied sites exists [23]. A percolation transition is when, in the low filling regime, disorder excludes atoms from enough sites that there is no path of connected, nearest-neighbor, occupied sites across the lattice. Disorder causes sites to be unoccupied by raising the on-site energy ϵ above the chemical potential μ. The disorder strength Δ necessary to produce a percolation transition, and thus a disordered insulator will be derived analytically following the example of Ref. [23] for the case of the optical speckle disorder we use in our disordered lattice.

The percolation transition that is predicted to cause the superfluid-to-disordered-insulator transition in the low-filling limit [23] must be modified for the disorder distribution used in our experiment. For our speckle disorder, the first-order intensity distribution (the probability of the disorder having value intensity I at a given site) is a negative exponential $P(I) = \frac{1}{\bar{I}} e^{-I/\bar{I}}$. This negative exponential distribution is asymmetric with all disorder occuring higher than the $\epsilon = 0$ E_R mode of the distribution. The intensity distribution is also unbounded: $P(I)$ is nonzero for all positive values of I (up to a very high cutoff determined by the total power in our speckle beam divided by the spot size of the focusing optics). The negative exponential disorder distribution changes the critical lattice depth s^* where the disordered insulator transition occurs compared to white noise disorder. The critical disorder necessary to create an insulator we observed experimentally is similar to the value predicted in Ref. [23]. Considering that the Mott insulator is predicted to become a Bose glass at $\frac{\Delta}{U} = 0.5$, it is striking that the transition between superfluid and disordered insulator takes place at $\frac{\Delta}{U} > 10$.

To predict the disorder strength Δ necessary to produce a percolation transition, we first find the average occupation a single site with on-site energy ϵ and interaction energy U. We then average over a distribution of ϵ with average disorder Δ. We set this disorder-averaged probability of occupation equal to the critical occupation for a percolation transition to find the value of Δ where the disordered insulator forms.

We can estimate the change in density due to disorder near the superfluid-to-insulator transition when $\xi \sim d$ [148], where ξ is the correlation length of the atoms, and d is the lattice spacing. In this regime, we can approximate the density on each lattice site using a localized Hamiltonian,

$$H_{loc} = (\epsilon - \mu)n + \frac{U}{2} n(n+1). \tag{3.12}$$

We can find the minimum in H_{loc} with respect to n by taking the derivative,

$$\frac{dH_{loc}}{dn} = \epsilon - \mu + \frac{U}{2}(2n+1), \tag{3.13}$$

solving for n gives

$$n(\epsilon) = \frac{\mu - \epsilon + \frac{U}{2}}{U}. \tag{3.14}$$

To take disorder into account, an average is taken over all values of ϵ within a disorder distribution, $P(\epsilon)$. The average density is then,

$$\langle n \rangle = \int_{-\infty}^{\infty} P(\epsilon) n(\epsilon) d\epsilon \tag{3.15}$$

$$= \int_{-\infty}^{\infty} P(\epsilon) \frac{\mu - \epsilon + \frac{U}{2}}{U}. \tag{3.16}$$

For uniform ("box" distribution) disorder distribution (most often considered in theory because of the ease of calculation [23]):

$$P(\epsilon) = \begin{cases} \frac{1}{2\Delta} & \text{if } \Delta \geq \epsilon \geq -\Delta, \\ 0 & \text{otherwise.} \end{cases} \tag{3.17}$$

Negative densities cannot exist; so to limit n to positive values the integral is truncated at $\epsilon = \frac{U}{2} + \mu$. Next we set the density to the average site occupation we would like to investigate, in this case unit filling, and solve for μ.

$$\langle n \rangle = \frac{1}{2\Delta} \int_{-\Delta}^{U/2+\mu} \frac{\mu - \epsilon + \frac{U}{2}}{U} d\epsilon \tag{3.18}$$

$$= \frac{U/2 + \Delta + \mu}{4\Delta U} = 1, \tag{3.19}$$

which implies

$$\mu = -\frac{U}{2} - \Delta + 2\sqrt{U\Delta}. \tag{3.20}$$

The probability that a given site is occupied (i.e., $n = \frac{\mu - \epsilon + \frac{U}{2}}{U} = \frac{-\Delta + 2\sqrt{U\Delta} - \epsilon}{U} = 0$) is just the probability of the disorder on that site being less than a critical value, $\epsilon_c = 2\sqrt{U\Delta} - \Delta$. This probability, p_c is defined

$$p_c = \int_{-\infty}^{2\sqrt{U\Delta}-\Delta} P(\epsilon) d\epsilon \tag{3.21}$$

$$= \frac{1}{2\Delta} \int_{-\Delta}^{2\sqrt{U\Delta}-\Delta} d\epsilon \tag{3.22}$$

$$= \frac{1}{2\Delta}(2\sqrt{U\Delta} - \Delta + \Delta) = \sqrt{\frac{U}{\Delta}}. \tag{3.23}$$

A three-dimensional lattice has a percolation threshold of $p_c = 0.31$ [127]. Setting $\sqrt{\frac{U}{\Delta}} = 0.31$ gives $\frac{\Delta}{U} \simeq 10$ as the critical disorder strength for the percolation transition. The probability that a site will be unoccupied is different between the exponential disorder distribution we use, and the "box" distribution used most often theoretically. The result of the difference is that we would require a higher disorder strength Δ to cross the percolation threshold as shown in Figure 3.20.

The analysis above was predicted to work in the region $\frac{U}{t}$ = 1–30 [23]. While we see agreement in the region $\frac{U}{t}$ = 15–30, we do not observe an insulator transition at lower $\frac{U}{t}$. The disorder needed to cross the percolation threshold is proportional to the density. This is important because the gas at low lattice depths has slightly higher than unit filling. An increase in density from 1 to 1.4 atoms per site (see Figure 3.8) would only require

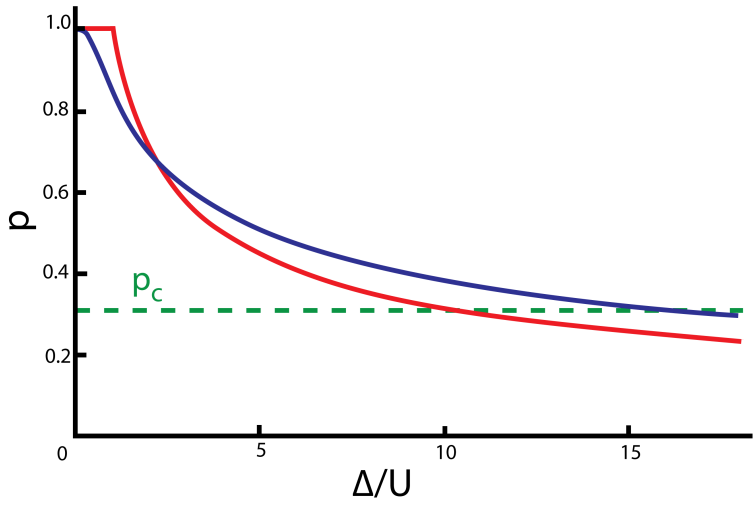

Figure 3.20 Using a localized Hamiltonian as in Ref. [23], the probability of a lattice site being occupied for an average filling $\langle n \rangle = 1$ is plotted against Δ/U. The two lines represent results for a uniform box (red) distribution between $[-\Delta, \Delta]$ and a negative exponential distribution (blue) $P(\epsilon) = \frac{1}{\Delta} e^{-\epsilon/\Delta}$, where $P(\epsilon)$ is the probability of a site having disorder ϵ. The dotted line at p_c is the three-dimensional percolation transition for a cubic lattice.

1.4 times more disorder to cause a percolation transition. Since U is four times lower at $s = 6\ E_R$ than at $s = 12\ E_R$, we would expect to observe an insulator transition at lower disorder at $s = 6\ E_R$ than at $s = 12\ E_R$. The fact that we do not observe a disordered insulator transition at $s = 6\ E_R$ suggests that other differences between experiment and theory need to be considered (such as off-diagonal disorder, or harmonic confinement), or that the theory does not correctly solve the disordered Bose-Hubbard model in this regime.

3.4.2 Anisotropic Behavior

This section will examine the role speckle potential anisotropy plays in a weakly interacting disordered lattice for transport along a non-lattice direction. We observed increased dissipation at low lattice depths for impulses along the direction where disorder has a short correlation length (transverse), but not in the direction with long correlation length (longitudinal). This anisotropic dissipation suggests that the speckle width plays a role in our finite-sized system in the non-quantum-depleted superfluid regime. The dependence of dissipation on speckle autocorrelation length may be responsible for the absence of the predicted disordered insulator at low lattice depth.

To be clear, we observed no anisotropic behavior in the quantum-depleted regime where a disordered insulator was observed, nor do we believe the anisotropy of the speckle has any effect in that regime. All of the transport measurements and quasimomentum distributions in the strongly-interacting regime are completely isotropic.

We measure dissipation when motion is underdamped by exciting a dipole oscillation for the gas COM. We measured the change in the oscillation's damping rate γ as disorder

strength was increased. These (unpublished) data show that dissipation is not strongly affected by disorder for $s = 12\ E_R$, nor for $s = 6\ E_R$ for an impulse in the longitudinal direction. However, for impulses along the transverse direction for $s = 6\ E_R$, the damping rate γ increases by a factor of five as disorder is increased. This increase in damping plateaus around $\Delta/U = 0.3$ as shown in Figure 3.21.

The difference in the behavior of γ between transport in the longitudinal direction, where the disorder autocorrelation length $\sigma_L = 3\ \mu$m, and the transverse direction where $\sigma_T = 570$ nm, indicates the importance of the speckle autocorrelation length in this regime.

We measure the damping rate by the method discussed in Section 3.2.1. We varyied the disorder strength Δ, and hold time t_h, while keeping the lattice depth s, temperature before loading into the lattice, and total atom number N fixed. The measured velocities are fitted (with fixed s and Δ), to a decaying sinusoidal function

$$v(t_h) = v_i e^{-t_h\gamma} \cos[\omega_L(t_h - t_0)] + v_0, \tag{3.24}$$

where $v(t_h)$ is the velocity, and v_i, ω_L, t_0, and v_0 are fit parameters for the initial velocity, frequency, phase offset, and offset velocity, respectively. When $\gamma \ll \omega_L$ (the underdamped regime), the parameters v_i, ω_L, and t_0 are independent of the disorder strength. The oscillation frequency at a given lattice depth is dependent on the effective mass m^* of the atoms, and the damping rate γ. The amplitude of the oscillation $v_i = \frac{F_m\tau}{m^*}$ in controlled by the impulse $F\tau = \int F(t)dt$ (F is the maximum average force).

For $s = 6\ E_R$, deep in the underdamped, superfluid regime, γ is the same in both impulse directions when $\Delta = 0\ E_R$. For an impulse in the longitudinal direction, disorder does not increase γ significantly over the interval $\Delta = 0$–$1.2\ E_R$, corresponding to $\frac{\Delta}{U} = 0$–8. However, in the transverse direction, disorder dramatically changes the damping rate. On the interval $\frac{\Delta}{U} = 0$–2, γ increases from $2\pi\cdot 12$Hz to $2\pi\cdot 60$Hz. Over $\frac{\Delta}{U} = 2$–6, γ stays roughly constant. The data at $s = 6\ E_R$ are in the low filling limit with $N = 7000$ total atoms in the lattice.

This data presents two interesting features that have not been explained theoretically. First, we observe strongly anisotropic damping in the non-quantum-depleted superfluid regime that we do not observe at higher lattice depths. In this regime, increasing the disorder strength causes damping to increase by a factor of 5, although only in the transverse direction. The second interesting feature is the plateau in damping rate above $\Delta/U \simeq 0.3$ ($\Delta/t \simeq 1$). Increasing disorder above this value does not cause any additional dissipation. This phenomenon of anisotropic damping deserves more experimental and theoretical study.

3.4.3 Optical Speckle Topological Defects

The optical speckle potential that produces disorder in our experiment contains topological defects. These defects appear as dark lines that cross the entire gas of atoms or as small

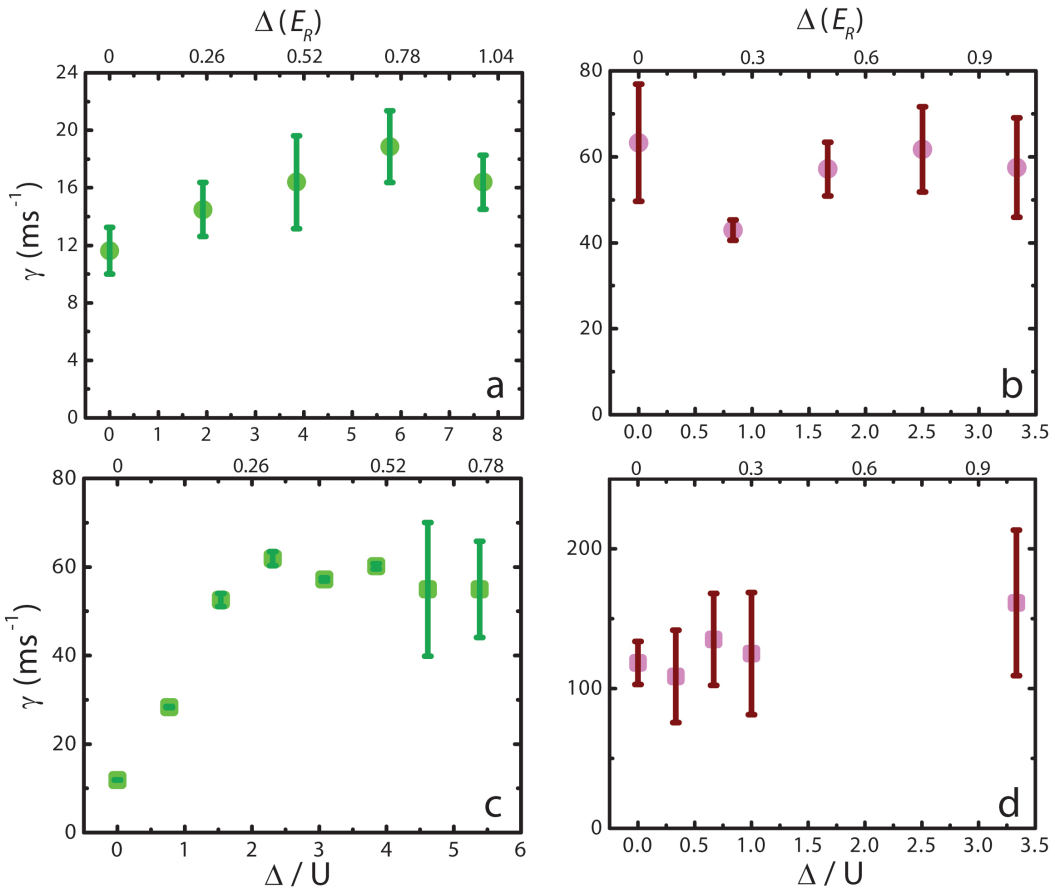

Figure 3.21 The damping rate γ for $s = 6\ E_R$ (green **a**, **c**) and $s = 12$ (purple **b**, **d**) plotted against Δ/U for longitudinal impulses (**a**, **b**) and transverse impulse (**c**, **d**). Damping was measured by applying an impulse to the atoms and fitting the velocity versus time to a damped sinusoidal function with damping rate γ. The measurement technique begins so loses sensitivity for high γ, requiring the use of initial velocity measurements in the strongly overdamped regime.

loops of zero intensity. When $t \sim U$ it may be possible for these dark lines to affect transport in the lattice. We expect that any effect of these dark lines will reflect a 5.4-to-1 anisotropy which they share with the speckle autocorrelation function. In the regime where $U \gg t$ ($s = 8$–$18\ E_R$), we observed no anisotropy either in the quasimomentum distribution of the atoms, nor in transport. This suggests that in the strongly interacting regime where the main results of this thesis were measured, these topological defects play no role.

The monochromatic optical speckle field that creates our disordered potential contains phase singularities where the intensity is zero. A phase singularity occurs in the light field when the phase winds 2π around a single point where the phase is not defined and the intensity is zero. These singularities are topological defects in the complex amplitude of the monochromatic laser beam. Because they are topological defects, they propagate along the laser until they annihilate with a singularity of opposite winding, or they leave the beam.

Consequently, the disordered potential we use has one-dimensional lines of zero intensity that run through it. The aspect ratio of our beam means the tubes move 5.4 times further along the longitudinal direction than along the transverse direction (see Figure 3.22). In the absence of a lattice, atoms may propagate along these tubes while experiencing a much smaller disorder intensity on average than would have occurred for truly random disorder. Given the anisotropy in dissipation we observed at low lattice depths (see Section 3.4.2), it is important to understand if these vortices play a role in transport. This feature of our speckle field should also be considered when looking to explain the absence of a disordered insulator at low lattice depths.

3.5 Conclusion

This concludes the portion of this dissertation discussing transport in the disordered Bose-Hubbard model. I have presented measurements showing a superfluid-to-disordered-insulator phase transition in a strongly interacting gas of atoms caused by strong, fine-grain optical-speckle disorder in a 3D optical lattice. Along with the COM velocity we have measured the condensate fraction in the lattice and have shown that dissipation of the COM motion becomes infinite when the condensate fraction vanishes. In these experiments we found the lattice site filling and placed bounds on the entropy per particle in the disordered lattice using the second law of thermodynamics. Using these bounds on entropy, we showed that the disordered insulator is not solely due to heating.

The disordered insulator we found in our experiment exists only at lattice depths where $U/t > 20$ and for $\Delta = 3\ E_R$. A superfluid-to-disordered-insulator transition at this disorder strength matched recent theoretical predictions [23]. However we did not observe a disordered insulator at lattice depths below $U/t = 20$, as was predicted. From measurements of the momentum distribution after band-mapping we showed evidence that the disorder was being screened by interactions at $s = 6\ E_R$. Another commonly predicted feature of the

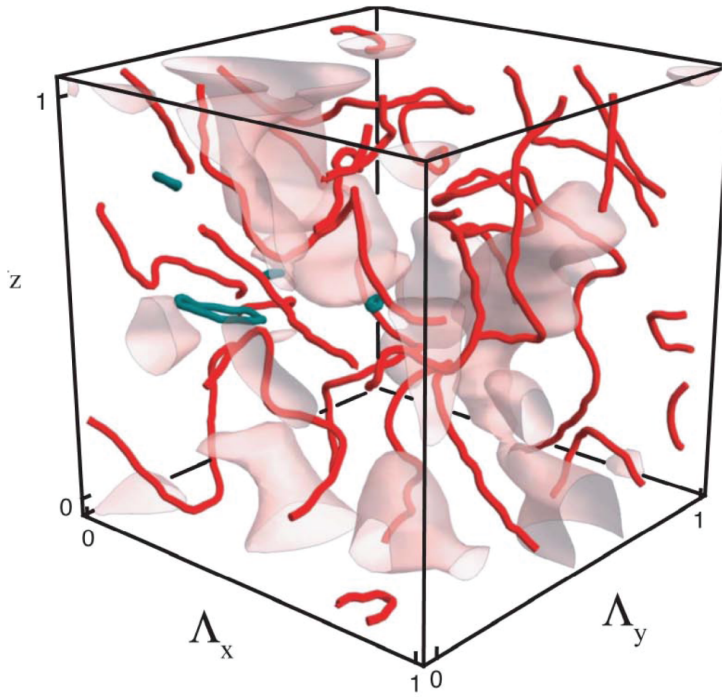

Figure 3.22 A calculated speckle potential reproduced from Ref. [149] in a Talbot cell. The red lines represent topological defects in the speckle potential where the intensity is zero. Green lines are topological defects which loop on themselves and therefore have compact support. The transparent surfaces represent the isopotential curves for $\epsilon = \Delta$. For our speckle potential $\Lambda_x = \Lambda_y = z/a$, where $a = 5.4$ is the aspect ratio of the speckle autocorrelation function.

disordered Bose-Hubbard phase diagram we did not observe was a predicted "re-entrant" superfluid above $s = 13.3\ E_R$. The differences between these theoretical predictions and our results may be caused by the finite temperature of the gas or by differences in the disordered lattice in our experiment from the type of lattice considered in theory.

To account for these differences, the disordered optical lattice in our experiments was measured in detail, and these measurements were used to determine the disordered Bose-Hubbard Hamiltonian that describes the atoms in our disordered lattice. Using a microscope and translation stage, we were able to measure the 3D intensity distribution of the optical speckle field which produced our disorder. We showed that this intensity distribution matched both analytical calculations as well as computer simulations which took into account the optics in our experiment. Using this precise knowledge of our disorder, the Ceperley group was able to calculate the distribution of parameters for the disordered Bose-Hubbard Hamiltonian which describes the gas in our disordered lattice. They showed strong "off-diagonal" disorder in the hopping energy t. This off-diagonal disorder was correlated with a difference in the nearest neighbor on-site energies ϵ. This showed that the fine-grain nature of our disorder was important in causing off-diagonal disorder.

In this work we did not identify the type of disordered insulator we measured. To fully characterize the phase diagram, local measurements need to be made that do not have multiple phases present simultaneously. Next, each of these phases will need to be characterized using measurements of transport, the excitation spectrum, and compressibility. Using transport, the superfluid and insulating states can be discerned. Using measurements of the excitation spectrum and compressibility, we will be able to determine in the future if an insulator is a Mott insulator or a glassy phase like the Bose or Mott glasses. Our group is currently developing a new imaging scheme to realize these measurements.

Chapter 4

Holographic Optical Potentials

4.1 Introduction

Laser light can be shaped by digital computer-generated holograms (CGH) to produce arbitrary 2D optical potentials for ultra-cold atoms. These potentials are made possible by two advances: algorithms which calculate the CGH, and spatial light modulators (SLMs) which display these holograms. When we began investigating holography soon after I arrived in Illinois, the algorithms available were not suitable for creating optical potentials for ultra-cold atoms. We have since solved this problem by creating a new algorithm to create CGHs. This algorithm creates holographic optical potentials that are, for the first time, sufficiently accurate and smooth to trap ultra-cold atoms. When we tried to implement these holograms experimentally however, the SLM we used was unable to display the holograms faithfully. In the years since we worked on this problem, advances in SLM fabrication, as well as new experimental techniques, have enabled SLMs to utilize our algorithm and produce arbitrary holographic optical potentials [50].

This chapter is divided into halves: the first is on using iterative algorithms to design digital holograms capable of producing ultra-cold atom traps; the second is about the spatial light modulators used to produce these holograms experimentally.

4.2 Digital Holography

The intensity profile of optical fields can be controlled by using a computer-generated digital phase raster, also called a computer-generated hologram. The raster, or kinoform, changes the complex phase of the optical field at each pixel without attenuating the amplitude. The CGH, physically implemented using a spatial light modulator or similar technology, is illuminated by a monochromatic beam which is relayed to a focusing objective; the desired intensity distribution is produced at the focal plane of the objective. CGHs have been used in a wide range of technological applications and physical research. For example, soft matter and biological systems have been manipulated using dynamic arrays of focused beams (i.e., optical tweezers) created using CGHs (see [150] for a review), and CGHs have been used to shape laser beams for inertial confinement fusion experiments [151–154].

Before we began working on digital holography, CGH technology had been applied

to experiments involving ultra-cold atom gases. However, that work has been limited to arrays of optical dipole traps [155–158]. Since an effective algorithm for producing CGHs for ultracold atom potentials has been found, this work is beginning to applied to experiments with smooth potentials [50]. New applications of optical dipole potentials for cold-atom research, such as interferometers [46] and atom "transistors" [48], may be realized using high-quality arbitrary light intensity profiles.

The trapping potential for an atom confined in an optical dipole trap is proportional to the light intensity, and therefore the properties of the intensity profile created by a CGH are critical for such applications. Desirable features of a CGH applied to trapping ultra-cold atoms include accuracy in matching the desired intensity profile, smoothness of the profile generated by the CGH, and efficiency in diffracting light into the target profile. Smoothness, of particular importance for ultra-cold atom experiments, has received limited attention in previous work on CGHs [159, 160] and eliminates techniques to generate complex spot arrays as useful for this application (see [161, 162], for example). Disorder related to small-length-scale intensity fluctuations in an optical potential, while useful for studying the disordered Bose-Hubbard model (for instance), when uncontrolled introduces complications for interferometric applications [163–166]. Previous measures used to analyze the roughness of intensity profiles created using CGHs could only be applied to uniform distributions; to study arbitrary smooth optical traps, we introduced a new roughness metric appropriate for continuous profiles. Some constraints related to CGHs may be relaxed for ultra-cold atom applications—a CGH in this context is not required to control the intensity in the entire focal plane, since ultra-cold atom gases are typically confined to a finite region of space.

Calculating a CGH to generate a high-quality arbitrary light intensity distribution is a challenging problem, because a CGH cannot be directly computed, in general, from a desired arbitrary intensity profile. One technique for calculating a CGH when an exact solution is unknown is to use an iterative Fourier-transform algorithm (IFTA), which is computationally efficient compared with other methods, such as a direct binary search [167, 168]. An IFTA predicts the propagation of a beam through an initial kinoform by fast Fourier transform (FFT), and then successively modifies the kinoform based on a comparison between the predicted and desired focal plane intensities. The most frequently used IFTAs for calculating CGHs are variants of the Gerchburg-Saxton (GS) and Adaptive-Additive (AA) algorithms [159, 169–173].

In this chapter, I present a new IFTA that we call the "mixed-region amplitude freedom" (MRAF) algorithm. The MRAF algorithm typically improves by one order of magnitude on accuracy and and two orders of magnitude on roughness compared with the GS and AA algorithms for continuous target profiles. To our knowledge, no algorithm for creating CGHs with a comparable level of computational complexity surpasses the MRAF algorithm in measures of accuracy and roughness. The MRAF algorithm controls intensity in a bounded two-dimensional subset of the focal plane and achieves accuracy at the percent

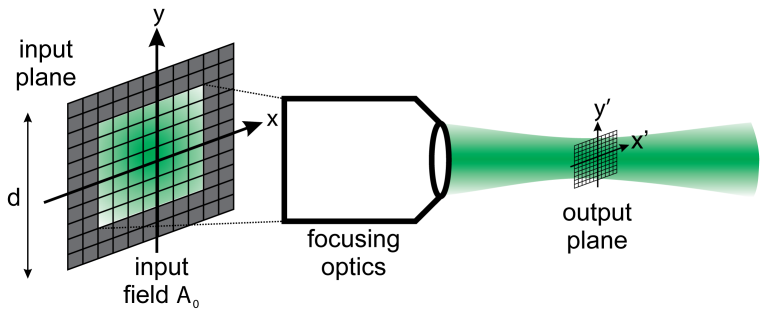

Figure 4.1 Schematic geometry for an IFTA. The optical field that propagates from the input to the output plane through a focusing objective is shown in green. The field is discretized using coordinates (x, y) in the input plane and (x', y') in the output plane. The dashed lines represent the clear aperture of the focusing optics. The matrix used to computationally represent the input field must be enlarged beyond this region and filled with zero intensity points (dark gray) to fully resolve the output plane. The physical size of the matrix used to represent the input plane is d.

level at typically the cost of a factor of three in efficiency (compared with the GS and AA algorithms). Because the MRAF algorithm controls the intensity profile in a single plane, this method can only be applied to creating two-dimensional arbitrary optical traps. Atoms must therefore be confined to the focal plane of the focusing objective to ensure interaction with light only in that plane; this can be accomplished using an additional tightly focused sheet of light. In Section 4.2.1 the MRAF algorithm is explained in detail, and in Section 4.2.4 I report on the algorithm performance for six target intensity profiles.

4.2.1 IFTA Algorithms

Before giving the mathematical details of the MRAF algorithm, I will briefly review the operation of an IFTA (see ref. [174] for a much more general treatment). An IFTA is a technique to solve the following problem: design a CGH that will convert a light field $A_0(x, y)$ at the CGH, or input plane, into a target intensity distribution $I_0(x', y')$ at the focal, or output, plane of a focusing optic (see Figure 4.1) (to make our symbols more legible, in the rest of this chapter I may not explicitly state the (x,y) dependence of the 2D input and output functions). The light field A_0 is typically a Gaussian beam apodized by the input aperture of the device used to implement the CGH. The IFTA problem does not have a unique solution, as the complex phase of the optical field associated with I_0 is not constrained. This is known as phase freedom; there is a choice of phase in the output plane [170, 175]. Complete phase freedom is allowed for far-off resonance optical atom traps because the phase of the field in the output plane does not contribute to the trapping potential if the light is far-detuned from an electronic transition and if the dipole approximation is valid. An IFTA is designed to use phase freedom to minimize the difference between I_0 and the intensity distribution produced by the CGH in the output plane.

An IFTA can be decomposed into two parts as illustrated in Figure 4.2: an initialization step and an iterative loop. In the initialization step, a phase distribution $K_0(x, y)$ is chosen

as a starting point for the algorithm and is imprinted on A_0 to produce the input field $E_{in}^{(1)}(x,y) = |A_0|e^{iK_0}$ for the first iteration (we assume a flat phase for the input profile WLOG). Each iteration n of the loop begins by calculating the field $E_{out}^{(n)}(x',y') = \mathcal{F}\left[E_{in}^{(n)}\right]$ produced by $E_{in}^{(n)}$ propagating to the output plane. The propagation is modeled using a Fourier transform $\mathcal{F}$, which assumes the paraxial approximation for the focusing optics [42]. The algorithm then combines the propagated field $E_{out}^{(n)}$ with the target intensity profile I_0 to produce a new field $G^{(n)}(x',y')$. This procedure is carried out using one or more numerical scalars called mixing parameters m. The phase of the backward propagated field $\arg\left[\mathcal{F}^{-1}\left[G(n)\right]\right]$ is used as the starting phase distribution for the next iteration.

The iterative loop is terminated after N iterations once a figure-of-merit η, calculated using the intensity profile in the output plane and I_0, does not improve with repeated iterations. The phase profile $K_f(x',y') = \arg\left[E_{in}^{(N+1)}\right]$ of the field in the input plane for the final iteration is the kinoform which must be transferred to a physical device. An ideally implemented CGH will produce the predicted intensity profile $I_f(x',y') = |E_{out}^{(N)}|^2$ in the output plane. The goal of using an IFTA to design a CGH is to choose mixing parameters that optimize one or more measures calculated on the predicted profile I_f, such as the deviation from I_0. Achieving this goal will typically require executing an IFTA multiple times with different selections of mixing parameters as part of an optimization scheme [176].

Central to the MRAF algorithm is the introduction of amplitude freedom into a restricted region of the output plane and the use of a single mixing parameter. The mathematical details of the MRAF algorithm are given in Section 4.2.2. The use of amplitude freedom in the MRAF algorithm is not sufficient to generate a high-quality optical field—a choice of initial phase that eliminates optical vortices from the output plane for all iterations is also necessary. I outline a procedure for choosing appropriate initial phase distributions in Section 4.2.3. Additionally, I suggest a method for improving and automating this process in Section 4.2.5.

4.2.2 MRAF Algorithm

At each step n of the MRAF algorithm, the propagated field is combined with the target intensity distribution according to:

$$G^{(n)} = \left\{ m\sqrt{I_0}|_{SR} + (1-m)\left|E_{out}^{(n)}\right|_{NR} \right\} e^{i\arg\left[E_{out}^{(n)}\right]}. \tag{4.1}$$

A single mixing parameter m controls the relative distribution of optical power in two subsets, the signal region (SR) and noise region (NR), of the output plane. Phase freedom is permitted everywhere in the output plane (the phase of the propagated field is used for the phase of $G^{(n)}$), while amplitude freedom is allowed only in the noise region. Even though the mixing parameter m is kept fixed, the fraction of power in each region changes for every iteration; the only constraints imposed on the MRAF algorithm are that the power in the

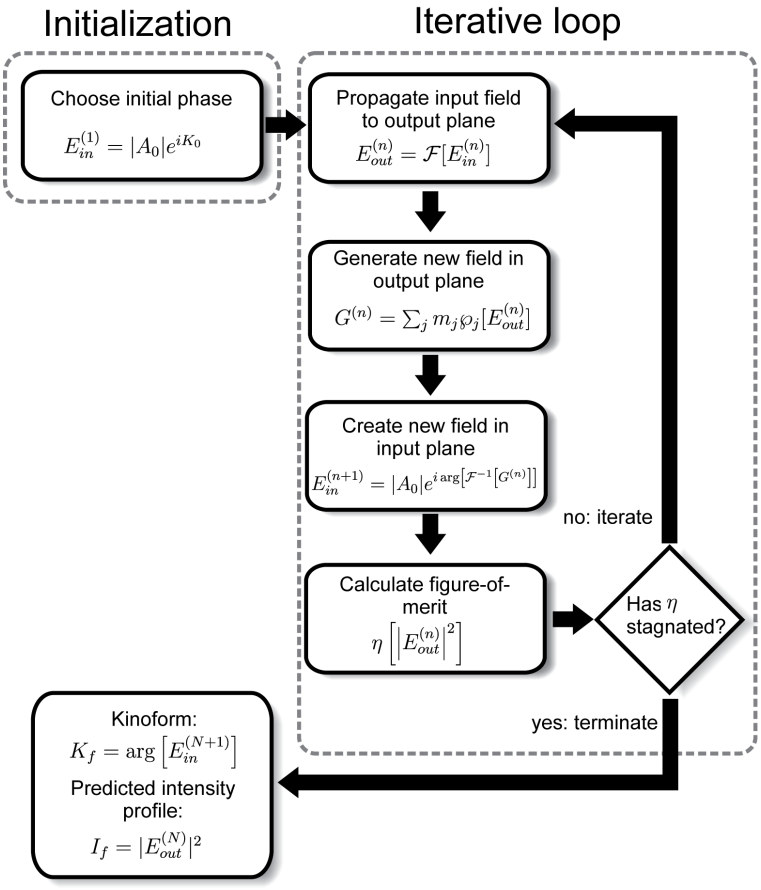

Figure 4.2 Block diagram of an IFTA.

target profile $\sum I_0$ (which is only non-zero in the SR) and the total power in the output plane $m\sum_{SR}\left|E_{out}^{(n)}\right|^2+(1-m)\sum_{NR}\left|E_{out}^{(n)}\right|^2$ remain constant.

The signal region is chosen to overlap with the area in which light will interact with atoms; the remainder of the output plane is the noise region. The effect of dividing the output plane into subsets is to cause the algorithm to converge very closely to the target profile within the signal region, while behaving in a less controlled manner in the noise region. Utilizing the amplitude freedom in the noise region allows for increased accuracy in matching I_0 in the signal region, while decreasing the efficiency of the CGH. The MRAF algorithm is equivalent to a variable strength projection [177] or regularized algorithm [17] with a specific trajectory for the variable mixing parameter that has not been previously demonstrated. The MRAF algorithm is also similar to the algorithms used in [170] and [178]—in which amplitude freedom was first introduced to IFTAs—but with a fixed m.

In Section 4.2.4, I compare the performance of the MRAF algorithm with the GS and AA algorithms. The GS algorithm, in which $G^{(n)}=\sqrt{I_0}e^{i\arg\left[E_{out}^{(n)}\right]}$, permits only phase freedom in the output plane. In the AA algorithm, amplitude freedom is introduced uniformly into the output plane: $G^{(n)}=\left\{m\sqrt{I_0}+(1-m)E_{out}^{(n)}\right\}e^{i\arg\left[E_{out}^{(n)}\right]}$.

4.2.3 Initial Phase

As in any optimization scheme, an initial guess that produces a result close to the target improves the convergence rate and reduces the risk of stagnation into a local optimization minimum. Because IFTAs are used when the solution to the CGH problem is unknown, choosing an initial phase profile K_0 to reproduce complex features in I_0 is not possible. Therefore, we wish to find a K_0 as our starting point for which most of the power in the output plane roughly overlaps with the envelope of I_0. The distribution K_0 must also be chosen so that $E_{out}^{(1)}$ does not contain any undesired optical vortices—points characterized by a phase singularity and zero intensity—since an IFTA is not able to eliminate vortices present in the output plane [17, 152, 179, 180]. A further constraint is that only certain choices for K_0 can prevent an IFTA from *producing* optical vortices in the output plane at each iteration [17, 179, 180]. The optical field in an IFTA is discretized and the Fourier transforms are calculated using FFTs. In order for the FFT to fully resolve the output plane and to reproduce the aperture of the physical device used to implement the CGH, the matrix representing the optical field must be enlarged (i.e., "padded") beyond the size of the CGH by adding a zero-intensity region [181]. The truncation of the input plane field caused by padding leads IFTAs to create optical vortices in the output plane; this behavior is not completely understood [179].

We find that a quadratic phase distribution for K_0 combined with linear and conical gradients does not introduce optical vortices for the MRAF algorithm, even through the input field is truncated in each iteration of the IFTA. Quadratic phase distributions, the equivalent of a thin lens, were first discussed as a solution to the vortex problem in the

context of variants of the GS algorithm [179] (we note that phase-unwrapping techniques have also proven useful in this context [182]). A quadratic phase profile, given by $K_0(x,y) = 4R\left[\alpha x^2 + (1-\alpha)\,y^2\right]$ (R is the curvature and $\alpha/(1-\alpha)$ is the aspect ratio) changes the size of the envelope of the intensity profile in the output plane. A linear gradient phase profile $K_0(x,y) = B\left[x\cos(\mu) + y\sin(\mu)\right]$, where B is the strength of the gradient and μ is an angle, shifts the centroid of the intensity profile in the output plane. A conical phase gradient $K_0(x,y) = Br$ creates a ring in the output plane, where $r = \sqrt{x^2+y^2}$.

For the work described here, quadratic phase profiles are used to roughly match the size of the field in the output plane to the size of the target profile. We find that the results of the algorithm are not strongly affected by small changes in R. Linear gradients are used to match targets that are shifted from the center of the output plane to avoid complications caused by undiffracted light resulting from the finite efficiency of a physically-implemented CGH. Conical gradients are used to match target profiles which have a ring-like structure. Quadratic, linear, and conical phase distributions are added together modulo 2π to combine the effects of each. We find that this combination of initial phase distributions has enough flexibility to obtain sufficient overlap of $|E_{out}^{(1)}|^2$ with I_0 to achieve a few percent error in I_f within tens of iterations.

4.2.4 MRAF Algorithm Results

We characterize the performance of the MRAF algorithm using the six target intensity profiles shown in Figure 4.3, chosen because of their potential application to ultra-cold atom experiments. Target (a) consists of two Gaussian beams connected by a ring with a Gaussian cross-section, which could be used to study ultra-cold atom gases in multiply-connected geometries (which has been experimentally realized [50]). A 3-pointed star-shaped intensity profile is shown in Figure 4.3(b); a similar profile was recently used to induce spontaneous vortex generation in an atomic Bose-Einstein condensate (BEC) [183]. Figure 4.3(c) shows a uniform square intensity profile, which may be used as an optical lattice beam in experiments for which it is desirable to remove effects generated by the external confinement resulting from a Gaussian beam profile [66, 69]. Target (d) is a complex intensity profile that could be employed to realize an "atomtronic" logical OR gate [48]. An intensity profile that could be used to trap a BEC in a superconducting quantum interference device (SQUID) geometry is shown in Figure 4.3(e). Finally, a BEC confined in a dipole trap created using target profile (f) would be equivalent to a thin superconducting wire connected between bulk superconductors [135].

The parameters defining the geometry of each target profile are given in the caption to Figure 4.3. To describe these test patterns and in the rest of this chapter, we use pixels (px) to measure distances in the input and output planes. Each pixel in the input plane represents a point at which the input field is discretized. The physical size of a pixel in the input plane is the physical size, d, of the matrix used to represent the input field divided by

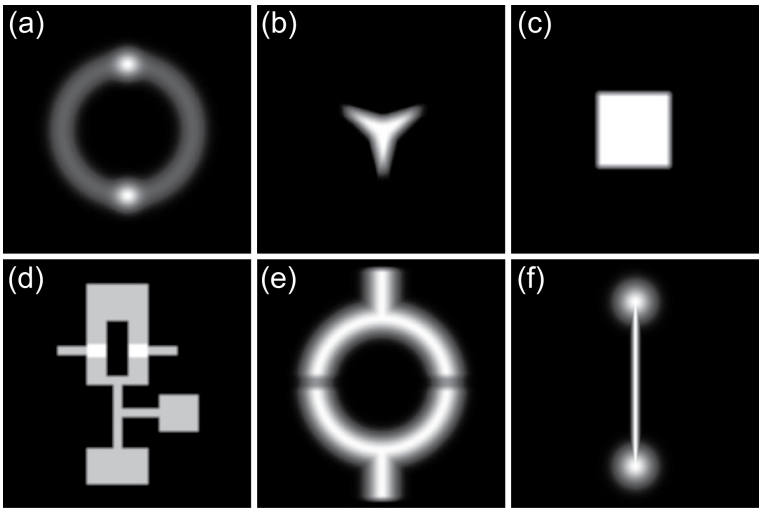

Figure 4.3 Target intensity profiles I_0 used to characterize the performance of the MRAF algorithm. The field-of-view for images (a), (b), (c), and (e) is a 200×200 pixel and for (d) and (f) is a 400×400 pixel subset of the output plane centered on I_0. The grayscale represents intensity, with black corresponding to the regions of zero intensity. The radius of the ring in (a) is 53 pixels and the waist for each Gaussian beam and the Gaussian cross-section of the ring is 14 pixels. The maximum intensity of the Gaussian beams is three times that of the ring. Each "tip" of the star-shaped pattern in (b) is 20 pixels from the center of the star; the two lines that intersect to form each "tip" subtend a 28° angle. To create the profile shown in (b), a uniform intensity profile with a star shape was convolved with a Gaussian with a 5 pixel waist. The profile in (c) was created by convolving a 58 pixel on edge square profile with a 3 pixel averaging filter. The overall dimensions of the profile in (d) are 288 pixels wide and 325 pixels high, and the intensity in the "base" regions is increased by 33%. The Gaussian ring in (e) has a 53 pixel radius and a 7 pixel r.m.s. width. The intensity in the 10 pixel wide gaps in (e) is suppressed by a factor of 2, and the "leads" in (e) are 185 pixels from end-to-end. The 264 pixel wide Gaussian "wire" in (f) has a 3.5 pixel r.m.s. width, and the Gaussian reservoirs in (f) have a 17.6 pixels r.m.s. radius. The center of each profile is displaced from the center of the output plane by (b) 37 pixels and (c) 63 pixels; the profiles in (a), (d), (e), and (f) are centered on the output plane.

the number of pixels. The pixel size in the output plane is $f\lambda/d$, where f is the focal length of the focusing objective and λ is the wavelength of the light. For the results given in this section, the input field is discretized on a 768×768 pixel array and the phase of the field in the input plane is discretized in 256 levels (for each iteration of the IFTA) (see Section 4.3). The input field array is padded with zero intensity points in each iteration of the IFTA to create a 1536×1536 pixel matrix. We observe no significant change in the algorithm results if the array is enlarged beyond 1536×1536 pixels (consistent with the Nyquist-Shannon sampling theorem). We implement IFTAs in MATLAB, and we use a Gaussian input field $A_0 \propto e^{-r^2/w_0^2}$ with a 565 pixel waist w_0.

The initial phase profile chosen for each target intensity profile is shown in the top half of Figure 4.4. A conical phase profile is used in K_0 for (a) and (e) to create a ring structure. Target profiles (b) and (c) are shifted from the center of the output field, and therefore linear gradients are used in K_0 to displace the intensity in $E_{out}^{(1)}$ accordingly. Quadratic phase profiles are used in each K_0 to match the approximate area covered by I_0 in the output plane. The intensity profile in the output plane for the first iteration of the IFTA is shown in the bottom half of Figure 4.4. The initial phase profiles in Figure 4.4 were optimized manually; the predicted intensity profile is not affected by small changes in K_0.

A qualitative comparison between the predicted intensity profiles for the MRAF, GS, and AA algorithms is shown in Figure 4.5. We find that the small-length-scale intensity fluctuations apparent in Figure 4.5 are a generic feature of using the GS and AA algorithms to generate arbitrary intensity profiles. We did not determine if any of these fluctuations are optical vortices, which can be removed from I_f under limited circumstances by changing K_f (and at the cost of greatly increased computational complexity) [172, 179, 180, 184].

To quantitatively characterize the performance of the MRAF algorithm and compare with the GS and AA algorithms, we introduce measures of accuracy and roughness. The accuracy metric is the root-mean-square (r.m.s.) fractional error from the target averaged across a subset, the measure region (MR), of the output plane:

$$\eta = \sqrt{\frac{1}{N_{MR}} \sum_{(x',y') \in MR} \frac{\left[\widetilde{I}_f(x',y') - \widetilde{I}_0(x',y')\right]^2}{\widetilde{I}_0(x',y')^2}}. \tag{4.2}$$

The measure region is a subset of the signal region and is chosen to exclude the zero-intensity pixels in I_0. The intensity profiles $\widetilde{I}_f = I_f / \sum_{(x',y') \in MR} I_f$ and $\widetilde{I}_0 = I_0 / \sum_{(x',y') \in MR} I_0$ are normalized to have the same power in the measure region, and $N_{MR} = \sum_{(x',y') \in MR} 1$ is the number of pixels in the measure region. The error η is also used as the convergence parameter and the optimization parameter for the MRAF and AA algorithms.

The roughness measure

$$\rho = \sum_{(x',y') \in MR} \left\{ H\left[\widetilde{I}_f(x',y') - \widetilde{I}_0(x',y')\right] \right\}^2 / N_{MR} \tag{4.3}$$

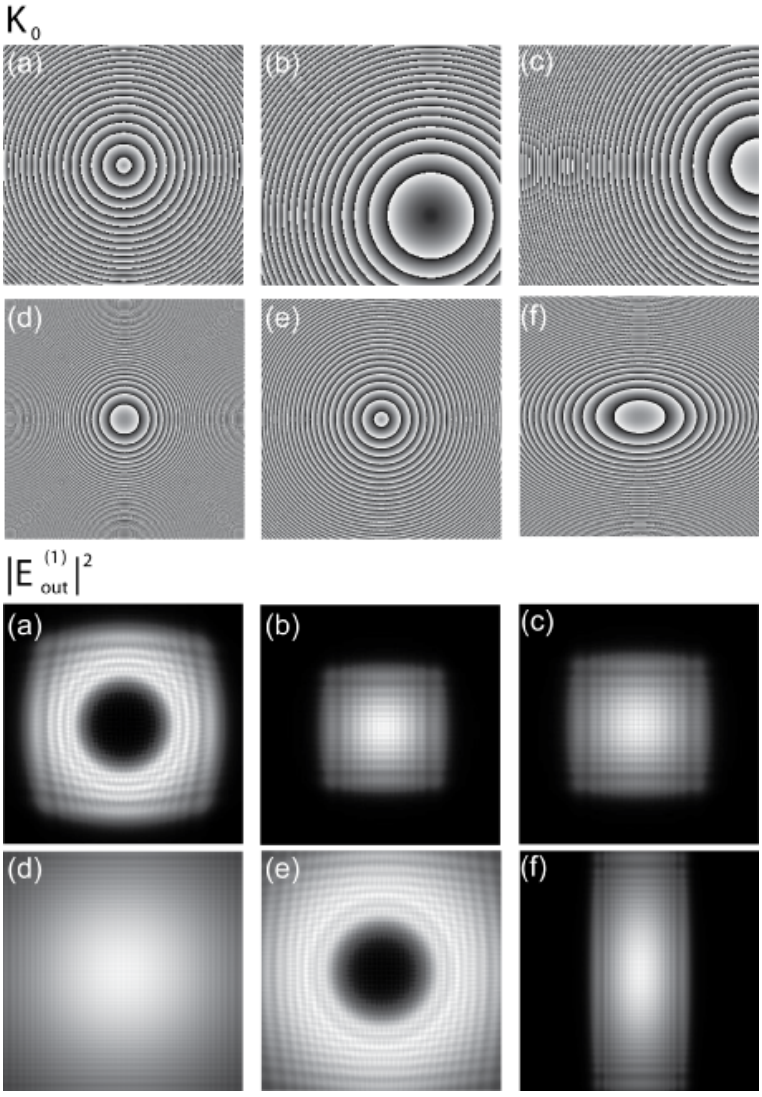

Figure 4.4 Initial phase profiles K_0 (top row) and predicted initial intensity profiles $|E_{out}^{(1)}|^2$ (bottom row) chosen for the target intensity profiles in Figure 4.3. The phase profiles are 768×768 pixels and are shown in grayscale modulo 2π; white corresponds to a 2π phase. Conical phase profiles with $B = 117\ mrad/px$ are employed in (a) and (e). Linear gradients of 136 $mrad/px$ and 260 $mrad/px$ with $\mu = 0$ and $\pi/4$ are used for (b) and (c), respectively. Quadratic phase profiles with $R = 0.31\ mrad/px^2$, $R = 0.3\ mrad/px^2$, $R = 0.34\ mrad/px^2$, $R = 1.4\ mrad/px^2$, $R = 0.5\ mrad/px^2$, and $R = 1.6\ mrad/px^2$;$\alpha = 0.29$ are applied in (a), (b),(c), (d), (e), and (f) respectively.

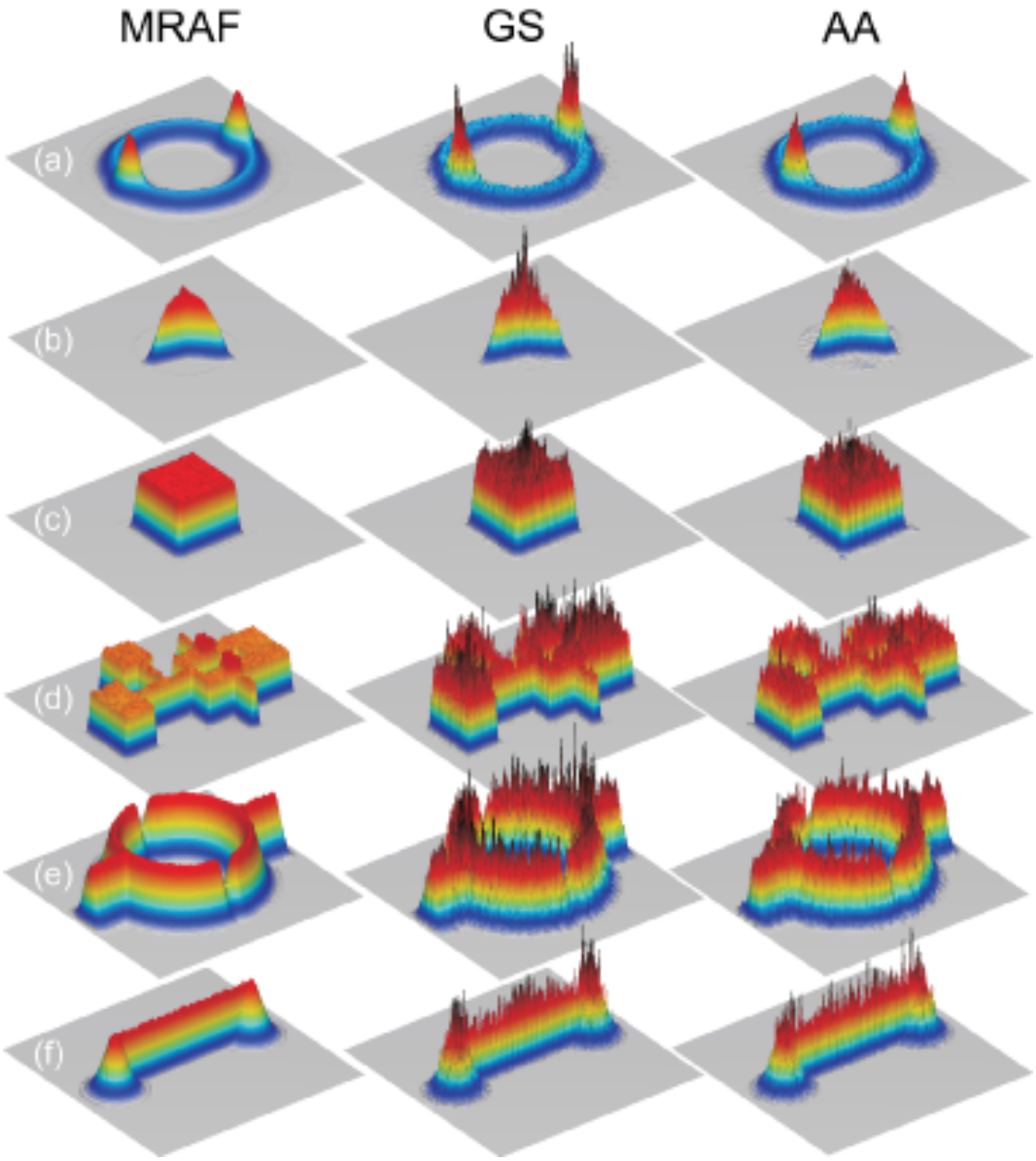

Figure 4.5 Intensity profiles I_f for the MRAF, GS, and AA (left, middle, right) algorithms for the test target profiles. Only the intensity in the signal region is shown, and the profiles are scaled so that the total power in the signal region is the same for each.

is the average of the square of the mean curvature H of the difference between the predicted and target intensity profiles in the measure region. The roughness ρ is proportional to the Willmore bending energy for the surface $\widetilde{I}_0 - \widetilde{I}_f$ [185]. A unique measure of roughness for a two-dimensional manifold, such as I_f, does not exist. We choose ρ as defined in Eq. 4.3 as a metric because it is intuitively appealing as an energy that is strongly weighted by small-length scale deviations of I_f from I_0 (the Willmore bending energy of a spherical surface is proportional to the square of the inverse of the radius of curvature). The measure ρ also quantitatively reproduces qualitative features we observe in the predicted intensity profiles. For each predicted intensity profile we also calculate the efficiency of the CGH for diffracting light into signal region. The efficiency $\xi = \sum_{(x',y')\in SR} \widetilde{I}_f / \sum_{(x',y')} \widetilde{I}_f$ is defined as the ratio of the power in the signal region to the total power in the output plane. The parameters η and ρ are both efficiency-independent measures of the deviation of I_f from I_0: η and ρ are zero if $\widetilde{I}_f = \widetilde{I}_0$.

The result of using the MRAF algorithm to create a CGH based on the test target profiles is shown in Figure 4.6. Both the final kinoforms to which the the initial phase profiles in Figure 4.4 converged and the predicted intensity profiles are shown in the figure. The mixing parameters and the conical and quadratic phase profiles used in K_0 were optimized by determining the minimum value for η calculated for a wide range of m, B, and R. The signal region used in the MRAF algorithm is outlined in red for each target profile in Figure 4.6. The MRAF algorithm converged in less than 100 iterations for each of these target profiles.

Table 1 shows the accuracy, roughness, and efficiency calculated for each predicted intensity profiles in Figure 4.6 and the equivalent results generated by the GS and AA algorithms. The accuracy and roughness are determined using the measure region outlined in yellow in Figure 4.6. The MRAF algorithm on average shows a factor of 9 improvement in accuracy and a factor of 190 improvement in roughness compared with the GS and AA algorithms; the average error for each target for the MRAF algorithm is at the few percent level. The MRAF algorithm produces comparatively smooth intensity profiles even though ρ is not used to optimize the mixing parameters or as a convergence criteria for the IFTA (see Figure 4.7).

The error η, an average across the measure region, can be small although large errors exist at points in the output plane. To show that the MRAF algorithm achieves accuracy everywhere in the signal region, a histogram of the error evaluated at each output plane point $(\sqrt{\widetilde{I}_f^{\,2} - \widetilde{I}_0^{\,2}}/\widetilde{I}_0)$ in the signal region for the result in Figure 4.6(a) is shown in Figure 4.8; 95% of the pixels in the signal region have less than a 3% error. For the purposes of comparison, the result of using the GS and AA algorithms to calculate a CGH for target (a) is also shown in Figure 4.6. The MRAF algorithm improves greatly on the GS and AA algorithms, both of which have at least 45% of the pixels in the signal region with errors greater than 10%.

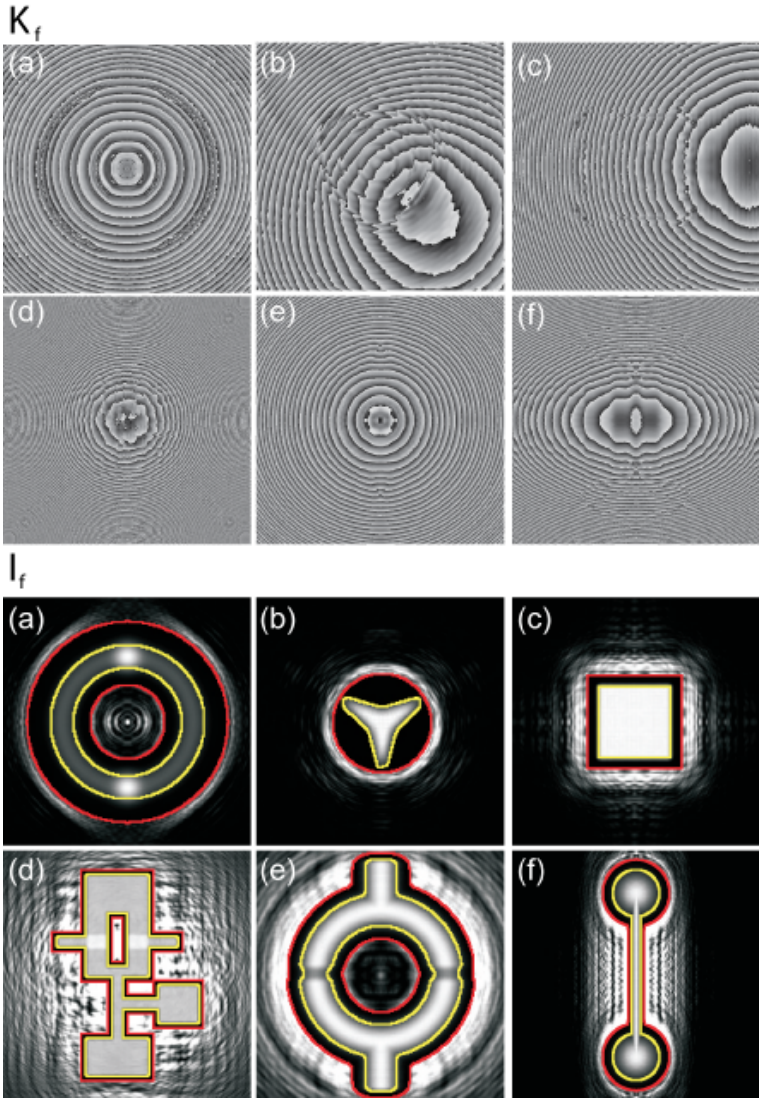

Figure 4.6 Final kinoforms K_f (top row) and predicted intensity profiles I_f (bottom row) produced by the MRAF algorithm for targets (a), (b), and (c). The mixing parameters used to generate these results are: (a) 0.40, (b) 0.35, (c) 0.40, (d) 0.30, (e) 0.35, and (f) 0.30. The signal region (red) for (a) is an annulus with with inner and outer radii 25 and 81 pixels; in (b) is a circle with a 40 pixel radius; for (c) is a square 75 pixels on edge; in (d) is a region 10 pixels from the edge of the target profile; for (e) a region 10 pixels away from where the intensity is 10% of the maximum intensity; and for (f) consists of two 53 pixel radius circles separated by 264 pixels and a connective region 25 pixels wide. The measure region (yellow) in (a) is an annulus with inner and outer radii 44 and 62 pixels; in (b), (e), and (f) is defined by a region in which the intensity of the target is greater than 10% of the maximum target intensity; in (c) is a square 57 pixels on edge; and for (d) is the edge of the target profile.

Algorithm	Error η					
	Ring (a)	Star (b)	Square (c)	OR gate (d)	SQUID (e)	thin wire (f)
GS	0.21	0.30	0.23	0.34	0.36	0.36
AA	0.13	0.19	0.19	0.23	0.21	0.23
MRAF	0.017	0.027	0.015	0.039	0.018	0.029
	Roughness ρ					
GS	220	5600	460	13	160	110
AA	64	2200	400	5.3	47	40
MRAF	0.65	20	1.1	0.044	0.18	0.19
	Efficiency ξ					
GS	0.99	0.99	0.99	0.96	0.97	0.97
AA	0.90	0.83	0.88	0.79	0.71	0.59
MRAF	0.45	0.29	0.45	0.18	0.30	0.19

Table 4.1 Table comparing the performance of the MRAF to the GS and AA algorithms. The mixing parameters used for the AA algorithm are (a) 1.9, (b) 2.0, (c) 1.9, (d) 2.0, (e) 2.2, and (f) 2.5. The GS and AA algorithms converged in 100 iterations for the results in this table.

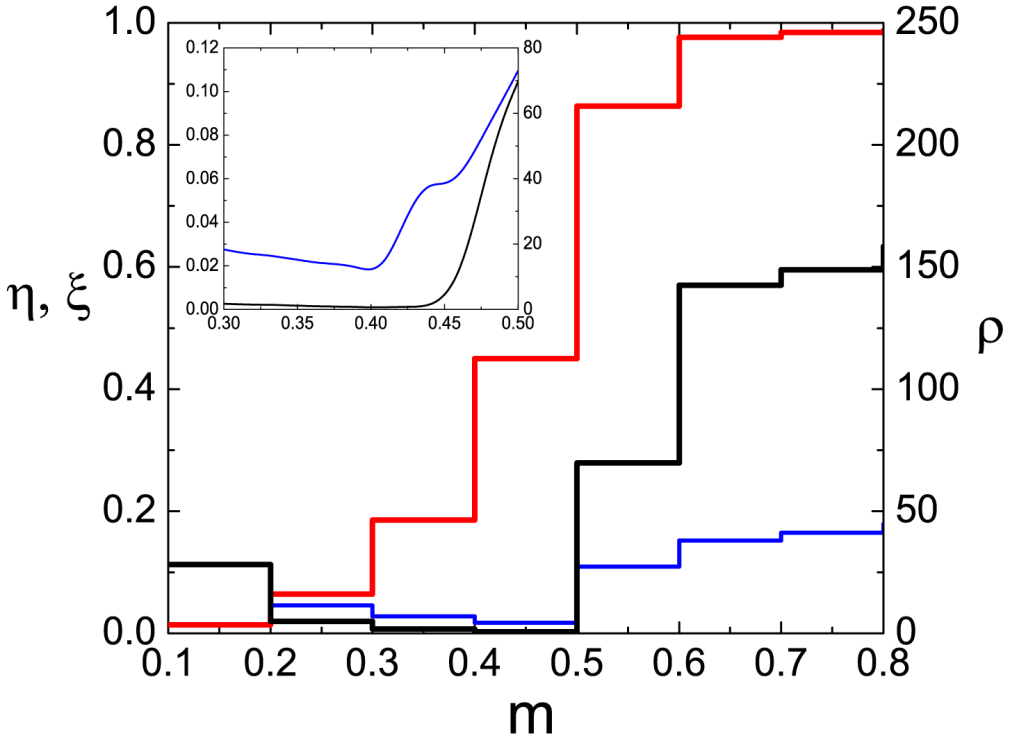

Figure 4.7 Variation of measures characterizing the MRAF algorithm performance as the mixing parameter m is varied. The efficiency ξ (red), roughness ρ (black), and error η (blue) are shown for target (a) for different values of the mixing parameter m. The inset shows detail around the globally-optimized value of m. The mixing parameter that minimizes η approximately coincides with an minimum in roughness ρ for the MRAF algorithm.

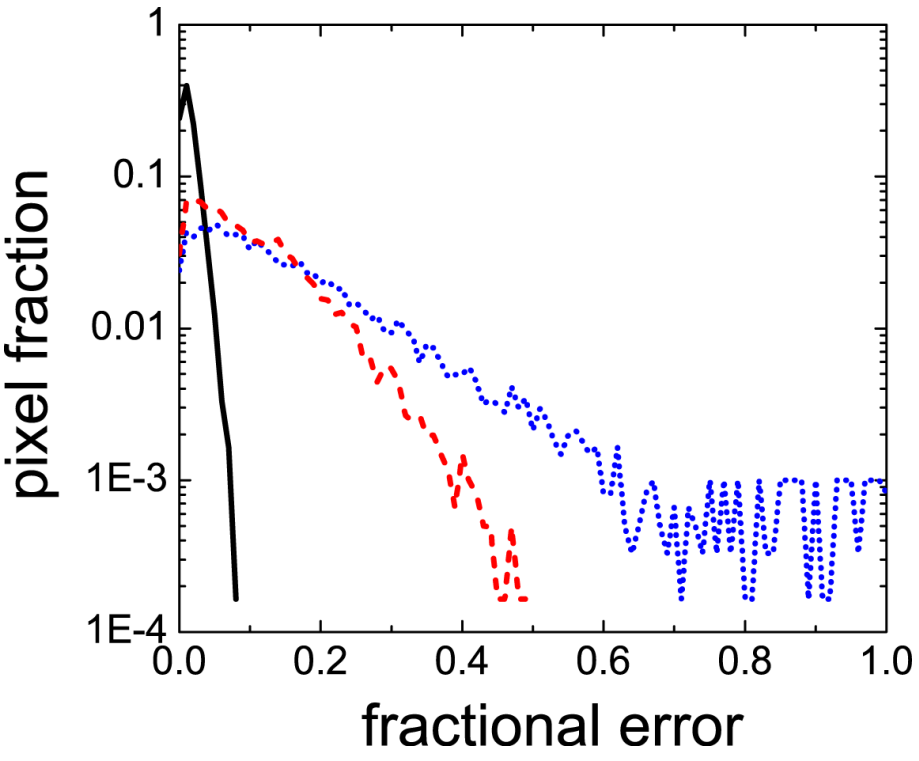

Figure 4.8 Histogram of the fractional error at each pixel evaluated for I_f for the MRAF algorithm used on target (a). The fraction of pixels in the signal region are binned with respect to the fractional error $\sqrt{\widetilde{I_f}^2 - \widetilde{I_0}^2}/\widetilde{I_0}$. The width of each bin is equivalent to a 1% fractional error. The solid black, blue dotted, and red dashed lines are the result for the MRAF, GS, and AA algorithms, respectively.

For the targets used here, the MRAF algorithm has approximately a factor of 2–3 lower efficiency compared with the GS and AA algorithms. While the MRAF algorithm does not lead to efficiencies as high as the GS and AA algorithms, it does not perform so poorly that the efficiency advantage of using a phase-only CGH is lost. For example, the authors of [183] created a profile similar to (b) by propagating a Gaussian beam through an intensity mask and imaging the result onto a BEC. The efficiency of that mask in transmitting light was 3%, compared with $\approx 29\%$ for a CGH created using the MRAF algorithm.

In conclusion, I have discussed the realization of a new IFTA for designing CGHs that can be used to create arbitrarily-shaped, two-dimensional optical dipole traps for ultracold atom experiments. The MRAF algorithm has relatively low computational complexity and converges rapidly—within tens of iterations. For six test target profiles, the predicted output of a CGH designed using the MRAF algorithm is comparatively smooth and has errors at the percent level.

4.2.5 Improving the Initial Phase

Although we accomplished our goal of creating holograms that can trap cold atoms [50], there is still room to improve the fraction of the light that is wasted (the efficiency) when producing these traps. The initial phase K_0 is crucial to solving this problem because the amount of light that falls inside the signal window after the first iteration largely determines the efficiency of the algorithm. The technique of geometric transformations, used previously for beam shaping, can be used to provide this initial phase in a deterministic way [179, 186–188]. Based on these methods, we propose a way to automate the determination of the initial phase K_0 for the MRAF algorithm. Note that the stability of this method against introducing vortices during the IFTA remains to be investigated.

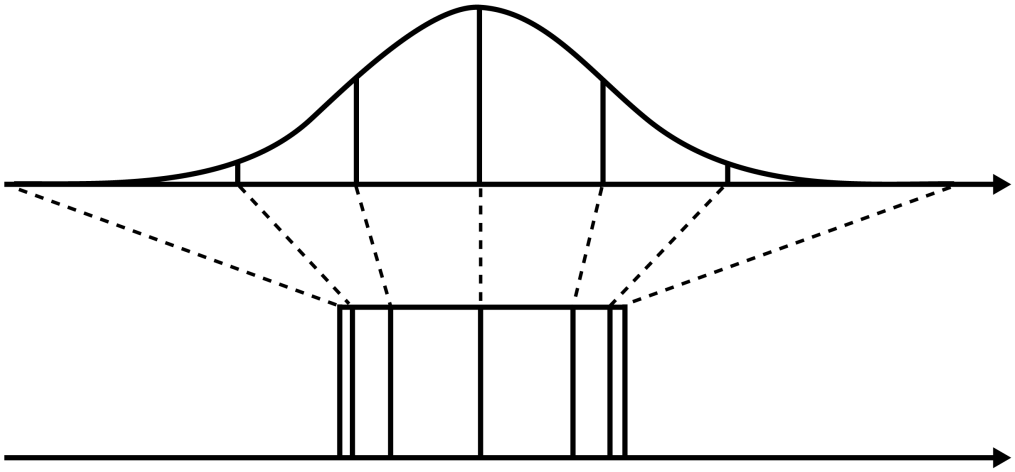

Figure 4.9 A method to map power from one arbitrary 1D function $f_1(x)$ to another $f_2(x)$ [179]. The upper function $f(x)$ is divided into a series of equally spaced blocks. The blocks labeled $\{b_i\}$ span $x = \{x_{i-1}, x_i\}$. The lower function is broken up into non-equally spaced blocks $\{c_i\}$ such that the power in $P(b_i) = P(c_i)$ where $P(b_i) = \int_{x_{i-1}}^{xi} f(x)dx$. The set points $\{x_i'\}$ is chosen by, starting from the end of the previous block making c_i wider until the condition $P(b_i) = P(c_i)$ is satisfied. If we allow $n \to \infty$, we can define a continuous function h from $\mathbb{R} \to \mathbb{R}$. This mapping can be converted into a kinoform that converts a 1D light field with intensity $f_1(x)$ into a light field at the focus $f_2(x)$ [187].

To understand how the 2D transformations that would produce K_0 would work, it is useful to first consider the 1D analytical method of geometrical transformations [179]. The goal is to find a coordinate transformation h which transfers power from the input intensity $I_1(x) = |f_1(x)|^2$ to the appropriate position in the output intensity $I_2(x) = |f_2(x)|^2$ (see figure 4.9). The condition that the I_1 is mapped by $h(x)$ to I_2 can be expressed mathematically as,

$$|f_1(x)|^2 dx = |f_1(h)|^2 dh. \tag{4.4}$$

Integrating the two infinitesimal pieces in 1D starting from $-\infty$ gives

$$\int_{-\infty}^{x} |f_1(t)|^2 dt = \int_{-\infty}^{h(x)} |f_2(t)|^2 dt. \tag{4.5}$$

Thus we find the transformation

$$h(x) = F_2^{-1}[F_1(x)], \tag{4.6}$$

where the integrals $F_k(x) = \int_{-\infty}^{x} |f_k(t)|^2 dt$ (k = 1,2) exist and $F_2(x)$ is invertible.

From this mapping, we can produce a kinoform $\phi(x)$ by the method of stationary phases [187]

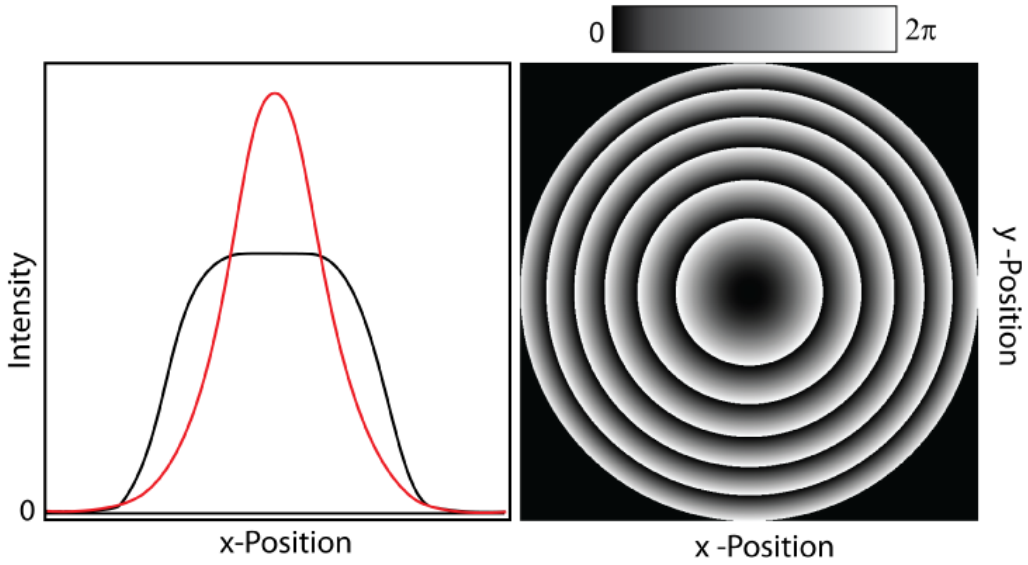

Figure 4.10 A cross section of the predicted intensity at the output plane of a Gaussian with the analytically applied kinoform. A kinoform computed analytically that maps a 2D Gaussian (red) to a 6^{th} order super-Gaussian (black). The colorscale on the right shows the phase modulation between 0 and 2π

$$\phi(x) = 2\pi \int_{-\infty}^{x} h(t)dt. \tag{4.7}$$

The method of stationary phases used to produce ϕ from the mapping h assumes the input function (e.g. f_1) is composed of small spatial frequencies. Thus to take advantage of these analytical transformations, the size of the input Gaussian beam should be made smaller than the face of the phase-modulation device to avoid clipping and the resulting high spatial frequencies. Because of the fringes that would result from any clipping, this method alone is not sufficient to produce optical potentials for ultra-cold atoms.

In our paper, the functions K_0 were composed of linear and quadratic phases only. Using the technique in Ref [179], we can select K_0 from a much larger set of 2D separable functions. These functions have the form $g_i(x, y) = X_i(x)Y_i(y)$, where g_1 and g_2 are the input and output intensities. The kinoform that transforms $g_1 \to g_2$ is $\phi_x + \phi_y$, where ϕ_x transforms $X_1 \to X_2$ and ϕ_y transforms $Y_1 \to Y_2$. This technique has the advantage that separable K_0 can be calculated simply; for instance, with a few lines of code in Mathematica. An example of such a separable 1D function is the high-order super-Gaussian distribution shown in Figure 4.10. The Gaussian function (red) is converted into a 6^{th} order super-Gaussian (black) by the analytically calculated kinoform on the right.

While the 1D mapping technique of Aagedal et al. [179] provided an analytical method for producing separable holograms, some holograms are not well-approximated by a separable function (see, for instance, Figure 4.3). A mesh-based mapping algorithm can create

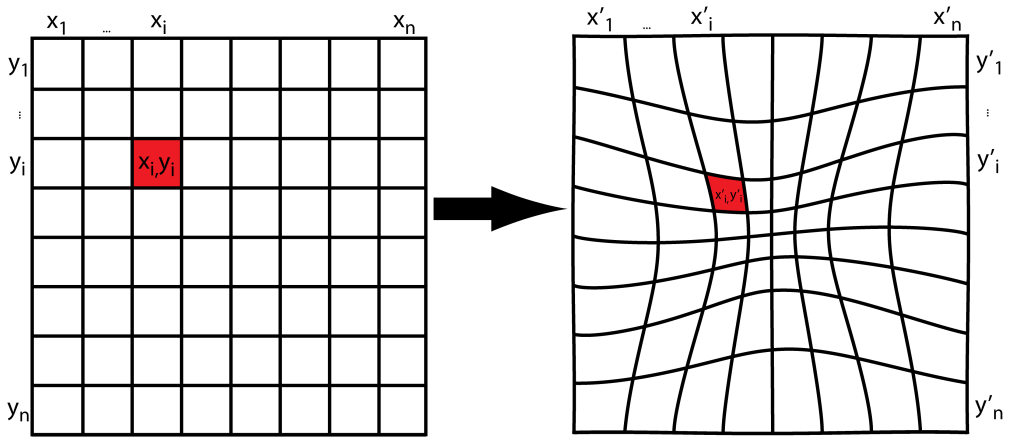

Figure 4.11 The regular mesh on the right breaks an input beam up into cells labeled $\{x_i, y_i\}$. This lattice is distorted by an algorithm that maps an input intensity distribution to the desired target distribution [188]. The mapping changes both the position and size of the corresponding cell in the output mesh denoted by $\{x'_i, y'_i\}$; this is shown by the distortion and displacement of the red cell. This mapping is converted into a kinoform by the method of stationary phases [187].

initial phases K_0 that form initial intensity distributions I_0 from the larger set of non-separable functions without phase singularities [188]. This class of functions contain no topological defects which would cause the algorithm to stagnate, making them an excellent starting point the MRAF algorithm. The idea behind these mesh algorithm can be see in Figure 4.11. The initial light field is divided up into many different regions $\{x_i, y_i\}$. This mesh is distorted by an algorithm which maps power from the input plane to the output plane to find a 2D mapping h [188]. Using the same method as in 1D, this 2D mapping function is converted into a kinoform [187].

4.3 Experimentally Producing Holograms

Now that an algorithm to produce holograms exists, the challenge for realizing arbitrary, two-dimensional dipole traps for atoms is in experimentally implementing a CGH. We attempted to use an SLM realize the kinoforms produced by the MRAF algorithm. However, the kinoforms reproduced by this SLM were not suitable for ultra-cold atoms because of large inaccuracy in the phase calibration. This section will discuss how these SLMs work, the methods we used to measure their performance, and problems we encountered. I will also demonstrate a method for producing static holograms on emulsion plates that could be used as an alternative to SLMs.

4.3.1 Spatial Light Modulator

The most common method currently for producing holographic optical traps is the spatial light modulator [150]. This electronically controlled device displays a kinoform by changing the birefringence on an active surface. For polarized light, the spatially varying birefringence produces a position dependent phase shift. For SLMs that use nematic liquid crystals as a birefringent medium, the change in phase $\Delta\phi$ is controlled by the voltage V_I applied to each pixel.

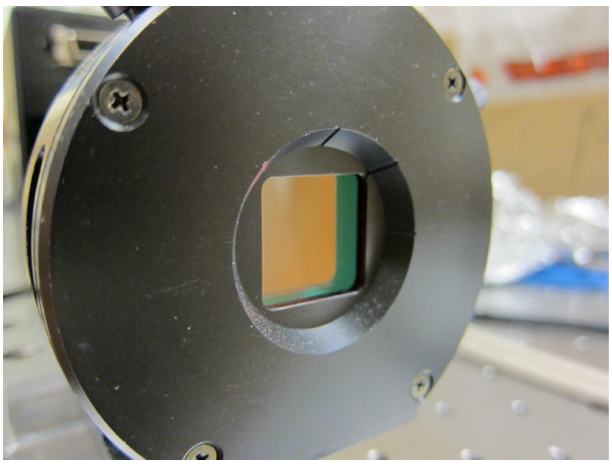

Figure 4.12 The liquid-crystal display on the Hamamatsu X8267 SLM.

The SLM we used was the Hamamatsu X8267. The liquid-crystal surface of this device, shown in Figure 4.12, is broken up into 768×768 pixels, each capable of displaying 256 discrete phase levels. The SLM works using a two-stage mechanism. In the first stage, a laser contained in the body of the SLM passes through an amplitude modulation SLM. This light pattern is then imaged onto the back of the external active surface. The phase $\Delta\phi$ produced by the external liquid crystal face is proportional to the light intensity incident on its internal surface. The kinoform is transmitted from the control computer to the SLM via a driver box which converts an input signal (the green-channel from an RGB monitor output) into a voltage V_I that drives the SLM as shown in Figure 4.13.

This SLM may also be used to modulate the amplitude of the laser rather than the phase. In amplitude modulation mode, the birefringent liquid crystal rotates the polarization of the laser at each pixel based on V_I. Passing the laser beam through an additional polarizer removes the un-rotated light (or vice-versa). For holography, this mode is intrinsically less efficient than phase modulation because at least half of the light is removed from the beam.

For a perfect SLM, the phase $\Delta\phi$ displayed by the SLM would be linearly related to the input from the control computer. However for the Hamamatsu SLM we used, this is not the case — the relationship between $\Delta\phi$ and the input voltage V_I is a non-linear function which must be determined experimentally. To find this function $\Delta\phi = g(V_I)$ we illuminated the SLM with two spots from the same monochromatic laser beam. Using optics to produce the Fourier transform of the light (as shown in Section 4.3.2), we see the interference of the two spots. The imaged interference pattern is fit to a simulated interference pattern to find the relative phase between the two spots. Using this function $\Delta\phi = g(V_I)$, shown in Figure 4.14, we modify the kinoforms we display on the SLM to account for the non-linearities in $g(V_I)$. This process is usually performed to calibrate any SLM (see, for instance, Ref. [189]). However, as explained in Section 4.3.3, this procedure is not sufficient to correct the non-ideal phase response of the SLM we used.

4.3.2 SLM Optics

Aside from the SLM itself, the performance of a CGH is sensitive to the optics which manipulate the light. These optics are divided into three parts: the fiber and telescope which produce the input beam, the relay lenses that produce a hologram after the SLM, and the microscope and CCD that image this hologram (see Figure 4.15). Each of these stages is susceptible to imperfections that can degrade the hologram, or the image we measure.

The first stage takes monochromatic, polarized light and creates a parallel Gaussian beam of the correct size at the SLM active surface. A polarization maintaining optical fiber creates a Gaussian beam with little error in the amplitude or phase as well as linear polarization. A $\lambda/2$ plate rotates this polarization to match the required SLM input polarization for phase-only operation. A telescope then expands the beam to fill the SLM. This telescope

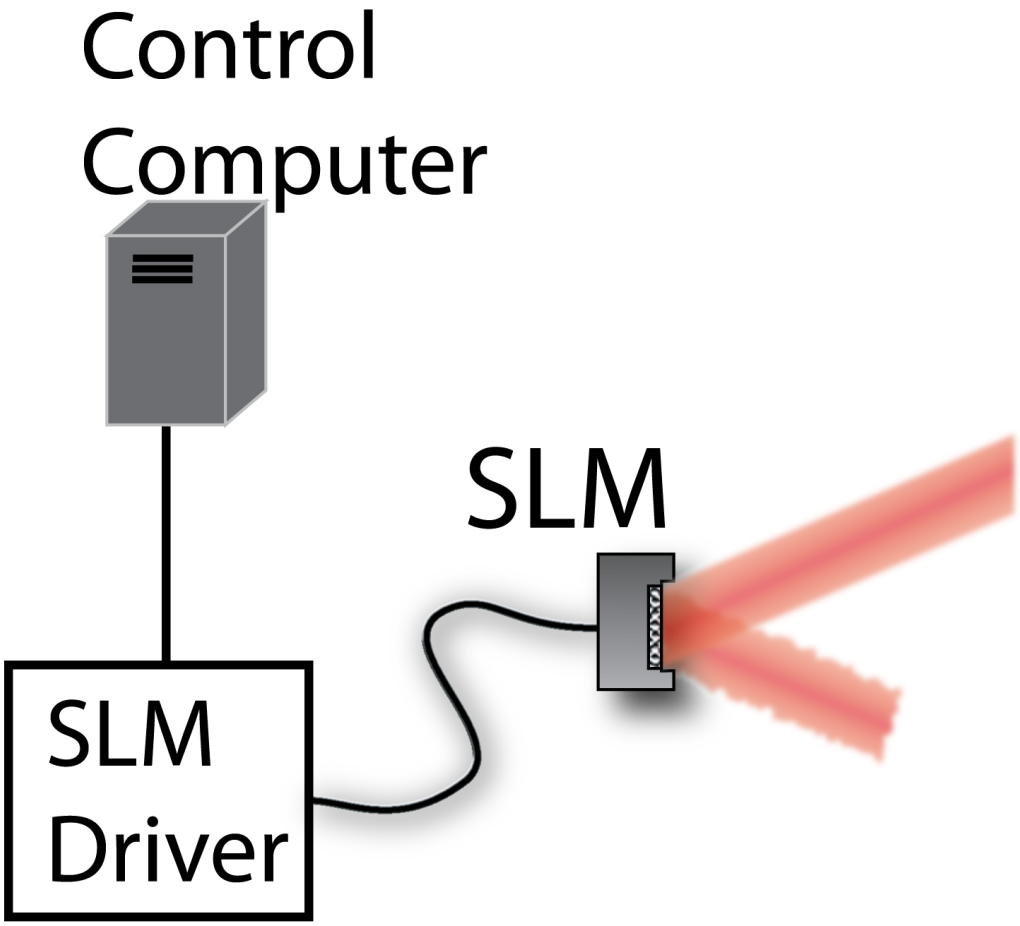

Figure 4.13 A control computer outputs a kinoform which is switched to be shown on either a monitor or an SLM. The SLM driver produces the voltage necessary to fully modulate the phase of the laser (red).

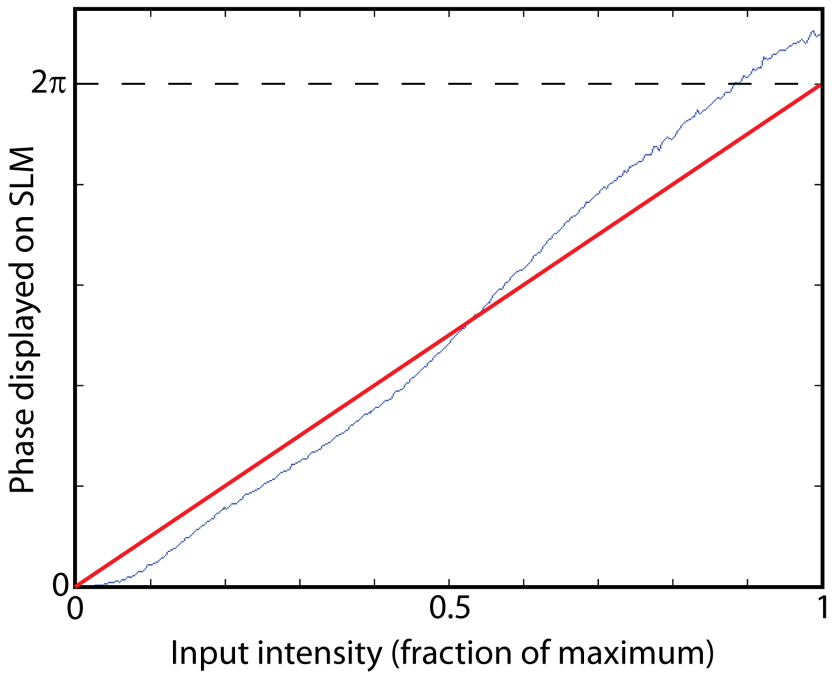

Figure 4.14 The phase calibration of the Hamamatsu SLM. The output phase is not a linear function of the input intensity. The red line shows an ideal phase calibration. The phase calibration is averaged over a small number of pixels. For the SLM we used, the phase calibration varied significantly across the device.

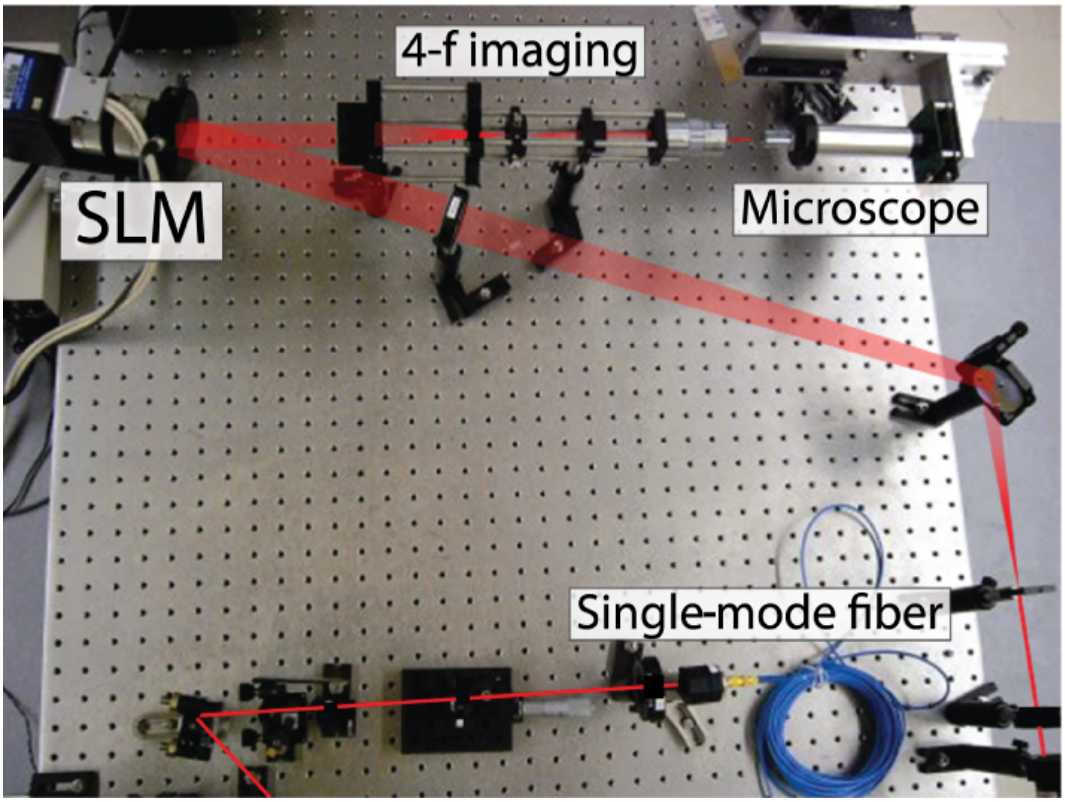

Figure 4.15 The optics used to produce and measure holograms experimentally with the path of the laser superimposed in red. After the light is coupled into a single-mode fiber it is expanded by a telescope so that it fills the face of the SLM. The 4-f relay optics shrink the beam and transfer it onto the Mitutoyo objective lens. This focused light field is imaged by a microscope and CCD.

uses long focal length lenses to allow thinner lenses which reduce aberration. We measure the width of the beam with a razor blade and photodetector. Making multiple measurements after the telescope at different distances allows us to ensure that the beam is parallel. To eliminate optical aberrations like astigmatism and coma the beam is centered on each lens by inserting a "bulls-eye" paper target and looking at the beam with a IR-viewer.

Once the input beam is phase-modulated by the kinoform on the SLM, the light must be focused to produce the optical-trap target intensity pattern. A lens directly after the SLM would accomplish the Fourier transform exactly. However, because the SLM is reflective, it is not possible to place a lens close to the active surface. If a simple lens were placed a distance away light at the focus would deviate from a true Fourier transform [42] and the intensity pattern would not be correct. To get around this problem, we use relay optics that transfer the exact complex amplitude of light at the SLM to the final focusing lens (an objective lens) that creates the hologram. This relay scheme is called "4-f" imaging because it is 4 times the focal length of the lenses in the telescope. For this prototypical 4-f configuration, each of the two lenses is the same focal length forming a 1-1 telescope. The distance to the SLM before and and imaging lens after the telescope is the focal length f. We modify this to reduce the size of the light by a factor of two so it fits without clipping on the focusing lens. In this configuration, the first lens has focal length $f_1 = 150$ mm and the second $f_2 = 75$ mm creating a telescope with magnification is $f_2/f_1 = 1/2$. The distance between the first lens and the SLM is f_1 and the distance from the second lens to the focusing lens is f_2. This final lens, a Mitutuyo infinity compensated, long working distance objective, focuses the beam, forming the target intensity pattern. All of the optics in this stage are especially sensitive to misalignment and are fixed in a Thorlabs cage mount system to maintain precise alignment.

To image the hologram, we built an integrated CCD/microscope. This consisted of building a lens tube which fixed a microscope objective (Optics for Research 20x, 40x, and 60x) 180 mm away from the face of a CCD camera (Optics Xpress MX-7). The entire microscope was mounted to a 3D translation stage. The objective could be switched to change the magnification and resolution of microscope.

4.3.3 SLM Performance

Our SLM was incapable of producing the smooth optical traps the MRAF algorithm predicted. Although SLMs had previously been sufficient to produce simple traps, more complex, smooth traps exposed subtle flaws in the SLM's ability to accurately reproduce the kinoforms. Although this prevented us from using the SLM and holograms to trap atoms, these problems have recently been overcome [50].

We found the SLM was incapable of accurately reproducing kinoforms because the phase calibration varied across the SLM's liquid-crystal display. Different regions on the display, given a certain input voltage, would produce different phase shifts. These variations in the

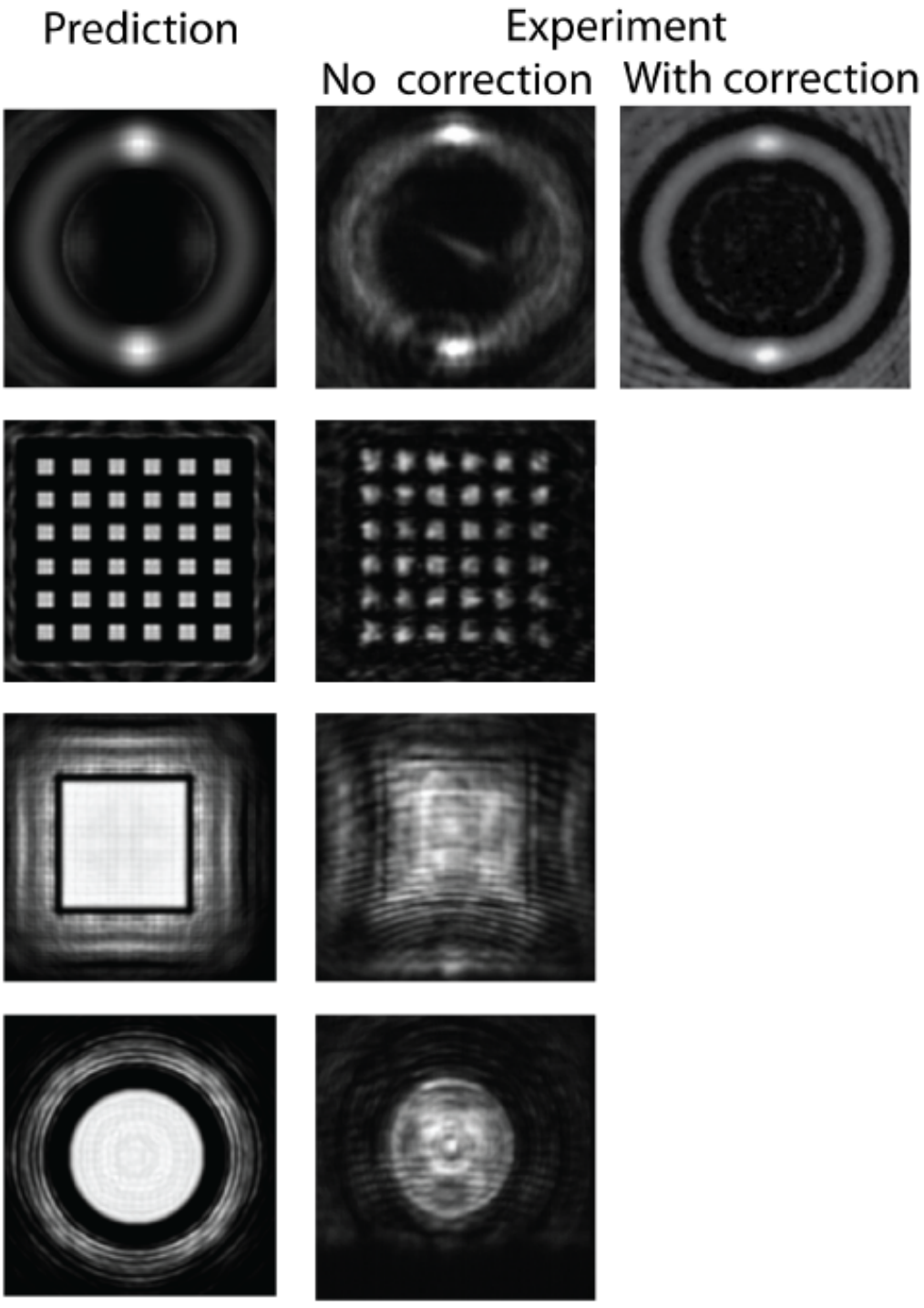

Figure 4.16 The column on the left shows 4 intensity predictions produced by the MRAF algorithm. The center column shows the results of light modulated by these predicted kinoforms with our Hamamatsu SLM. The poor experimental accuracy is a result of phase calibration non-uniformities which have not been corrected. In the final column reproduced from Ref. [50] these non-uniformities have been corrected resulting in an accurate intensity distribution.

phase calibrations resulted in large intensity modulations in the target intensity profiles shown in Figure 4.16. In this figure we compare a few predicted intensity distributions with the best results we could produce with an SLM. For the case of the ring trap there is also a result published earlier this year demonstrating an SLM with the non-uniformities corrected. The manufacturer of our device has since published a paper explaining how these variations can be removed in newer versions of the SLM we used [190].

Based on the results obtained in soft condensed matter experiments for holographic optical traps [150], we had expected much better performance from our SLM. However, the traps we were attempting to produce are different in an important way from those attempted previously. When attempting to trap small objects (like plastic spheres), as is done often in soft condensed matter experiments, the traps are point-like. Spatial variations in the phase calibration of the SLM will only change slightly the position and intensity of these point-like traps. These variations are measured and accounted for iteratively [150]. On the other hand, in the traps created by the MRAF algorithm, light is mapped between two continuous functions. Slight changes in the position of a small portion of the intensity pattern result in large fluctuations in the intensity of the trap at that point, and the smoothness is drastically reduced.

4.3.4 Fixed Plate Holograms

We investigated, in addition to an SLM, silver halide sensitized gelatin (SHSG) holograms [191]. These emulsions, mounted on a glass plate, are exposed and developed like film. For applications which do not require a time-dependent hologram, we hoped that these holographic plates offered a cheaper method for producing arbitrary holographic potentials. Additionally, plate holograms are insensitive to polarization, unlike SLMs that require vertical linear polarization. This section will describe the method we used to expose kinoforms onto holographic plates, how we measured their performance, and the result of these measurements.

The index of refraction of an emulsion hologram changes depending on the intensity of light during an exposure. A film mask with varying transparency controls the amount of light that is incident on the emulsion. The more light the emulsion plate is exposed to, the higher the change in the index of refraction, and thus the higher the phase imprinted on a laser beam by the resulting hologram. We exposed the plate to light from an incandescent bulb with 1 mW/in^2 intensity for 33 seconds. To prevent stray light from hitting the plate, exposure is done in a dark room.

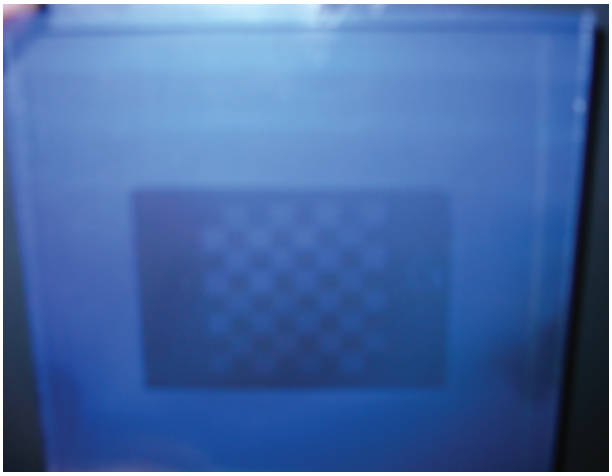

Figure 4.17 A holographic plate photographed to show the kinoform. The checkerboard pattern was used to calibrate the phase difference $\Delta\phi$ produced for a given exposure as shown in Figure 4.18.

The plate is next developed in a three step process. First the plates are soaked in a developing solution for 2 minutes. The developer is composed of the following chemicals: distilled water (750 mL), catechol (20 g), ascorbic acid (10 g), sodium sulfite (10 g), urea (75 g) and water at 68° F (1 L), sodium carbonate (60 g) dissolved in distilled water at 100° F (800 mL) and then mixed into water at 68° F (1 L). After soaking, the developer is washed off in a bath of water for 3 minutes. Next the plates are placed in bleach for 3 minutes, and then washed off in water for 3 minutes. The bleach solution is composed of: distilled water 68° F (750 mL), potassium dichromate (5 g), sodium bisulfate (80 g), water at 68° F (1 L). Care was taken to avoid skin contact with these potentially carcinogenic chemicals. Finally the process is finished with a 3 minute bath of Photo-flo. The Photo-flo solution is: Photo-flo (5 mL), water (995 mL). The developing solution must be used within 24 hours.

To test the performance of these holograms we created a binary checker-board pattern and measured the far-field diffraction from this pattern as a function of exposure intensity as shown in Figure 4.18. The plate was exposed with an intensity based on the transparency of the masking film from 5% to 100%. Half of the squares saw light, while the other half were dark during exposure, creating a checker-board pattern where the "red" squares had ϕ_1 and the "black" squares had ϕ_2. We measured diffraction at the focus of a lens to determine the difference between these two phases. We then matched this to a theoretical calculation that took into account the shape of the input laser field. By comparing the expected $\Delta\phi$ with the experimentally measured value, we were able to create the phase calibration shown in Figure 4.18.

As a result of this investigation into emulsion holograms we found they are a viable alternative to expensive and bulky SLMs. For an experiment that only needs a few types of holographic optical potentials, these may be an effective replacement. In addition to phase

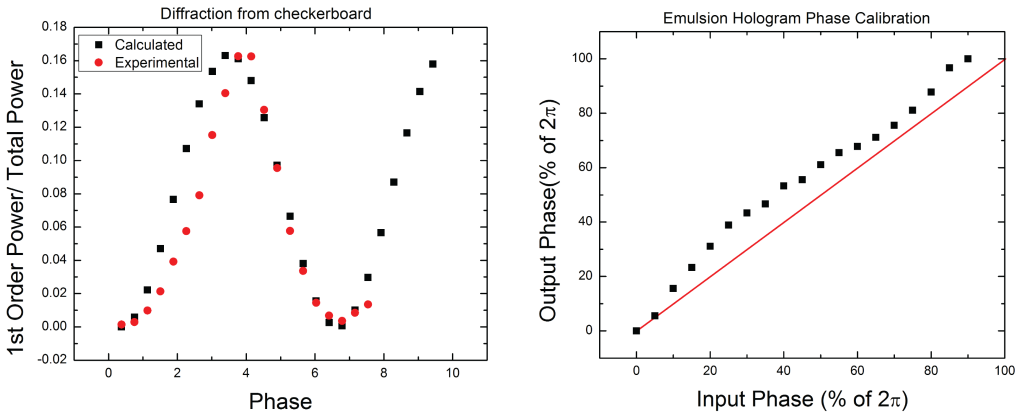

Figure 4.18 On the left, the measured 1^{st} order diffraction peak intensity normalized by total beam power (black) and an ideal simulation of the same value (red). The x-axis of the left plot is the phase difference for the calculated diffraction pattern, which the experimental is scaled to match at 2π. Comparing these two functions, a phase calibration curve was calculated (right). The red line shows where input phase equals output phase.

only holograms, another even easier solution may be amplitude modulation holograms made from metal-masks or films [192]. The wide variety of methods for producing CGHs give the MRAF algorithm relevance beyond just SLMs.

4.4 Conclusion

In this chapter we have introduced a new type of algorithm to calculate computer generated holograms suitable for producing arbitrary 2D optical potentials for ultra-cold atoms. This new algorithm produces potentials that have significantly higher accuracy and smoothness compared to previous algorithms. To make using these algorithms simpler and to decrease the amount of light wasted by the resulting hologram, we also suggested a method to automate the search for the initial phase K_0.

In conjunction with our effort to design an effective CGH algorithm, we also investigated using an SLM to produce optical potentials experimentally. We used a commercially available SLM integrated with optics which produced and imaged the holographic intensity distributions. We were unable to produce sufficiently high-quality optical potentials because the SLM phase calibration was spatially non-uniform. Since our work with SLMs ended, techniques to measure these non-uniformities and correct them have been developed [190].

The invention of our MRAF algorithm cleared one of several hurdles that were preventing CGHs from being used to create arbitrary potentials for atoms. Following the success of our work, the final challenge of producing these potentials experimentally has been overcome [50]. These innovations created a number of new research opportunities in ultra-cold atomic physics which are only beginning to be realized.

Appendix A

Calculating State Diagrams

Consider the calculation we perform numerically to calculate in-trap density profiles and associated N_0/N and S/N. The values of density, condensate fraction, and entropy are interpolated at fixed spacing in r from a phase diagram with fixed spacing in μ, where the i^{th} discrete point is at radius r_i and chemical potential μ_i. The LDA requires that all properties of the lattice are dependent on μ.

Any harmonically trapped lattice with the same maximum chemical potential μ_{max} will have the same S/N and N_0/N at a given temperature. There is only one way to select a parabola that starts at μ_{max} and ends at μ_{min}; $\mu_i = (\mu_{max} - \mu_{min})(1 - i^2/k^2)$, where μ_i is the chemical potential at the i^{th} of k total points. The observable quantity, such as number, is integrated over this set of μ_i as in equation 2.25. Notice that $r_i = i \cdot dr$, where dr is the step size. Equation 2.25 is evaluated at a discrete set of points

$$N = \frac{4dr^3\pi}{(\lambda/2)^3} \sum_i^k \rho(\mu_i) i^2 \tag{A.1}$$

$$N = r_{max}^3 \frac{4\pi}{k^3(\lambda/2)^3} \sum_i^k \rho(\mu_i) i^2 \tag{A.2}$$

$$N = \frac{\omega^3}{\sqrt{m}(\lambda/2)^3} \sqrt{2(\mu_{max} - \mu_{min})} \frac{4\pi}{k^3} \sum_i^k \rho[(\mu_{max} - \mu_{min})(1 - i^2/k^2)] i^2 \tag{A.3}$$

The equation for number, or any other quantity, is separable into a prefactor, dependant only on ω, the site spacing d, and mass; and another quantity dependant only on the range of chemical potentials $(\mu_{max} - \mu_{min})$. To speed up numerical calculations, the phase diagram can be converted into sums for one harmonic trap, also known as a state diagram [82]. All other sums can be obtained by simply changing the prefactor $\frac{\omega^3}{\sqrt{m}(\lambda/2)^3}$.

References

[1] J. E. Lye, L. Fallani, M. Modugno, D. S. Wiersma, C. Fort and M. Inguscio. Bose-Einstein condensate in a random potential. *Phys. Rev. Lett.* **95**, 070401 (2005).

[2] C. Fort, L. Fallani, V. Guarrera, J. E. Lye, M. Modugno, D. S. Wiersma and M. Inguscio. Effect of optical disorder and single defects on the expansion of a Bose-Einstein condensate in a one-dimensional waveguide. *Phys. Rev. Lett.* **95**, 170410 (2005).

[3] Y. P. Chen, J. Hitchcock, D. Dries, M. Junker, C. Welford and R. G. Hulet. Phase coherence and superfluid-insulator transition in a disordered Bose-Einstein condensate. *Phys. Rev. A* **77**, 033632 (2008).

[4] T. Schulte, S. Drenkelforth, J. Kruse, W. Ertmer, J. Arlt, K. Sacha, J. Zakrzewski and M. Lewenstein. Routes towards Anderson-like localization of Bose-Einstein condensates in disordered optical lattices. *Phys. Rev. Lett.* **95**, 170411 (2005).

[5] T. Schulte, S. Drenkelforth, G. K. Büning, W. Ertmer, J. Arlt, M. Lewenstein and L. Santos. Dynamics of Bloch oscillations in disordered lattice potentials. *Phys. Rev. A* **77**, 023610 (2008).

[6] S. Drenkelforth, G. K. Büning, J. Will, T. Schulte, N. Murray, W. Ertmer, L. Santos and J. J. Arlt. Damped Bloch oscillations of Bose-Einstein condensates in disordered potential gradients. *New J. Phys.* **10**, 045027 (2008).

[7] D. Clément, A. F. Varón, M. Hugbart, J. A. Retter, P. Bouyer, L. Sanchez-Palencia, D. M. Gangardt, G. V. Shlyapnikov and A. Aspect. Suppression of transport of an interacting elongated Bose-Einstein condensate in a random potential. *Phys. Rev. Lett.* **95**, 170409 (2005).

[8] L. Sanchez-Palencia, D. Clément, P. Lugan, P. Bouyer, G. V. Shlyapnikov and A. Aspect. Anderson localization of expanding Bose-Einstein condensates in random potentials. *Phys. Rev. Lett.* **98**, 210401 (2007).

[9] L. Fallani, J. E. Lye, V. Guarrera, C. Fort and M. Inguscio. Ultracold atoms in a disordered crystal of light: Towards a Bose glass. *Phys. Rev. Lett.* **98**, 130404 (2007).

[10] E. E. Edwards, M. Beeler, T. Hong and S. L. Rolston. Adiabaticity and localization in one-dimensional incommensurate lattices. *Phys. Rev. Lett.* **101**, 260402 (2008).

[11] B. Deissler, M. Zaccanti, G. Roati, C. DErrico, M. Fattori, M. Modugno, M. G. and M. Inguscio. Delocalization of a disordered bosonic system by repulsive interactions. *Nature Physics* **6**, 354–358 (2010).

[12] B. Deissler, E. Lucioni, M. Modugno, G. Roati, L. Tanzi, M. Zaccanti, M. Inguscio and G. Modugno. Correlation function of weakly interacting bosons in a disordered lattice. *New J. Phys.* **13**, 023020 (2011).

[13] J. Billy, V. Josse, Z. Zhanchun, B. Alain, B. Hambrecht, P. Lugan, D. Clement, L. Sanchez-Palancia, P. Bouyer and A. Aspect. Direct observation of Anderson localization of matter waves in a controlled disorder. *Nature* **453**, 891–894 (2008).

[14] G. Roati, C. D'Errico, L. Fallani, M. Fattori, C. Fort, M. Zaccanti, G. Modugno, M. Modugno and M. Inguscio. Anderson localization of a non-interacting Bose-Einstein condensate. *Nature* **453**, 895–898 (2008).

[15] B. Damski, J. Zakrzewski, L. Santos, P. Zoller and M. Lewenstein. Atomic Bose and Anderson glasses in optical lattices. *Phys. Rev. Lett.* **91**, 080403 (2003).

[16] P. Anderson. *The theory of superconductivity in the high-T_c cuprates* (Princeton University Press, 1997).

[17] E. Kim and M. Chan. Probable observation of a supersolid helium phase. *Nature* **427**, 225–227 (2004).

[18] J. Wu and P. Phillips. Minimal model for disorder-induced missing moment of inertia in solid ^{4}He. *Phys. Rev. B* **78**, 014515 (2008).

[19] A. van Oudenaarden, S. J. K. Várdy and J. E. Mooij. One-dimensional localization of quantum vortices in disordered Josephson junction arrays. *Phys. Rev. Lett.* **77**, 4257–4260 (1996).

[20] M. P. A. Fisher, P. B. Weichman, G. Grinstein and D. S. Fisher. Boson localization and the superfluid-insulator transition. *Phys. Rev. B* **40**, 546–570 (1989).

[21] W. Krauth, N. Trivedi and D. Ceperley. Superfluid-insulator transition in disordered boson systems. *Phys. Rev. Lett.* **67**, 2307–2310 (1991).

[22] S. Rapsch, U. Schollwöck and W. Zwerger. Density matrix renormalization group for disordered bosons in one dimension. *EPL (Europhysics Letters)* **46**, 559 (1999).

[23] V. Gurarie, L. Pollet, N. V. Prokof'ev, B. V. Svistunov and M. Troyer. Phase diagram of the disordered Bose-Hubbard model. *Phys. Rev. B* **80**, 214519 (2009).

[24] R. Feynman. Simulating physics with computers. *International Journal of Theoretical Physics* **21**, 467–488 (1982).

[25] D. M. Ceperley. Path integrals in the theory of condensed helium. *Rev. Mod. Phys.* **67**, 279–355 (1995).

[26] M. R. White. *Ultracold atoms in a disordered optical lattice*. Ph.D. thesis, University of Illinois at Urbana-Champaign (2009).

[27] H. J. Lewandowski, D. M. Harber, D. L. Whitaker and E. A. Cornell. Simplified system for creating a Bose-Einstein condensate. *Journal of Low Temperature Physics* **132**, 309–367 (2003).

[28] D. Steck. *Rubidium 87 D Line Data*. http://steck.us/alkalidata/ (2001).

[29] N. R. Newbury, C. J. Myatt and C. E. Wieman. s-wave elastic collisions between cold ground-state ^{87}Rb atoms. *Phys. Rev. A* **51**, R2680–R2683 (1995).

[30] W. Demtroeder. *Laser Spectroscopy* (Springer, Berlin, 2003), 3rd edn.

[31] P. F. Griffin. *Laser Cooling and Loading of Rb into a Large Period, Quasi-Electrostatic, Optical Lattice*. Ph.D. thesis, Durham University, Durham UK (2005).

[32] W. Petrich, M. H. Anderson, J. R. Ensher and E. A. Cornell. Behavior of atoms in a compressed magneto-optical trap. *J. Opt. Soc. Am. B* **11**, 1332–1335 (1994).

[33] W. Ketterle and N. van Druten. Evaporative cooling of atoms. In B. Bederson and H. Walther (eds.) *Advances in Atomic, Molecular, and Optical Physics*, vol. 37, 181 (1996).

[34] Y.-J. Lin, A. R. Perry, R. L. Compton, I. B. Spielman and J. V. Porto. Rapid production of ^{87}Rb Bose-Einstein condensates in a combined magnetic and optical potential. *Phys. Rev. A* **79**, 063631 (2009).

[35] C.-L. Hung, X. Zhang, N. Gemelke and C. Chin. Accelerating evaporative cooling of atoms into Bose-Einstein condensation in optical traps. *Phys. Rev. A* **78**, 011604 (2008).

[36] M. Greiner, O. Mandel, T. Esslinger, T. Hänsch and I. Bloch. Quantum phase transition from a superfluid to a Mott insulator in a gas of ultracold atoms. *Nature* **415**, 39–44 (2002).

[37] T. Stöferle, H. Moritz, C. Schori, M. Köhl and T. Esslinger. Transition from a strongly interacting 1d superfluid to a Mott insulator. *Phys. Rev. Lett.* **92**, 130403 (2004).

[38] M. Köhl, H. Moritz, T. Stöferle, C. Schori and T. Esslinger. Superfluid to Mott insulator transition in one, two, and three dimensions. *J. Low Temp. Phys.* **138**, 635–644 (2005).

[39] M. White, M. Pasienski, D. McKay, S. Q. Zhou, D. Ceperley and B. DeMarco. Strongly interacting bosons in a disordered optical lattice. *Phys. Rev. Lett.* **102**, 055301 (2009).

[40] R. Grimm, M. Weidemller and Y. B. Ovchinnikov. Optical dipole traps for neutral atoms. vol. 42 of *Advances In Atomic, Molecular, and Optical Physics*, 95 – 170 (Academic Press, 2000).

[41] J. Goodman. *Speckle Phenomena in Optics* (Roberts and Company, 2007).

[42] J. Goodman. *Introduction to Fourier Optics* (McGraw-Hill, 1998).

[43] S. Q. Zhou and D. M. Ceperley. Construction of localized wave functions for a disordered optical lattice and analysis of the resulting Hubbard model parameters. *Phys. Rev. A* **81**, 013402 (2010).

[44] M. Pasienski, D. McKay, M. White and B. DeMarco. A disordered insulator in an optical lattice. *Nature Physics* **6**, 677–680 (2010).

[45] W. S. Bakr, J. I. Gillen, A. Peng, S. Folling and M. Greiner. A quantum gas microscope for detecting single atoms in a Hubbard-regime optical lattice. *Nature* **462**, 74–77 (2009).

[46] D. McGloin, G. Spalding, H. Melville, W. Sibbett and K. Dholakia. Applications of spatial light modulators in atom optics. *Opt. Express* **11**, 158–166 (2003).

[47] S. Lal, S. Gopalakrishnan and P. M. Goldbart. Approaching multichannel Kondo physics using correlated bosons: Quantum phases and how to realize them. *Phys. Rev. B* **81**, 245314 (2010).

[48] B. T. Seaman, M. Krämer, D. Z. Anderson and M. J. Holland. Atomtronics: Ultracold-atom analogs of electronic devices. *Phys. Rev. A* **75**, 023615 (2007).

[49] M. Pasienski and B. DeMarco. A high-accuracy algorithm for designing arbitrary holographic atom traps. *Opt. Express* **16**, 2176–2190 (2008).

[50] G. D. Bruce, J. Mayoh, G. Smirne, L. Torralbo-Campo and D. Cassettari. A smooth, holographically generated ring trap for the investigation of superfluidity in ultracold atoms. *Physica Scripta* **2011**, 014008 (2011).

[51] M. Lewenstein, A. Sanpera, V. Ahufinger, B. Damski, A. Sen and U. Sen. Ultracold atomic gases in optical lattices: mimicking condensed matter physics and beyond. *Advances in Physics* **56**, 243–379 (2007). `arXiv:cond-mat/0606771`.

[52] T. Giamarchi and H. J. Schulz. Localization and interaction in one-dimensional quantum fluids. *EPL (Europhysics Letters)* **3**, 1287 (1987).

[53] T. Giamarchi and H. J. Schulz. Anderson localization and interactions in one-dimensional metals. *Phys. Rev. B* **37**, 325–340 (1988).

[54] F. London. The λ-phenomenon of liquid helium and the Bose-Einstein degeneracy. *Proceedings of the Royal Society, A* **153**, 576 (1938).

[55] P. Kapitska. Viscosity of liquid helium below the λ-point. *Nature* **141**, 74 (1938).

[56] J. Allen and M. A.D. Flow of liquid helium II. *Nature* **141**, 75 (1938).

[57] J. Allen and H. Jones. New phenomena connected with heat flow in helium II. *Nature* **141**, 243 (1938).

[58] B. C. Crooker, B. Hebral, E. N. Smith, Y. Takano and J. D. Reppy. Superfluidity in a dilute Bose gas. *Phys. Rev. Lett.* **51**, 666–669 (1983).

[59] M. H. W. Chan, K. I. Blum, S. Q. Murphy, G. K. S. Wong and J. D. Reppy. Disorder and the superfluid transition in liquid ^{4}He. *Phys. Rev. Lett.* **61**, 1950–1953 (1988).

[60] J. D. Reppy. Superfluid helium in porous media. *Journal of Low Temperature Physics* **87**, 205–245 (1992).

[61] P. A. Crowell, F. W. Van Keuls and J. D. Reppy. Superfluid-insulator transition in ^{4}He films adsorbed in Vycor glass. *Phys. Rev. Lett.* **75**, 1106–1109 (1995).

[62] P. A. Crowell, F. W. Van Keuls and J. D. Reppy. Onset of superfluidity in ^{4}He films adsorbed on disordered substrates. *Phys. Rev. B* **55**, 12620–12634 (1997).

[63] A. S. C. Rittner and J. D. Reppy. Disorder and the supersolid state of solid ^{4}He. *Phys. Rev. Lett.* **98**, 175302 (2007).

[64] D. M. Ceperley and B. Bernu. Ring exchanges and the supersolid phase of ^{4}He. *Phys. Rev. Lett.* **93**, 155303 (2004).

[65] L. Pollet, N. V. Prokof'ev, B. V. Svistunov and M. Troyer. Absence of a direct superfluid to Mott insulator transition in disordered Bose systems. *Phys. Rev. Lett.* **103**, 140402 (2009).

[66] D. Jaksch, C. Bruder, J. I. Cirac, C. W. Gardiner and P. Zoller. Cold bosonic atoms in optical lattices. *Phys. Rev. Lett.* **81**, 3108–3111 (1998).

[67] S. Inouye, M. R. Andrews, J. Stenger, H.-J. Miesner, D. M. Stamper-Kurn and W. Ketterle. Observation of Feshbach resonances in a Bose-Einstein condensate. *Nature* **392**, 151–154 (1998).

[68] C. Chin, R. Grimm, P. Julienne and E. Tiesinga. Feshbach resonances in ultracold gases. *Rev. Mod. Phys.* **82**, 1225–1286 (2010).

[69] B. DeMarco, C. Lannert, S. Vishveshwara and T.-C. Wei. Structure and stability of Mott-insulator shells of bosons trapped in an optical lattice. *Phys. Rev. A* **71**, 063601 (2005).

[70] K. V. Krutitsky, A. Pelster and R. Graham. Mean-field phase diagram of disordered bosons in a lattice at nonzero temperature. *New J. Phys.* **8**, 187 (2006).

[71] D. McKay, M. White, M. Pasienski and B. DeMarco. Phase-slip-induced dissipation in an atomic Bose-Hubbard system. *Nature* **453**, 895–898 (2008).

[72] K. Huang. *Introduction to Statistical Physics* (CRC Press, 2001).

[73] N. Gemelke, X. Zhang, C. Hung and C. Chin. In situ observation of incompressible Mott-insulating domains in ultracold atomic gases. *Nature* **460**, 995–998 (2009).

[74] G. G. Batrouni, V. Rousseau, R. T. Scalettar, M. Rigol, A. Muramatsu, P. J. H. Denteneer and M. Troyer. Mott domains of bosons confined on optical lattices. *Phys. Rev. Lett.* **89**, 117203 (2002).

[75] K. Sheshadri, H. R. Krishnamurthy, R. Pandit and T. V. Ramakrishnan. Superfluid and insulating phases in an interacting-boson model: Mean-field theory and the RPA. *EPL (Europhysics Letters)* **22**, 257 (1993).

[76] D. S. Rokhsar and B. G. Kotliar. Gutzwiller projection for bosons. *Phys. Rev. B* **44**, 10328–10332 (1991).

[77] M. C. Gutzwiller. Correlation of electrons in a narrow s band. *Phys. Rev.* **137**, A1726–A1735 (1965).

[78] W. Krauth, M. Caffarel and J.-P. Bouchaud. Gutzwiller wave function for a model of strongly interacting bosons. *Phys. Rev. B* **45**, 3137–3140 (1992).

[79] X. Lu and Y. Yu. Finite-temperature effects on the number fluctuation of ultracold atoms across the superfluid–to–Mott-insulator transition. *Phys. Rev. A* **74**, 063615 (2006).

[80] C. Kollath, A. M. Läuchli and E. Altman. Quench dynamics and nonequilibrium phase diagram of the Bose-Hubbard model. *Phys. Rev. Lett.* **98**, 180601 (2007).

[81] U. R. Fischer, R. Schützhold and M. Uhlmann. Bogoliubov theory of quantum correlations in the time-dependent Bose-Hubbard model. *Phys. Rev. A* **77**, 043615 (2008).

[82] M. Rigol, G. G. Batrouni, V. G. Rousseau and R. T. Scalettar. State diagrams for harmonically trapped bosons in optical lattices. *Phys. Rev. A* **79**, 053605 (2009).

[83] K. Jiménez-García, R. L. Compton, Y.-J. Lin, W. D. Phillips, J. V. Porto and I. B. Spielman. Phases of a two-dimensional Bose gas in an optical lattice. *Phys. Rev. Lett.* **105**, 110401 (2010).

[84] M. Greiner. *Ultracold quantum gases in three-dimensional optical lattice potentials.* Ph.D. thesis, University of Munich, Munich (2003).

[85] T.-L. Ho and Q. Zhou. Intrinsic heating and cooling in adiabatic processes for bosons in optical lattices. *Phys. Rev. Lett.* **99**, 120404 (2007).

[86] P. B. Blakie and J. V. Porto. Adiabatic loading of bosons into optical lattices. *Phys. Rev. A* **69**, 013603 (2004).

[87] A. M. Rey, G. Pupillo and J. V. Porto. The role of interactions, tunneling, and harmonic confinement on the adiabatic loading of bosons in an optical lattice. *Phys. Rev. A* **73**, 023608 (2006).

[88] J. A. Hertz, L. Fleishman and P. W. Anderson. Marginal fluctuations in a Bose glass. *Phys. Rev. Lett.* **43**, 942–946 (1979).

[89] G. A. Csáthy, J. D. Reppy and M. H. W. Chan. Substrate-tuned boson localization in superfluid ^{4}He films. *Phys. Rev. Lett.* **91**, 235301 (2003).

[90] R. M. Bradley and S. Doniach. Quantum fluctuations in chains of Josephson junctions. *Phys. Rev. B* **30**, 1138–1147 (1984).

[91] W. Zwerger. Global and local phase coherence in dissipative Josephson-junction arrays. *EPL (Europhysics Letters)* **9**, 421 (1989).

[92] H. S. J. van der Zant, W. J. Elion, L. J. Geerligs and J. E. Mooij. Quantum phase transitions in two dimensions: Experiments in Josephson-junction arrays. *Phys. Rev. B* **54**, 10081–10093 (1996).

[93] I. S. Beloborodov, A. V. Lopatin, V. M. Vinokur and K. B. Efetov. Granular electronic systems. *Rev. Mod. Phys.* **79**, 469–518 (2007).

[94] D. K. K. Lee and J. M. F. Gunn. Dirty bosons: Screening, inert layers and the Lifshitz tail. *Journal of Low Temperature Physics* **89**, 101–113 (1992).

[95] A. De Martino, M. Thorwart, R. Egger and R. Graham. Exact results for one-dimensional disordered bosons with strong repulsion. *Phys. Rev. Lett.* **94**, 060402 (2005).

[96] K. G. Singh and D. S. Rokhsar. Disordered bosons: Condensate and excitations. *Phys. Rev. B* **49**, 9013–9023 (1994).

[97] K. Sheshadri, H. R. Krishnamurthy, R. Pandit and T. V. Ramakrishnan. Percolation-enhanced localization in the disordered bosonic Hubbard model. *Phys. Rev. Lett.* **75**, 4075–4078 (1995).

[98] P. Buonsante, V. Penna, A. Vezzani and P. B. Blakie. Mean-field phase diagram of cold lattice bosons in disordered potentials. *Phys. Rev. A* **76**, 011602 (2007).

[99] U. Bissbort and W. Hofstetter. Stochastic mean-field theory for the disordered Bose-Hubbard model. *EPL (Europhysics Letters)* **86**, 50007 (2009).

[100] M. Wallin, E. S. So/rensen, S. M. Girvin and A. P. Young. Superconductor-insulator transition in two-dimensional dirty boson systems. *Phys. Rev. B* **49**, 12115–12139 (1994).

[101] M. B. Hastings. Bose glass in a large-n commensurate dirty boson model. *Phys. Rev. B* **64**, 024517 (2001).

[102] B. V. Svistunov. Superfluid-Bose-glass transition in weakly disordered commensurate one-dimensional system. *Phys. Rev. B* **54**, 16131–16134 (1996).

[103] F. Pázmándi and G. T. Zimányi. Direct Mott insulator-to-superfluid transition in the presence of disorder. *Phys. Rev. B* **57**, 5044–5047 (1998).

[104] P. B. Weichman and R. Mukhopadhyay. Particle-hole symmetry and the dirty boson problem. *Phys. Rev. B* **77**, 214516 (2008).

[105] T. D. Kühner and H. Monien. Phases of the one-dimensional Bose-Hubbard model. *Phys. Rev. B* **58**, R14741–R14744 (1998).

[106] L. Zhang and M. Ma. Real-space renormalization-group study of hard-core dirty bosons. *Phys. Rev. B* **45**, 4855–4863 (1992).

[107] I. F. Herbut. Dual superfluid-Bose-glass critical point in two dimensions and the universal conductivity. *Phys. Rev. Lett.* **79**, 3502–3505 (1997).

[108] R. T. Scalettar, G. G. Batrouni and G. T. Zimanyi. Localization in interacting, disordered, Bose systems. *Phys. Rev. Lett.* **66**, 3144–3147 (1991).

[109] W. Krauth and N. Trivedi. Mott and superfluid transitions in a strongly interacting lattice boson system. *EPL (Europhysics Letters)* **14**, 627 (1991).

[110] G. G. Batrouni and R. T. Scalettar. World-line quantum Monte Carlo algorithm for a one-dimensional Bose model. *Phys. Rev. B* **46**, 9051–9062 (1992).

[111] J. Kisker and H. Rieger. Bose-glass and Mott-insulator phase in the disordered boson Hubbard model. *Phys. Rev. B* **55**, R11981–R11984 (1997).

[112] P. Hitchcock and E. S. Sørensen. Bose-glass to superfluid transition in the three-dimensional Bose-Hubbard model. *Phys. Rev. B* **73**, 174523 (2006).

[113] M. Makivić, N. Trivedi and S. Ullah. Disordered bosons: Critical phenomena and evidence for new low energy excitations. *Phys. Rev. Lett.* **71**, 2307–2310 (1993).

[114] P. Sen, N. Trivedi and D. M. Ceperley. Simulation of flux lines with columnar pins: Bose glass and entangled liquids. *Phys. Rev. Lett.* **86**, 4092–4095 (2001).

[115] J.-W. Lee, M.-C. Cha and D. Kim. Phase diagram of a disordered boson hubbard model in two dimensions. *Phys. Rev. Lett.* **87**, 247006 (2001).

[116] N. Prokof'ev and B. Svistunov. Superfluid-insulator transition in commensurate disordered bosonic systems: Large-scale worm algorithm simulations. *Phys. Rev. Lett.* **92**, 015703 (2004).

[117] P. Niyaz, R. T. Scalettar, C. Y. Fong and G. G. Batrouni. Ground-state phase diagram of an interacting Bose model with near-neighbor repulsion. *Phys. Rev. B* **44**, 7143–7146 (1991).

[118] J. K. Freericks and H. Monien. Phase diagram of the Bose-Hubbard model. *EPL (Europhysics Letters)* **26**, 545 (1994).

[119] J. K. Freericks and H. Monien. Strong-coupling expansions for the pure and disordered Bose-Hubbard model. *Phys. Rev. B* **53**, 2691–2700 (1996).

[120] K. J. Runge. Numerical study of the onset of superfluidity in two-dimensional, disordered, hard-core bosons. *Phys. Rev. B* **45**, 13136–13139 (1992).

[121] G. Roux, T. Barthel, I. P. McCulloch, C. Kollath, U. Schollwöck and T. Giamarchi. Quasiperiodic Bose-Hubbard model and localization in one-dimensional cold atomic gases. *Phys. Rev. A* **78**, 023628 (2008).

[122] B. Kramer and A. MacKinnon. Localization: theory and experiment. *Reports on Progress in Physics* **56**, 1469 (1993).

[123] G. Modugno. Anderson localization in Bose-Einstein condensates. *Reports on Progress in Physics* **73**, 102401 (2010).

[124] E. Abrahams, P. W. Anderson, D. C. Licciardello and T. V. Ramakrishnan. Scaling theory of localization: Absence of quantum diffusion in two dimensions. *Phys. Rev. Lett.* **42**, 673–676 (1979).

[125] P. Lugan, D. Clément, P. Bouyer, A. Aspect, M. Lewenstein and L. Sanchez-Palencia. Ultracold Bose gases in 1d disorder: From Lifshits glass to Bose-Einstein condensate. *Phys. Rev. Lett.* **98**, 170403 (2007).

[126] Q. Zhou and S. Das Sarma. Bosons in a double-well potential: Understanding the interplay between disorder and interaction in a simple model. *Phys. Rev. A* **82**, 041601 (2010).

[127] D. Stauffer and A. Aharony. *Introduction to Percolation Theory* (Taylor and Francis, London:, 1992), 2nd ed. edn.

[128] T. Schwartz, G. Bartal, S. Fishman and M. Segev. Transport and Anderson localization in disordered two-dimensional photonic lattices. *Nature* **446**, 52–55.

[129] P. A. Lee and T. V. Ramakrishnan. Disordered electronic systems. *Rev. Mod. Phys.* **57**, 287–337 (1985).

[130] D. K. K. Lee and J. M. F. Gunn. Bosons in a random potential: condensation and screening in a dense limit. *Journal of Physics: Condensed Matter* **2**, 7753 (1990).

[131] O. F. Syljuåsen. Directed loop updates for quantum lattice models. *Phys. Rev. E* **67**, 046701 (2003).

[132] N. Prokofev, B. Svistunov and I. Tupitsyn. Exact, complete, and universal continuous-time worldline Monte Carlo approach to the statistics of discrete quantum systems. *J. Exp. Theor. Phys.* **87**, 310–321 (1998).

[133] R. E. Packard and J. C. Davis. Phase slip phenomena in superfluid helium. *Physica B* **197**, 315 – 323 (1994).

[134] A. Amar, J. Davis, R. Packard and R. Lozes. Phase-slips in the flow of superfluid 4he through a submicron orifice. *Physica B* **165-166**, 753 – 754 (1990). Proceedings of the 19th International Conference on Low Temperature Physics.

[135] A. Bezryadin, C. N. Lau and M. Tinkham. Quantum suppression of superconductivity in ultrathin nanowires. *Nature* **404**, 971–974 (2000).

[136] M. Tinkham. *Introduction to Superconductivity* (Dover Publications, 1996).

[137] M. Greiner, I. Bloch, O. Mandel, T. W. Hänsch and T. Esslinger. Exploring phase coherence in a 2d lattice of Bose-Einstein condensates. *Phys. Rev. Lett.* **87**, 160405 (2001).

[138] J. H. Denschlag, J. E. Simsarian, H. Hffner, C. McKenzie, A. Browaeys, D. Cho, K. Helmerson, S. L. Rolston and W. D. Phillips. A Bose-Einstein condensate in an optical lattice. *J. Phys. B: At., Mol. Opt. Phys.* **35**, 3095 (2002).

[139] D. McKay, M. White and B. DeMarco. Lattice thermodynamics for ultracold atoms. *Phys. Rev. A* **79**, 063605 (2009).

[140] W. Yi, G.-D. Lin and L.-M. Duan. Signal of Bose-Einstein condensation in an optical lattice at finite temperature. *Phys. Rev. A* **76**, 031602 (2007).

[141] G.-D. Lin, W. Zhang and L.-M. Duan. Characteristics of Bose-Einstein condensation in an optical lattice. *Phys. Rev. A* **77**, 043626 (2008).

[142] Y. Castin and R. Dum. Bose-Einstein condensates in time dependent traps. *Phys. Rev. Lett.* **77**, 5315–5319 (1996).

[143] C. Pethick and H. Smith. *Bose-Einstein Condensation in Dilute Gases* (Cambridge University Press, 2001).

[144] J. Catani, G. Barontini, G. Lamporesi, F. Rabatti, G. Thalhammer, F. Minardi, S. Stringari and M. Inguscio. Entropy exchange in a mixture of ultracold atoms. *Phys. Rev. Lett.* **103**, 140401 (2009).

[145] D. Chen, M. White, C. Borries and B. DeMarco. Quantum quench of an atomic mott insulator (2011). http://arxiv.org/abs/1103.4662.

[146] E. Altman, Y. Kafri, A. Polkovnikov and G. Refael. Phase transition in a system of one-dimensional bosons with strong disorder. *Phys. Rev. Lett.* **93**, 150402 (2004).

[147] P. Sengupta and S. Haas. Quantum glass phases in the disordered Bose-Hubbard model. *Phys. Rev. Lett.* **99**, 050403 (2007).

[148] B. Bulka, M. Schreiber and B. Kramer. Localization, quantum interference, and the metal-insulator transition. *Z. Phys. B* **66**, 21–30 (1987).

[149] K. O'Holleran, M. R. Dennis, F. Flossmann and M. J. Padgett. Fractality of light's darkness. *Phys. Rev. Lett.* **100**, 053902 (2008).

[150] D. G. Grier. A revolution in optical manipulation. *Nature* **424**, 810–816 (2003).

[151] S. N. Dixit, J. K. Lawson, K. R. Manes, H. T. Powell and K. A. Nugent. Kinoform phase plates for focal plane irradiance profile control. *Opt. Lett.* **19**, 417–419 (1994).

[152] S. N. Dixit, M. D. Feit, M. D. Perry and H. T. Powell. Designing fully continuous phase screens for tailoring focal-plane irradiance profiles. *Opt. Lett.* **21**, 1715–1717 (1996).

[153] Y. Lin, T. J. Kessler and G. N. Lawrence. Distributed phase plates for super-Gaussian focal-plane irradiance profiles. *Opt. Lett.* **20**, 764–766 (1995).

[154] J. S. Liu and M. R. Taghizadeh. Iterative algorithm for the design of diffractive phase elements for laser beam shaping. *Opt. Lett.* **27**, 1463–1465 (2002).

[155] R. Ozeri, L. Khaykovich and N. Davidson. Long spin relaxation times in a single-beam blue-detuned optical trap. *Phys. Rev. A* **59**, R1750–R1753 (1999).

[156] S. Bergamini, B. Darquié, M. Jones, L. Jacubowiez, A. Browaeys and P. Grangier. Holographic generation of microtrap arrays for single atoms by use of a programmable phase modulator. *J. Opt. Soc. Am. B* **21**, 1889–1894 (2004).

[157] J. Sebby-Strabley, R. T. R. Newell, J. O. Day, E. Brekke and T. G. Walker. High-density mesoscopic atom clouds in a holographic atom trap. *Phys. Rev. A* **71**, 021401 (2005).

[158] V. Boyer, R. M. Godun, G. Smirne, D. Cassettari, C. M. Chandrashekar, A. B. Deb, Z. J. Laczik and C. J. Foot. Dynamic manipulation of Bose-Einstein condensates with a spatial light modulator. *Phys. Rev. A* **73**, 031402 (2006).

[159] V. Kotlyar, P. Seraphimovich and V. Soifer. An iterative algorithm for designing diffractive optical elements with regularization. *Opt. Laser Eng.* **29**, 261–268 (1998).

[160] P. Senthilkumaran and F. Wyrowski. Phase synthesis in wave-optical engineering: mapping- and diffuser-type approaches. *J. Mod. Opt.* **49**, 1831–1850 (2002).

[161] V. Arrizón, M. Testorf, S. Sinzinger and J. Jahns. Iterative optimization of phase-only diffractive optical elements based on a lenslet array. *J. Opt. Soc. Am. A* **17**, 2157–2164 (2000).

[162] M. Gruber. Diffractive optical elements as raster-image generators. *Appl. Opt.* **40**, 5830–5839 (2001).

[163] A. E. Leanhardt, A. P. Chikkatur, D. Kielpinski, Y. Shin, T. L. Gustavson, W. Ketterle and D. E. Pritchard. Propagation of Bose-Einstein condensates in a magnetic waveguide. *Phys. Rev. Lett.* **89**, 040401 (2002).

[164] J. Fortágh, H. Ott, S. Kraft, A. Günther and C. Zimmermann. Surface effects in magnetic microtraps. *Phys. Rev. A* **66**, 041604 (2002).

[165] A. E. Leanhardt, Y. Shin, A. P. Chikkatur, D. Kielpinski, W. Ketterle and D. E. Pritchard. Bose-Einstein condensates near a microfabricated surface. *Phys. Rev. Lett.* **90**, 100404 (2003).

[166] J. Estève, C. Aussibal, T. Schumm, C. Figl, D. Mailly, I. Bouchoule, C. I. Westbrook and A. Aspect. Role of wire imperfections in micromagnetic traps for atoms. *Phys. Rev. A* **70**, 043629 (2004).

[167] M. A. Seldowitz, J. P. Allebach and D. W. Sweeney. Synthesis of digital holograms by direct binary search. *Appl. Opt.* **26**, 2788–2798 (1987).

[168] L. Legeard, P. Réfrégier and P. Ambs. Multicriteria optimality for iterative encoding of computer-generated holograms. *Appl. Opt.* **36**, 7444–7449 (1997).

[169] J. Fienup. Iterative method applied to image reconstruction and to computer-generated holograms. *Opt. Eng.* **19**, 297–305 (1980).

[170] F. Wyrowski. Diffraction efficiency of analog and quantized digital amplitude holograms: analysis and manipulation. *J. Opt. Soc. Am. A* **7**, 383–393 (1990).

[171] V. Soifer. *Methods for Computer Design of Diffractive Optical Elements* (John Wiley and Sons, NY, 2002).

[172] O. Ripoll, V. Kettunen and H. Herzig. Review of iterative Fourier-transform algorithms for beam shaping applications". *Opt. Eng.* **43** (2004).

[173] G. Spalding, J. Courtial and R. DiLeonardo. *Holographic Optical Trapping in Structured Light and its Applications: An Introduction to Phase-Structured Beams and Nanoscale Optical Forces* (Elsevier Press, 2008).

[174] R. Piestun and J. Shamir. Synthesis of three-dimensional light fields and applications. *Proc. IEEE* **90**, 222–244 (2002).

[175] F. Wyrowski and O. Bryngdahl. Iterative Fourier-transform algorithm applied to computer holography. *J. Opt. Soc. Am. A* **5**, 1058–1065 (1988).

[176] L. Bigué and P. Ambs. Optimal multicriteria approach to the iterative Fourier transform algorithm. *Appl. Opt.* **40**, 5886–5893 (2001).

[177] S. Bühling and F. Wyrowski. Improved transmission design algorithms by utilizing variable-strength projections. *J. Mod. Opt.* **49**, 1871–1892 (2002).

[178] H. Akahori. Spectrum leveling by an iterative algorithm with a dummy area for synthesizing the kinoform. *Appl. Opt.* **25**, 802–811 (1986).

[179] H. Aagedal, M. Schmid, T. Beth, S. Tiewes and F. Wyrowski. Theory of speckles in diffractive optics and its application to beam shaping. *J. Mod.Opt.* **43**, 1409–1421 (1996).

[180] P. Senthilkumaran, F. Wyrowski and H. Schimmel. Vortex stagnation problem in iterative Fourier-transform algorithms. *Opt. Lasers Eng.* **43**, 43–56 (2005).

[181] E. A. Sziklas and A. E. Siegman. Mode calculations in unstable resonators with flowing saturable gain. 2: Fast Fourier transform method. *Appl. Opt.* **14**, 1874–1889 (1975).

[182] K.-H. Brenner. Method for designing arbitrary two-dimensional continuous phase elements. *Opt. Lett.* **25**, 31–33 (2000).

[183] D. R. Scherer, C. N. Weiler, T. W. Neely and B. P. Anderson. Vortex formation by merging of multiple trapped Bose-Einstein condensates. *Phys. Rev. Lett.* **98**, 110402 (2007).

[184] N. Bertaux, Y. Frauel, P. Réfrégier and B. Javidi. Speckle removal using a maximum-likelihood technique with isoline gray-level regularization. *J. Opt. Soc. Am. A* **21**, 2283–2291 (2004).

[185] T. Willmore. *Riemannian Geometry* (Oxford University Press, 1997).

[186] O. Bryngdahl. Optical map transformations. *Optics Communications* **10**, 164 – 168 (1974).

[187] O. Bryngdahl. Geometrical transformations in optics. *J. Opt. Soc. Am.* **64**, 1092–1099 (1974).

[188] T. Dresel, M. Beyerlein and J. Schwider. Design of computer-generated beam-shaping holograms by iterative finite-element mesh adaption. *Appl. Opt.* **35**, 6865–6874 (1996).

[189] C. Kohler, X. Schwab and W. Osten. Optimally tuned spatial light modulators for digital holography. *Appl. Opt.* **45**, 960–967 (2006).

[190] T. Inoue, N. Matsumoto, N. Fukuchia, Y. Kobayashi and T. Hara. Highly stable wavefront control using a hybrid liquid-crystal spatial light modulator. *Proc. SPIE* **6306**, 630603 (2006).

[191] J. M. Kim, B. S. Choi, S. I. Kim, J. M. Kim, H. I. Bjelkhagen and N. J. Phillips. Holographic optical elements recorded in silver halide sensitized gelatin emulsions. part i. transmission holographic optical elements. *Appl. Opt.* **40**, 622–632 (2001).

[192] T. Dresel, M. Beyerlein and J. Schwider. Design and fabrication of computer-generated beam-shaping holograms. *Appl. Opt.* **35**, 4615–4621 (1996).